Development of Refrigeration and Air-Conditioning Technologies for Practical Use of Next-Generation Low-GWP Refrigerants

Volume 3

Group for Equipment Component Technologies

Development of Elemental Technologies Compatible with Refrigerant Mixtures

FY2023-2025 Progress Report

September 2026

New Energy and Industrial Technology Development Organization (NEDO)

Contents

1. Research and Development Overview and Outcomes 1
1.1 Background and Objectives 1
1.2 Heat Exchangers 2
1.2.1 Research and development of heat exchanger elemental technologies for suppressing heat transfer deterioration in low-GWP refrigerant mixtures 2
1.2.2 Fundamental research on suppressing heat transfer deterioration in low-GWP refrigerant mixtures and development of heat exchanger application technologies 2
1.2.3 Research and development on improving the evaporation and condensation performance of refrigerant mixtures by controlling the surface structure of aluminum and applying the technology to heat transfer tubes 3
1.2.4 Research and development on elucidating the thermal-fluid mechanisms of low-GWP refrigerant mixtures and heat transfer enhancement technologies 4
1.3 Compressors 4
1.3.1 Elucidation of refrigerant dissolution behavior in refrigerating oils in compressors, compatibility evaluation, and compression characteristics of low-GWP refrigerant mixtures 4
1.3.2 Elucidation of friction, wear, and lubrication characteristics in low-GWP refrigerant mixture atmospheres for improving compressor mechanical efficiency 5
1.3.3 Development of metal matrix composite materials suitable for compressor components and evaluation of their fundamental properties 6
1.4 Summary 6
2. Research and Development of Heat Exchanger Elemental Technologies for Suppressing Heat Transfer Deterioration in Low-GWP Refrigerant Mixtures (Saga University) 9
2.1 Design and Performance Evaluation of Refrigerant–Air Heat Exchangers 9
2.1.1 Characteristics of heat exchange in refrigeration cycles using refrigerant mixtures 9
2.1.2 Outline of apparatus and test heat exchanger 10
2.1.3 Experimental conditions 12
2.1.4 Experimental results and discussion 13
2.2 Transport Properties of Refrigerants 16
2.2.1 Overview and status of measurements 16
2.2.2 Measurement method for viscosity and example measurements 17
2.2.3 Measurement method for thermal conductivity and example measurements 18
2.2.4 Calculation model for transport properties: ECS model 20
2.3 Heat Transfer Database 21
2.3.1 Collection and structure of heat transfer data 21
2.3.2 Correlation evaluation function 21
2.4 Prediction of Heat Transfer Coefficients Using Machine Learning 22
2.4.1 Machine learning and workflow 22
2.4.2 Prediction models used for machine learning 22
2.4.3 Heat transfer data 23
2.4.4 Evaluation of machine learning 24

3. Basic Research on Suppression of Heat Transfer Degradation in Low-GWP Refrigerant Mixtures and Development of Heat Exchanger Application Technologies (Tokyo University of Marine Science and Technology) 29

3.1 Introduction 29
3.2 Experimental Apparatus and Data Reduction Method 29
3.2.1 Experimental apparatus 29
3.2.2 Data reduction method 30
3.3 Condensation and Evaporation Heat Transfer Characteristics of Low-GWP Refrigerant Mixtures 30
3.3.1 Evaluation of condensation heat transfer characteristics of the refrigerant mixture R474A 30
3.3.2 Evaluation of evaporation heat transfer characteristics of the refrigerant mixture R474A 31
3.4 Evaluation of Heat Transfer Enhancement by Surface Characteristics and Flow-Channel Geometry 32
3.4.1 Heat transfer enhancement by surface characteristics 32
3.4.2 Heat transfer enhancement by flow-channel geometry 33
3.5 Conclusions 35

4. Research and Development on Improving the Evaporation and Condensation Performance of Refrigerant Mixtures by Controlling the Surface Structure of Aluminum and Applying the Technology to Heat Transfer Tubes (UACJ) 36

4.1 Application of Refrigerant Mixtures to Heat Exchangers 36
4.1.1 Aluminum multiport tubes used in heat exchangers 36
4.1.2 Issues and countermeasures for heat transfer tubes in the application of refrigerant mixtures 36
4.1.3 Improvement of refrigerant boiling characteristics by surface treatment of aluminum 36
4.1.4 Objectives of this project 38
4.2 Approaches for Improving Heat Transfer Characteristics 39
4.2.1 Improvement of heat transfer performance by forming porous structures on aluminum surfaces 39
4.2.2 Verification toward anodizing treatment of the inner walls of multiport tubes 40
4.3 Future Issues 44

5. Elucidation of Thermal-Fluid Mechanisms of Low-GWP Refrigerant Mixtures and Research and Development of Heat Transfer Enhancement Technologies (Kobe University) 45

5.1 Void Fraction and Pressure Loss Characteristics of Zeotropic Refrigerant Mixture Two-Phase Flow in a Horizontal Mini-channel 45
5.1.1 Background and Objectives 45
5.1.2 Experimental Apparatus and Methods 46
5.1.3 Experimental Results and Discussion 48
5.2 Heat Transfer and Flow Characteristics of Refrigerant Evaporating Flow in Parallel Mini-Channels 51
5.2.1 Background and Objectives 51
5.2.2 Experimental Apparatus and Methods 51
5.2.3 Experimental Results and Discussion 53
5.3 Development of Evaluation and Improvement Methods for Nucleate Boiling Heat Transfer and Boiling Incipience Superheat in Non-Azeotropic Refrigerant Mixtures 55
5.3.1 Background and Objectives 55
5.3.2 Experimental Apparatus and Experimental Methods 56
5.3.3 Experimental Results and Discussion 57
5.4 Summary 61

6. Elucidation of Refrigerant Dissolution Behavior and Compatibility Evaluation of Refrigeration Oil in Compressors and Compression Characteristics of Low-GWP Mixed Refrigerants (Shizuoka University) 65

6.1 Overview of Research and Development 65
6.2 Solubility Characteristics of Refrigeration Oil/Refrigerant Mixtures: Solubility, Physical-Property Measurement, and Volume Change 66
6.2.1 Background and objectives 66
6.2.2 Experimental apparatus and method 66
6.2.3 Solubility and refractive index of refrigeration oil/refrigerant mixtures 67
6.2.4 Volume change associated with refrigerant dissolution in refrigeration oil 70
6.3 Solubility Characteristics of Refrigeration Oil/Refrigerant Mixtures: Dissolved Components and Solubility Prediction 72
6.3.1 Background and objectives 72
6.3.2 Experimental apparatus and method 72
6.3.3 Dissolved composition of refrigeration oil/refrigerant mixtures under saturated dissolution conditions 73
6.4 Formulation of Oil-Return Amount Based on Oil-Film Measurements in a Vertical Upward Pipe 74
6.4.1 Background and objectives 74
6.4.2 Film-thickness measurement using a fiber-optic liquid-film sensor and prediction of the base liquid film 74
6.4.3 Transport mechanism of highly viscous liquids in annular flow 76
6.5 Construction of a Compressor-Characteristics Prediction Model Considering Composition Changes in Mixed Refrigerants and Evaluation of Applicability of Alternative Refrigerants 78
6.5.1 Background and objectives 78
6.5.2 Construction of the compressor-characteristics prediction model 78
6.5.3 Validation of the prediction accuracy of the compressor model 80
6.5.4 Prediction of compressor characteristics associated with composition changes in R32/R1234yf mixed refrigerant 80
6.6 Development of Design Guidelines for High-Speed Compressors Using Low-GWP Refrigerants and Testing of Prototype Compressors 81
6.6.1 Background and objectives 81
6.6.2 Issues associated with increasing compressor speed and examination of countermeasures 82
6.6.3 Theoretical examination 83
6.6.4 Prototype compressor fabrication and integration into the test refrigeration cycle 84

7. Elucidation of Friction, Wear, and Lubrication Characteristics in Low-GWP Mixed-Refrigerant Atmospheres for Improving the Mechanical Efficiency of Compressors (Osaka Electro-Communication University) 86

7.1 Overview of Research and Development and Outcomes 86
7.2 Friction Characteristics of Rolling-Piston Rotary Compressors 86
7.2.1 Friction characteristics of rotary compressors 86
7.2.2 Friction characteristics between the vane and fixed groove 87
7.2.3 Friction characteristics between the vane and rolling piston 89
7.2.4 Wear characteristics of cast iron and composite materials 92
7.3 Examination of Compressor Mechanical Efficiency Based on Experimental Results for the Coefficient of Friction 92

8. Development of Metal-Matrix Composite Materials Suitable for Compressor Components and

Evaluation of Their Fundamental Properties (Advance Composite Co., Ltd.) 94
8.1 Design of Metal-Matrix Composite Materials 94
8.1.1 Material survey for compressor components (FY2023) 94
8.1.2 Design of metal-matrix composite materials 94
8.2 Development of Metal-Matrix Composite Materials 95
8.2.1 Verification of the effects of changing the matrix in metal-matrix composite materials (FY2023) 95
8.2.2 Design and development of reinforcement structure in metal-matrix composite materials (FY2024) 96
8.2.3 Machinability evaluation of metal-matrix composite materials (FY2025) 98
8.2.4 Summary 105
8.2.5 Future plans 105

1. Research and Development Overview and Outcomes

1.1 Background and Objectives

To suppress global warming caused by refrigerants used in refrigeration and air-conditioning equipment, the Kigali Amendment to the Montreal Protocol quantitatively defines reduction targets for HFC refrigerants with high global warming potential (GWP). In Japan, institutional measures to meet these targets are being implemented via the designated product system under the Act on Rational Use and Proper Management of Fluorocarbons, the quota system, and the promotion of refrigerant recovery and reclamation. To achieve this effectively, it is essential to develop not only new low-GWP refrigerants as alternatives to HFC refrigerants but also technologies for using them efficiently. Several HFO refrigerants have been developed as candidate low-GWP refrigerants; however, further HFO refrigerant candidates are considered unlikely to emerge. Nevertheless, no single HFO refrigerant has yet been developed that can be appropriately used in residential air conditioners and similar equipment. Moreover, many refrigerant mixtures have been proposed, whether combining multiple HFO refrigerants or blending HFO and HFC refrigerants.

In these refrigerant mixtures, the temperature changes continuously during condensation and evaporation because the boiling points of the individual components differ. This phenomenon, also referred to as temperature glide, contributes to deterioration in heat exchanger performance. In addition, during condensation and evaporation, heat transfer performance decreases owing to mass transfer resistance caused by concentration changes at the gas–liquid interface. Accordingly, this heat transfer deterioration mechanism must be quantitatively elucidated and technologies for suppressing it developed. Furthermore, heat exchangers with flow-channel structures adapted to temperature during phase change must be developed.

Although the basic mechanism of vapor compression in compressors itself does not differ substantially from conventional systems, the use of new HFO refrigerants requires clarification of their compatibility and dissolution behavior in refrigerating oils. Furthermore, when refrigerant mixtures are used, it is important to understand the dissolution characteristics of each component in refrigerating oil and the resulting changes in the physical properties of the oil. Refrigerating oils suitable for the target refrigerant mixtures must therefore be developed and evaluated based on these findings. In addition, achieving smaller, lighter compressors requires developing metallic materials capable of supporting higher rotational speeds and elucidating friction, wear, and lubrication characteristics.

The research and development activities reported in this chapter aimed to develop heat exchangers (including condensers and evaporators) and compressors compatible with low-GWP refrigerant mixtures and to establish design guidelines for these components. To this end, research and development efforts were focused on the following.

① Development of heat exchanger elemental technologies for suppressing heat transfer deterioration in low-GWP refrigerant mixtures

② Fundamental research on suppressing heat transfer deterioration in low-GWP refrigerant mixtures and development of heat exchanger application technologies

③ Improvement of evaporation and condensation performance of refrigerant mixtures through control of aluminum surface structures and application to heat transfer tubes

④ Elucidation of thermal-fluid mechanisms of low-GWP refrigerant mixtures and development of heat transfer enhancement technologies

⑤ Elucidation of refrigerant dissolution behavior in refrigerating oils in compressors, compatibility evaluation, and clarification of compression characteristics of low-GWP refrigerant mixtures

⑥ Elucidation of friction, wear, and lubrication characteristics in low-GWP refrigerant mixture atmospheres for improving compressor mechanical efficiency

⑦ Development of metal matrix composite materials suitable for compressor components and evaluation of their fundamental properties

1.2 Heat Exchangers

1.2.1 Research and development of heat exchanger elemental technologies for suppressing heat transfer deterioration in low-GWP refrigerant mixtures

This research and development item aimed to advance heat exchanger elemental technologies that account for temperature glide and phase-change heat transfer deterioration specific to refrigerant mixtures to overcome the heat transfer performance loss hindering the practical application of next-generation low-GWP refrigerant mixtures. Specifically, four topics were addressed: heat exchanger design and performance evaluation, measurement and modeling of refrigerant transport properties, construction of a heat transfer database and evaluation of correlations, and prediction of heat transfer coefficients using machine learning.

With regard to temperature glide and pressure loss, characteristic of refrigerant mixtures and affecting heat exchanger performance, the need for heat exchanger design guidelines distinct from those for pure refrigerants was examined. A heat exchanger comprising flat multiport tubes and corrugated fins was fabricated, and air-side pressure loss as well as condensation and evaporation heat transfer characteristics were evaluated experimentally. The results showed that the experimental data could be satisfactorily reproduced by modifying existing correlations. Furthermore, the conventional performance evaluation method based on the logarithmic mean temperature difference (LMTD) was found difficult to apply to refrigerant mixture systems. Accordingly, by introducing a numerical method that divides the heat exchanger into small regions, a new performance evaluation method accounting for local heat transfer and temperature distributions was established.

For refrigerant transport properties, viscosity and thermal conductivity were measured. By optimizing the parameters of a model based on the extended corresponding states (ECS) principle, a calculation model was developed that reproduces property values for new low-GWP refrigerants and refrigerant mixtures with an accuracy of ±1–2%.

Regarding the heat transfer database (RECDB), approximately 97,000 heat transfer and pressure-loss data points were systematically accumulated. A correlation evaluation function was developed, enabling the systematic organization of knowledge and the advancement of design guidelines for a wide range of refrigerants and heat transfer conditions. In addition, a machine-learning-based prediction model for heat transfer coefficients was constructed using large-scale data, achieving higher prediction accuracy than conventional empirical correlations. Furthermore, SHAP analysis quantitatively clarified that refrigerant type and tube geometry are dominant factors.

Through these outcomes, an evaluation framework integrating experiments, thermophysical properties, databases, and machine learning was established as a fundamental technology for designing heat exchangers compatible with new low-GWP refrigerant mixtures. These results contribute to greenhouse gas emission reduction through the high-efficiency use of low-GWP refrigerants and the energy conservation of refrigeration and air-conditioning equipment.

1.2.2 Fundamental research on suppressing heat transfer deterioration in low-GWP refrigerant mixtures and development of heat exchanger application technologies

This research and development item clarified the factors responsible for heat transfer deterioration in low-GWP zeotropic refrigerant mixtures and established technologies for suppressing such deterioration and enhancing heat transfer. First, condensation and evaporation heat transfer characteristics were evaluated in parallel microchannels simulating flat multiport tubes. The results showed that, compared with the pure refrigerant R1234yf, the heat transfer coefficient of the refrigerant mixture R474A decreased by 30–40% during condensation and by 15–50% during evaporation. These findings quantitatively demonstrated that mass diffusion resistance is the principal cause of heat transfer deterioration in zeotropic refrigerant mixtures. In addition, visualization of flow patterns and liquid film

structures showed that heat transfer deterioration becomes particularly pronounced under low mass velocity conditions.

Furthermore, technologies for suppressing heat transfer deterioration were investigated with a focus on optimizing heat transfer surface characteristics and flow-channel structures. A porous layer formed by anodizing promoted bubble nucleation and improved heat transfer performance by approximately 15% compared with a smooth surface under high heat-flux conditions; under some conditions, the performance exceeded that of a pure refrigerant. With respect to flow-channel structures, inclined microfin channels promoted flow mixing and disrupted the concentration boundary layer, enhancing heat transfer by a factor of 1.3–2.7 relative to parallel microchannels, even under low mass velocity conditions. It was also confirmed that dryout was suppressed in microfin channels and that stable heat transfer performance was maintained through enhanced rewetting.

Through these results, the occurrence conditions and dominant factors governing heat transfer deterioration in zeotropic refrigerant mixtures were clarified. Effective knowledge was also obtained on suppressing heat transfer deterioration and enhancing heat transfer through optimized surface treatment and flow-channel geometry. These findings are expected to contribute to establishing design guidelines for high-performance heat exchangers compatible with low-GWP refrigerant mixtures.

1.2.3 Research and development on improving the evaporation and condensation performance of refrigerant mixtures by controlling the surface structure of aluminum and applying the technology to heat transfer tubes

This research and development item established heat transfer enhancement technologies based controlling the surface structure of aluminum multiport tubes and optimizing flow-channel structures, to address the heat transfer performance loss associated with using low-GWP zeotropic refrigerant mixtures. First, a nanoscale porous oxide film was formed on the aluminum surface by anodizing, and its structure was successfully controlled. The resulting oxide film had a porous structure with a thickness of approximately 700 nm and a pore diameter of approximately 70 nm. Evaluation of the film as a boiling heat transfer surface confirmed an approximately 13% improvement in the heat transfer coefficient compared with an untreated surface under conditions using the refrigerant mixture R454C. In addition, bubble refinement resulting from enhanced bubble nucleation was observed, demonstrating that controlling the surface microstructure effectively enhances boiling heat transfer in refrigerant mixtures.

By contrast, verifying whether surface treatment could be practically applied to the inner walls of multiport tubes revealed that, when a simple electrolytic immersion method was used, ion diffusion into the flow channels became rate-limiting, resulting in substantially nonuniform oxide film formation on the inner walls compared with the outer surface. Although improvements were attempted by masking the outer surface and introducing auxiliary electrodes, reactions were concentrated near the channel inlets and localized dissolution occurred, confirming the difficulty of achieving uniform treatment in long, closed flow channels. These findings indicate that a new surface treatment process is needed for the inner walls of multiport tubes, such as one combined with forced flow of electrolyte through the channels.

As another approach to improving heat transfer performance, the cross-sectional geometry of multiport tubes was examined, and flow-channel designs intended to retain liquid films and suppress dryout were investigated and prototyped. This work presented a design strategy for suppressing heat transfer deterioration in refrigerant mixtures from the complementary perspectives of surface structure and flow-channel geometry.

Through these outcomes, the heat transfer enhancement effect achieved by forming nanoscale porous structures on aluminum surfaces was clarified, and technical challenges in applying this treatment to the inner walls of multiport tubes were identified. These findings provide a foundation for heat transfer tube design and surface treatment technologies aimed at realizing high-performance heat exchangers compatible with low-GWP refrigerant mixtures.

1.2.4 Research and development on elucidating the thermal-fluid mechanisms of low-GWP refrigerant mixtures and heat transfer enhancement technologies

This research and development item conducted experimental and theoretical investigations of the thermal-fluid characteristics of two-phase flow in microchannels, unstable evaporating flow in parallel channels, and nucleate boiling characteristics, to clarify the causes of reduced heat transfer performance in low-GWP zeotropic refrigerant mixtures and to establish heat transfer enhancement technologies.

The flow characteristics of gas–liquid two-phase flow in microchannels with an inner diameter of 1 mm were evaluated, and the flow patterns, void fraction, and pressure loss were systematically organized for the pure refrigerant R1234yf and the zeotropic refrigerant mixture R454C. The results clarified that the observed flow patterns generally agreed with existing classifications based on the Weber number, whereas refrigerant mixtures required a higher gas-phase velocity for transition to annular flow. In addition, the void fraction was lower than values predicted by existing correlations, and this tendency was particularly pronounced for refrigerant mixtures. Although the pressure loss could be organized using the Lockhart–Martinelli method, refrigerant mixtures tended to exhibit lower values than the predicted values, suggesting the influence of nonequilibrium states and temperature variation.

For evaporating flow in parallel small-diameter channels simulating flat multiport tubes, the effects of inlet conditions and header structure on flow distribution and heat transfer characteristics were determined. The results confirmed that, under constant inlet pressure conditions, increasing the header volume destabilized the flow and induced oscillatory flow and reverse flow. This oscillatory flow was found to suppress nucleate boiling and reduce the heat transfer coefficient in the low-quality region, whereas in the high-quality region it promoted rewetting of dry patches and thereby suppressed heat transfer deterioration.

Evaluation of nucleate boiling characteristics through pool boiling experiments showed that, for the zeotropic refrigerant mixture R454C, the superheat at the onset of boiling was approximately 22 K, which was higher than that of pure refrigerants, and that the heat transfer coefficient decreased by approximately 40% even in the developed nucleate boiling region. This decrease is considered to result from changes in the concentration distribution near the gas–liquid interface, which increase the interface temperature and suppress evaporation. Meanwhile, the composition ratio of the refrigerant mixture was varied, revealing that, although the effect on the superheat at the onset of boiling was small, increasing the proportion of the low-boiling-point component improved the nucleate boiling heat transfer coefficient.

Through these results, the thermal-fluid behavior and boiling phenomena of refrigerant mixtures in microchannels were systematically clarified, and the potential for heat transfer enhancement through liquid film agitation using oscillatory flow and nucleate boiling was demonstrated. These findings provide a foundation for designing high-performance heat exchangers compatible with low-GWP refrigerant mixtures and are expected to contribute to further development of heat transfer enhancement technologies and design guidelines.

1.3 Compressors

1.3.1 Elucidation of refrigerant dissolution behavior in refrigerating oils in compressors, compatibility evaluation, and compression characteristics of low-GWP refrigerant mixtures

This research and development item aimed to ensure the performance and reliability of compressors using low-GWP zeotropic refrigerant mixtures by clarifying fundamental aspects of refrigerant–refrigerating oil dissolution behavior, oil return characteristics, and blended-refrigerant compression characteristics, and by establishing compressor design guidelines that incorporate these factors.

To characterize the dissolution behavior of refrigerating oils and refrigerants, solubility, refractive index, and volume change were measured over the range of 30–90 °C for POE oil, PVE oil, the refrigerant mixture R454C, and its constituent components. The results showed that refrigerant dissolution induces volume contraction, in which the

mixture volume becomes smaller than the theoretical value, and that this effect is particularly pronounced at a refrigerant mass fraction of approximately 50%. It was also confirmed that the refractive index varies with refrigerant concentration and temperature, and that two-phase separation and supercritical-like behavior occur in the high-temperature region. Furthermore, analyzing the dissolution behavior of each component revealed that, under high-temperature conditions, R1234yf, which has higher molecular polarity, preferentially dissolves in the refrigerating oil, resulting in compositional segregation. These findings are important for elucidating the factors responsible for property changes and performance variations inside compressors.

For oil return characteristics, the liquid film thickness in annular two-phase flow in a vertical upward tube was measured using an optical-fiber liquid film sensor, and the liquid film structure and transport mechanism were characterized. The results showed that the conventional Blasius equation overestimates the liquid film thickness, whereas the Wallis equation can accurately predict the base liquid film thickness. It was further clarified that, for high-viscosity liquids, the amount transported by the base liquid film has an upper limit and that excess liquid is transported by surface waves, providing important knowledge for quantifying the oil return mechanism.

For compressor characteristics, a model accounting for composition changes in refrigerant mixtures was constructed, and quasi-steady analyses were conducted by considering the energy balance and losses in the suction, compression, and discharge processes. The model reproduced measured data for the conventional refrigerant R22 within approximately ±10% for refrigerant mass flow rate, compressor power, volumetric efficiency, and overall efficiency. In addition, for R32/R1234yf refrigerant mixtures, increasing the R32 fraction was found to reduce the suction density, thereby decreasing refrigerant mass flow rate and volumetric efficiency; the influence of composition change on compressor performance was thus quantitatively demonstrated.

In addition, investigations were conducted on increasing compressor rotational speed to compensate for the low volumetric refrigeration capacity of low-GWP refrigerants, and issues such as vane jumping, shaft deflection, and increased discharge loss were identified. To address these issues, reducing inertial force through lightweight materials and structural optimization was shown to be effective. Theoretical analysis further demonstrated that reducing vane weight increases the limiting rotational speed at which jumping occurs. Moreover, a prototype compressor incorporating lightweight composite materials was designed and fabricated, establishing a foundation for evaluation using an actual machine.

Through these outcomes, the refrigerant–oil system behavior, oil return mechanism, and compression characteristics in compressors using low-GWP refrigerant mixtures were systematically clarified, and a foundation for design guidelines, including high-speed operation, was established. This research provides important knowledge contributing to efficiency increment and downsizing of compressors compatible with low-GWP refrigerants.

1.3.2 Elucidation of friction, wear, and lubrication characteristics in low-GWP refrigerant mixture atmospheres for improving compressor mechanical efficiency

This research and development item determined the friction, wear, and lubrication characteristics of compressor sliding parts and established a foundation for improving mechanical efficiency, to suppress performance degradation in compressors using low-GWP refrigerant mixtures and achieve higher efficiency through high-speed operation. For the rolling-piston rotary compressor targeted in this study, test apparatuses reproducing the sliding conditions between the vane and cylinder groove and between the vane and rolling piston were developed, and friction characteristics were experimentally evaluated in a low-GWP refrigerant mixture atmosphere.

The results showed that, in all sliding parts, the friction coefficient depends on the dimensionless bearing characteristic number, remaining nearly constant in the low-bearing-number region and decreasing in the high-bearing-number region. For material effects, combinations of cast iron components exhibited the lowest friction, whereas composite materials tended to slightly increase the friction coefficient. However, for combinations involving composite materials, rolling contact became dominant and sliding velocity decreased, suggesting the sliding state could be

improved. In addition, abnormal wear caused by aggregation of ceramic particles was observed in the composite materials, and issues related to material design were identified.

Furthermore, investigating mechanical efficiency using the obtained friction coefficient data revealed that friction coefficients comparable to those reported previously were observed in the low-bearing-number region, whereas the friction coefficient decreased sharply in the high-bearing-number region. This characteristic is important for predicting compressor performance during high-speed operation and indicates that improving the accuracy of friction characteristics is essential for evaluating mechanical efficiency.

Through these outcomes, the friction and wear characteristics of compressor sliding parts in low-GWP refrigerant mixture environments were systematically clarified, and a foundation was established for loss evaluation and optimal design during high-speed operation. This research provides important knowledge contributing to the higher efficiency of compressors compatible with low-GWP refrigerants.

1.3.3 Development of metal matrix composite materials suitable for compressor components and evaluation of their fundamental properties

This research and development item developed lightweight, high-rigidity aluminum matrix composite materials (metal matrix composites; MMCs) intended for application to compressor rotating components and evaluated their fundamental properties, to achieve higher efficiency and smaller and lighter compressors compatible with low-GWP refrigerant mixtures. Target properties were established based on cast iron FC250, and materials were developed through reinforcement design based on the rule of mixtures and optimized particle dispersion.

The developed material, MMC02N, achieved a density of approximately 2.73 g/cm³, corresponding to a weight reduction of approximately 60% compared with conventional cast iron. At the same time, it achieved a tensile strength of 360 MPa, Young's modulus of 120 GPa, and fatigue strength of 133 MPa, demonstrating mechanical properties superior to those of cast iron. In particular, optimizing the shape and particle size of the reinforcing particles improved fatigue strength, which had previously been a key issue. Fracture surface observations showed that the particle dispersion state and interfacial characteristics markedly affect strength properties, and important factors for material design were identified. Furthermore, machinability evaluation confirmed that, although the developed material exhibited higher cutting resistance and cutting temperature than conventional materials, tool wear was reduced by approximately 30%. In particular, applying diamond tools was shown to suppress wear and stabilize machined surface quality, demonstrating applicability to machining processes.

In addition, rolling pistons and vanes fabricated from the developed material were prototyped and supplied to other research organizations, enabling evaluation of friction and wear characteristics and investigation of their applicability to compressor design.

Through these outcomes, metal matrix composite materials combining weight reduction with high strength and high rigidity were successfully developed, and a foundation was established for material technologies aimed at smaller, lighter, and higher-speed compressors. This research contributes to improving the efficiency of equipment compatible with low-GWP refrigerants.

1.4 Summary

The research reported in this chapter was conducted to support the practical application of next-generation low-GWP refrigerant mixtures in response to the Kigali Amendment. To overcome the reduction in heat exchanger performance caused by temperature glide and mass-transfer resistance specific to refrigerant mixtures and to ensure the performance and reliability of compressors using such refrigerants, elemental technologies related to heat exchangers and compressors were developed in an integrated manner. In this project, comprehensive research and development were carried out through collaboration among multiple institutions on the following topics: (1) elucidation of heat transfer deterioration mechanisms in refrigerant mixtures and development of technologies for suppressing such deterioration,

(2) heat exchanger design and performance evaluation, (3) measurement and modeling of refrigerant transport properties, (4) prediction using heat transfer databases and machine learning, (5) evaluation of refrigerant–oil system characteristics in compressors and clarification of blended-refrigerant compression characteristics, (6) improvement of compressor mechanical efficiency, and (7) development of materials for compressor components.

First, it was clarified that, during condensation and evaporation of refrigerant mixtures, heat transfer deterioration occurs owing to mass-diffusion resistance, resulting in decreases in the heat transfer coefficient of approximately 30–40% during condensation and approximately 15–50% during evaporation compared with those of pure refrigerants. In addition, flow patterns, void fraction, pressure loss, and nucleate boiling characteristics in microchannels were systematically evaluated. The results demonstrated that refrigerant mixtures exhibit lower void fractions, a higher boiling incipience superheat of approximately 22 K, and reductions in the heat transfer coefficient of up to approximately 40%. Furthermore, the effects of flow instability and oscillatory flow in parallel channels on heat transfer characteristics were clarified, and the potential for heat transfer enhancement through rewetting effects was demonstrated.

For heat exchanger technologies, performance evaluation was conducted through experiments and numerical analyses using a heat exchanger composed of flat multiport tubes and corrugated fins. The limitations of applying the conventional LMTD method were demonstrated, and a segmented analysis method accounting for local heat transfer was developed. In addition, efforts to suppress heat transfer deterioration focused on optimizing surface and flow-channel structures. As a result, heat transfer improvements of approximately 10–15% using porous surfaces and enhancement effects of 1.3–2.7 times using microfin channels were confirmed. Simultaneously, technical issues for practical application, including the difficulty of uniformly treating the inner walls of multiport tubes, were identified. Furthermore, a database (RECDB) comprising approximately 97,000 heat transfer and pressure-loss data points was constructed, a correlation evaluation function was developed, and a machine-learning-based heat transfer coefficient prediction model was created, achieving higher accuracy than conventional correlations.

For refrigerant transport properties, high-accuracy measurements of viscosity and thermal conductivity, combined with modeling based on the ECS principle, enabled the development of models that predict measured values for new refrigerants and refrigerant mixtures with errors of approximately ±1–2%.

For compressor technologies, the dissolution characteristics, composition changes, and oil return characteristics of refrigerant–refrigerating-oil mixtures were clarified. These results demonstrated that compositional segregation and liquid-film transport behavior specific to refrigerant mixtures affect compressor performance. In addition, the friction and wear characteristics of sliding parts were experimentally evaluated, showing that the friction coefficient varies depending on the dimensionless bearing characteristic number and that friction characteristics have a considerable effect on mechanical efficiency under high-speed operating conditions. Furthermore, although composite materials suggested the possibility of increased rolling contact and reduced wear, issues such as abnormal wear caused by the materials' internal structure were identified.

As a compressor material technology, aluminum matrix composite materials intended for compressor components were developed. These materials achieved a density of 2.73 g/cm^3, corresponding to an approximately 60% reduction in weight compared with that of conventional cast iron, while also achieving a tensile strength of 360 MPa, Young's modulus of 120 GPa, and fatigue strength of 133 MPa, thereby confirming improved mechanical properties. In addition, machinability evaluation showed that tool wear could be reduced by approximately 30%, although cutting resistance increased, clarifying their applicability in terms of machinability and wear resistance.

Through these outcomes, an integrated evaluation framework encompassing heat-transfer phenomena, flow characteristics, thermophysical properties, data science, materials, and mechanical elements was advanced as a fundamental technology necessary for designing heat exchangers and compressors compatible with new low-GWP refrigerant mixtures. These research outcomes are expected to promote the development and dissemination of refrigeration and air-conditioning equipment using low-GWP refrigerant mixtures, contribute to reducing the use of

HFC refrigerants, and support both the highly efficient use of such refrigerants and the energy conservation of refrigeration and air-conditioning equipment.

2. Research and Development of Heat Exchanger Elemental Technologies for Suppressing Heat Transfer Deterioration in Low-GWP Refrigerant Mixtures (Saga University)

2.1 Design and Performance Evaluation of Refrigerant–Air Heat Exchangers

2.1.1 Characteristics of heat exchange in refrigeration cycles using refrigerant mixtures

The most significant difference between zeotropic refrigerant mixtures and pure refrigerants is the occurrence of temperature variation, or temperature glide, during phase change. The magnitude of temperature glide depends on the combination of refrigerants, that is, on the difference in boiling points among the constituent components. For example, in R454A (R32/R1234yf: 35/65 mass%), R454B (R32/R1234yf: 68.9/31.1 mass%), and R454C (R32/R1234yf: 21.5/78.5 mass%) the temperature glide varies slightly depending on the operating temperature and pressure; however, within the range commonly used in air-conditioning equipment, it remains nearly constant at approximately 4 °C, 1 °C, and 5 °C, respectively. For these refrigerants, increasing the fraction of R1234yf tends to reduce GWP while increasing temperature glide. In addition, the refrigerant temperature inside the heat exchanger changes owing to frictional pressure loss. Although this effect depends on the refrigerant flow rate, the resulting temperature decrease cannot be neglected, particularly in condensation heat transfer, where the temperature gradients caused by temperature glide and pressure loss occur in the same direction. Figure 2.1-1 shows a schematic T-s diagram for cooling operation using R454C. As the figure shows, the temperature glide of the zeotropic refrigerant mixture requires a larger air–refrigerant temperature difference than for a pure refrigerant; consequently, compressor power—that is, the high–low pressure difference—increases. In addition, the evaporation and condensation heat transfer coefficients of refrigerant mixtures are considerably lower than those of pure refrigerants. Accordingly, when refrigerant mixtures are used in air-conditioning equipment, heat exchangers capable of achieving heat exchange with a smaller temperature difference are essential. In this research and development, prototype heat exchangers capable of accommodating such refrigerant mixtures were examined. This subsection reports part of the performance evaluation results for the new heat exchanger, namely air-side pressure loss and condensation heat transfer tests.

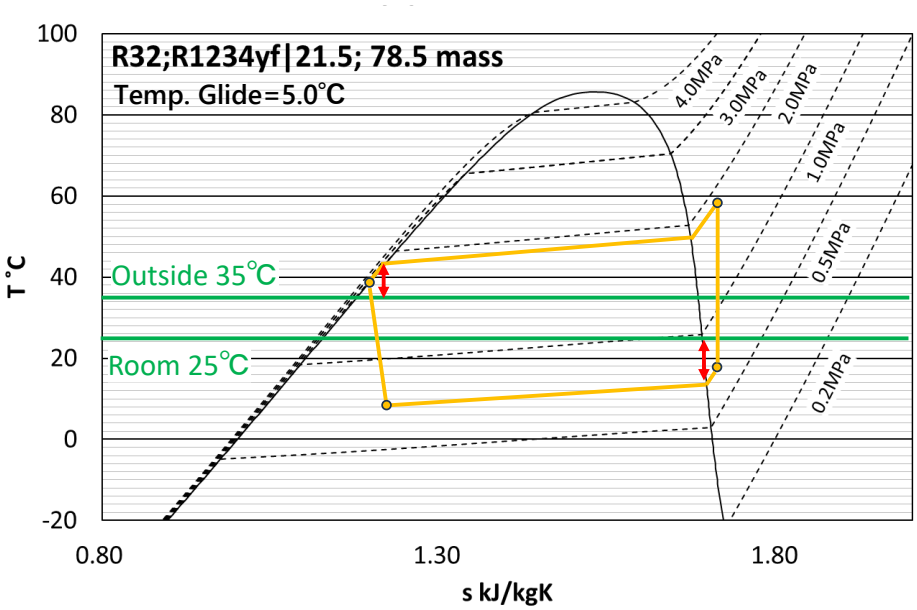

Figure 2.1-1 An example of refrigeration cycle of R454C on T-s diagram

2.1.2 Outline of apparatus and test heat exchanger

Figure 2.1-2 shows a schematic diagram of the test loop used to evaluate heat exchanger performance. The red line in the figure represents the refrigerant loop during the condensation test, whereas the blue line represents the air loop that exchanges heat with the refrigerant. Switching between evaporation and condensation tests is achieved by opening and closing valves in the refrigerant loop.

The refrigerant loop is driven by a compressor. The refrigerant discharged from the compressor is adjusted to a prescribed temperature, or degree of superheat, by a precooler. After its temperature and pressure are measured, the refrigerant flows into the test heat exchanger installed in the wind tunnel and exchanges heat with the air. Subsequently, after being sufficiently cooled to a compressed liquid state in the after-condenser and subcooler, the flow rate is measured using an ultrasonic flow sensor. The refrigerant is then depressurized by an expansion valve, adjusted to a prescribed degree of superheat in the evaporator, and returned to the compressor. The refrigerant temperature is adjusted by the compressor rotational speed and expansion valve opening, and the refrigerant flow rate is adjusted using a bypass installed between the compressor inlet and outlet.

In the air loop, the velocity, temperature, and humidity of the air flowing through the wind tunnel can be adjusted using the fan rotational speed, temperature controller, and dehumidifier/humidifier, respectively. The air temperature and velocity are measured using T-type sheathed thermocouples and a Pitot tube installed near the inlet and outlet of the test heat exchanger. Figure 2.1-3 shows photographs of the apparatus.

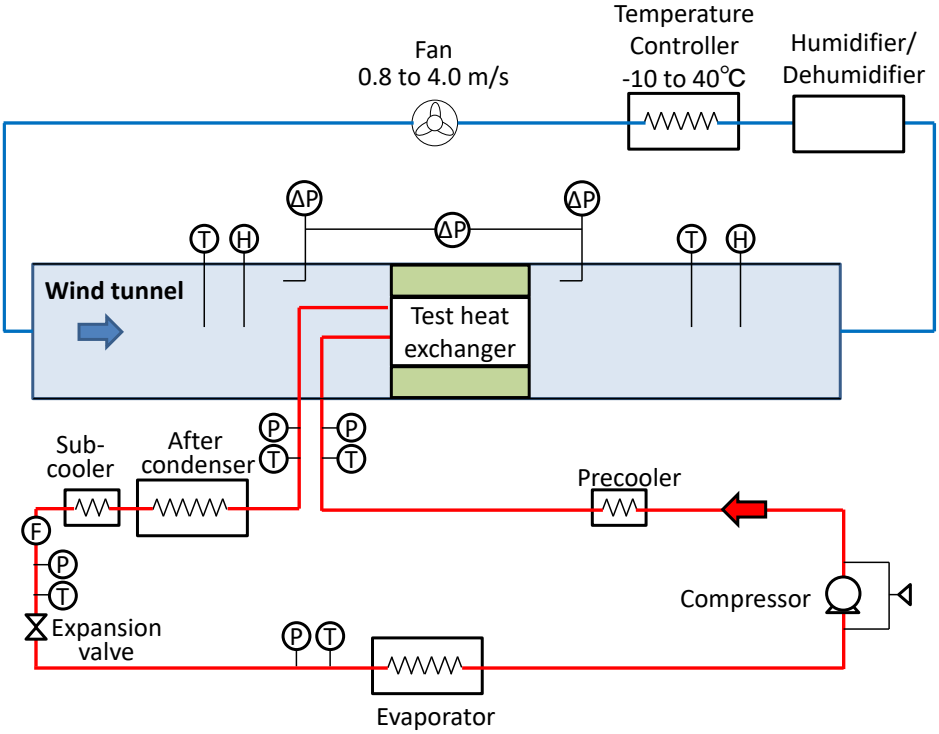

Figure 2.1-2 Schematic diagram of heat exchanger test loop

(a) Refrigerant circulation loop (b) Test section of wind tunnel

Figure 2.1-3 Photograph of experimental apparatus

Figure 2.1-4 shows a photograph of the test heat exchanger. The test heat exchanger consists of flat multiport tubes and corrugated fins, with a height of 250 mm and an effective heat transfer width of 400 mm. The refrigerant is distributed through a header to the flat multiport tubes. Corrugated fins with louvers are attached between the refrigerant flow channels to enhance heat transfer with air. The black portion in the photograph is thermal insulation, which is installed in the wind tunnel and also serves as a fixing frame for the heat exchanger, sealing the gap around the air flow passage once installed.

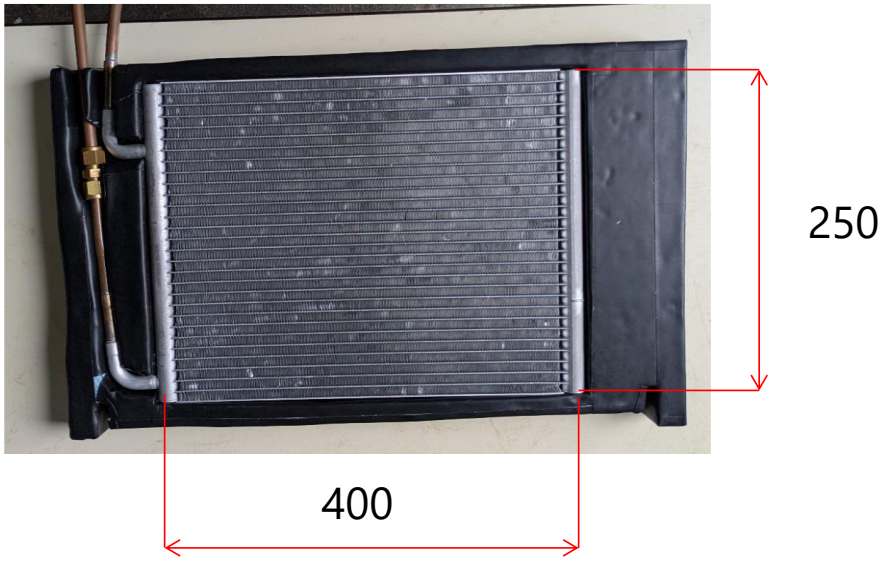

Figure 2.1-4 Photograph of test heat exchanger

2.1.3 Experimental conditions

In this research and development, R454C was used as the refrigerant. Details of R454C are shown in Table 2.1-1. R454C is a refrigerant mixture composed of R32, which is currently used mainly in residential air-conditioning equipment, and R1234yf, a candidate next-generation low-GWP refrigerant. It is characterized by a relatively low GWP among the R454 series; however, its temperature glide is the largest in this series. To establish a method for evaluating the performance of heat exchangers using the refrigerant mixture R454C, measurements were conducted for air-side frictional pressure loss, evaporation heat transfer characteristics, and condensation heat transfer characteristics. The test conditions are shown in Table 2.1-2. Frictional pressure loss was measured under conditions in which neither condensation nor frosting occurred; only air-side temperature and velocity were varied, under adiabatic conditions with no refrigerant flow. The air velocity and the evaporation and condensation heat exchange rates were set based on standard conditions for residential air-conditioning equipment and the size of the heat exchanger used in this research and development.

Table 2.1-1 Typical properties of R454C

Refrigerant	Composition	Mass fraction %	Boiling point °C	Temperature glide ° C	GWP	ASHRAE Class
R454C	R32/R1234yf	21.5/78.5	−45.5	5.0	146	A2L

Table 2.1-2 Experimental conditions

	Air-side velocity m s^{-1}	Air-side inlet Temp. °C	Refrigerant inlet Temp. °C	Heat exchange rate kW	Outlet Subcool Temp. °C	Outlet Superheat Temp. °C
Pressure drop	0.8 to 3.0	20 to 40	-	0 (Adiabatic)	-	-
Condensation	0.8 to 3.0	10 to 40	10 to 40	1.0 to 2.0	2	-
Evaporation	0.8 to 3.0	10 to 30	−10 to 10	1.0 to 2.0	-	4

2.1.4 Experimental results and discussion

Figure 2.1-5 shows the measurement results for frictional pressure loss. Figure 2.1-5(a) and (b) show the relationships between the air Reynolds number and frictional pressure loss and between the air Reynolds number and friction factor defined by Equation (2.1-1) (Wang *et al*., 2000), respectively.

$$f_{exp} = \frac{A_c}{A_o}\frac{\rho_m}{\rho_{in}}\left[\frac{2\Delta P_{\rho_{in}}}{G_c^2} - (1+\sigma^2)\left(\frac{\rho_{in}}{\rho_{out}} - 1\right)\right] \tag{2.1-1}$$

The results confirm that air-side pressure loss increases with Reynolds number, whereas the friction factor decreases. Based on the experimental data obtained, a correlation for the friction factor was examined. A satisfactory correlation was obtained by modifying coefficient C_1 in the friction factor correlation for louvered corrugated fins proposed by Wang *et al*. (2000), as shown in Equation (2.1-2).

Figure 2.1-6 shows the relationship between the examined correlation and the measured values.

$$f = C_1 Re^{F1}\left(\frac{P_t}{P_l}\right)^{F2}\left(\frac{F_p}{D_c}\right)^{F3} \tag{2.1-2}$$

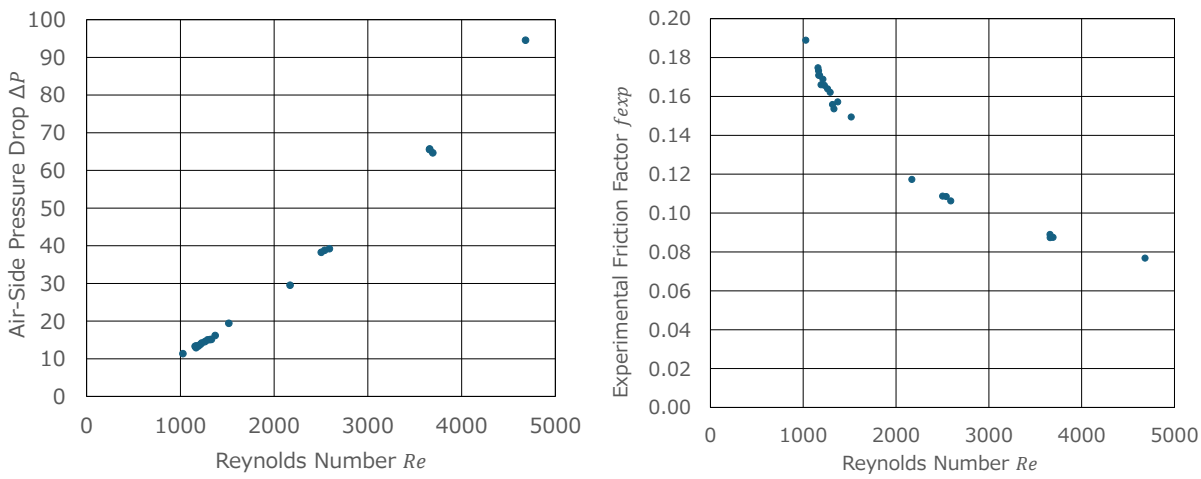

(a) Pressure loss (b) Friction factor

Figure 2.1-5 Experimental results of air-side pressure loss

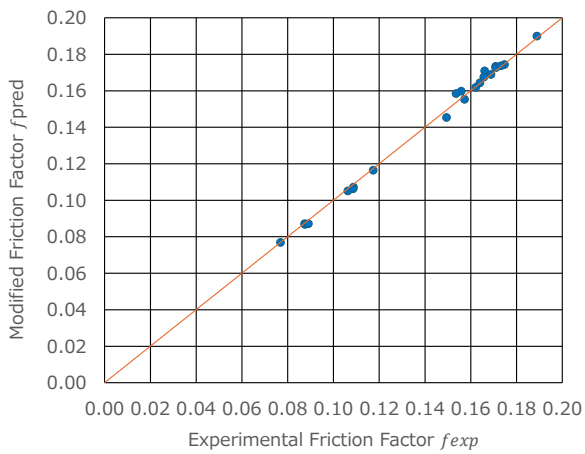

Figure 2.1-6 Comparison between predicted and experimental friction factors

As an example of the condensation test results, the *p–h* and *T–s* diagrams of the refrigeration cycle at an air velocity of 1.0 m s^{-1} are shown in Figure 2.1-7(a) and (b), respectively. The other conditions are indicated in the figure. The blue line indicates the change in refrigerant state in the test heat exchanger. The results confirm that the refrigeration cycle was operated appropriately, that the heat exchanger inlet and outlet were in single-phase states, and that the heat exchange rate could be calculated from the refrigerant enthalpy. Although the superheat at the compressor inlet appears excessive, this is attributable to flow-rate adjustment using the bypass between the compressor inlet and outlet. Under this condition, the heat exchange rate calculated from the refrigerant inlet and outlet enthalpies and mass flow rate was $Q = 2.17$ kW, and the temperature glide including refrigerant pressure loss was 7.6 °C. Measurements were conducted by varying the air-side velocity up to 3.0 m s^{-1}. The *KA* value, one of the heat exchanger performance evaluation indices, was calculated using Equation (2.1-3), based on the heat exchange rate Q, the logarithmic mean temperature difference ΔT_{lm} assuming counterflow, and the correction factor Ψ for application to crossflow.

$$KA = \frac{Q}{\Psi \Delta T_{lm}} \tag{2.1-3}$$

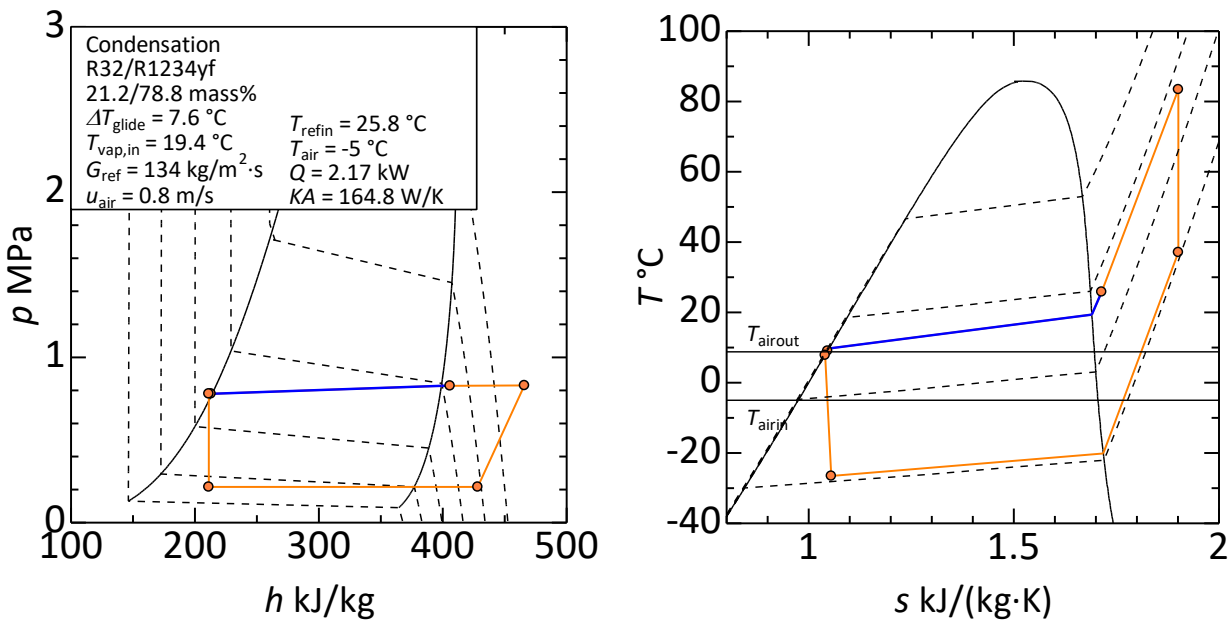

(a) *p–h* diagram (b) *T–s* diagram

Figure 2.1-7 Refrigeration cycle during a condenser test

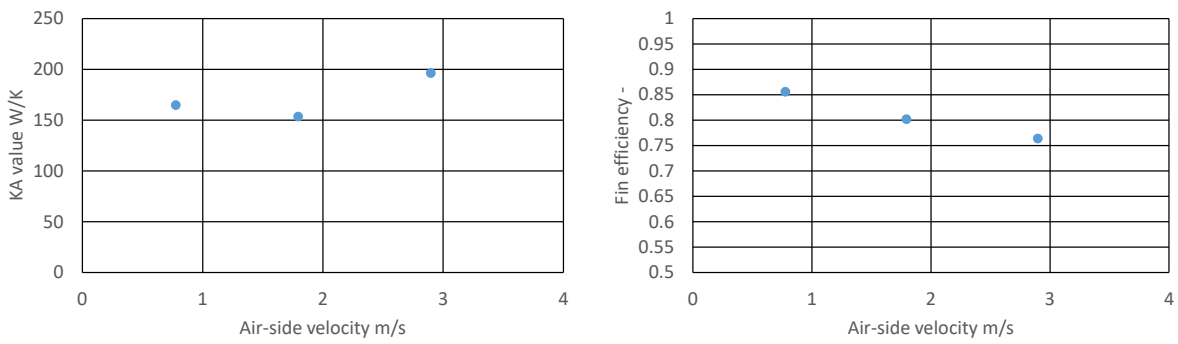

(a) *KA* value (b) Fin efficiency

Figure 2.1-8 Results of condenser performance test

The overall fin efficiency, including the fins and the outer surface of the heat transfer tubes, was also calculated by evaluating the air-side heat transfer coefficient using an existing heat transfer correlation for louvered corrugated-fin heat exchangers (Chang and Wang, 1997). Figure 2.1-8(a) and (b) show the relationships between air duct velocity and the *KA* value and between air duct velocity and fin efficiency, respectively. The results confirm that the *KA* value increases with air velocity, whereas fin efficiency tends to decrease.

Using the obtained *KA* value and fin efficiency, the refrigerant-side heat transfer coefficient α_{ref} was determined from Equation (2.1-4). Figure 2.1-9 shows the relationship between the refrigerant-side heat transfer coefficient and air velocity. The results show that the refrigerant-side heat transfer coefficient of this heat exchanger was less than 1000, which is smaller than the typical order of magnitude for refrigerant heat transfer coefficients in flat multiport tubes (Jige *et al*., 2023). This is considered to be attributable to the method used to calculate the *KA* value in this experiment. The *KA* value was calculated using the logarithmic mean temperature difference. The logarithmic mean temperature difference is derived under the assumption that the specific heat in the flow direction is constant, or that it can be regarded as infinite for two-phase flow. The results support the difficulty of applying this method to systems in which the refrigerant state changes from superheated vapor to subcooled liquid, such as the condensation process in a refrigeration cycle. As the evaporation test results showed a similar tendency, accurate calculation of the *KA* value using the logarithmic mean temperature difference is considered difficult for both condensation and evaporation.

$$\alpha_{ref} = \frac{1}{A_{ref}\left(\frac{1}{KA} - \frac{1}{\eta_0 \alpha_{air} A_{air}} - \frac{t}{\lambda_w A_w}\right)} \tag{2.1-4}$$

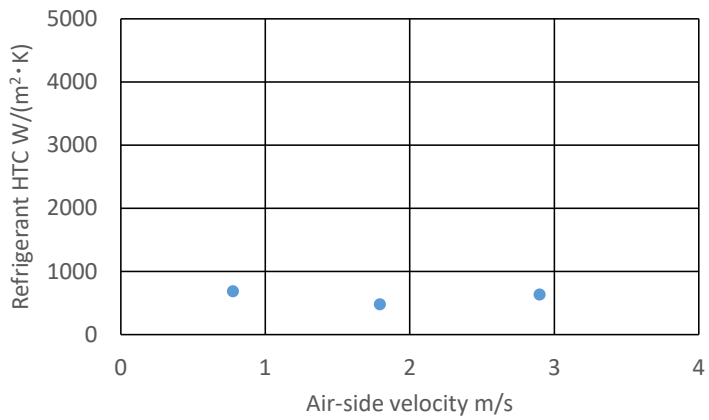

Figure 2.1-9 Condensation heat transfer coefficient evaluated from condenser tests

To calculate a more appropriate *KA* value, a numerical analysis approach was examined. Specifically, the heat exchanger was divided into small computational regions, and the local refrigerant heat transfer coefficient in each region was obtained by correcting existing heat transfer correlations. The correction factor for the heat transfer coefficient was determined iteratively so that the heat exchange rate obtained from the analysis agreed with the measured value. Furthermore, to account for the temperature decrease caused by refrigerant pressure loss, the local pressure loss in each computational region was also determined by correcting existing correlations to match the measured values. The results are shown in Figure 2.1-10. The obtained temperature distribution and heat transfer coefficient distribution exhibit qualitatively reasonable behavior, indicating that the analysis results are valid. In future work, the analysis will be extended to include evaporation test results, and a performance evaluation index for heat exchangers will be established. In addition, a calculation method that can flexibly analyze test results for different refrigerants will be developed.

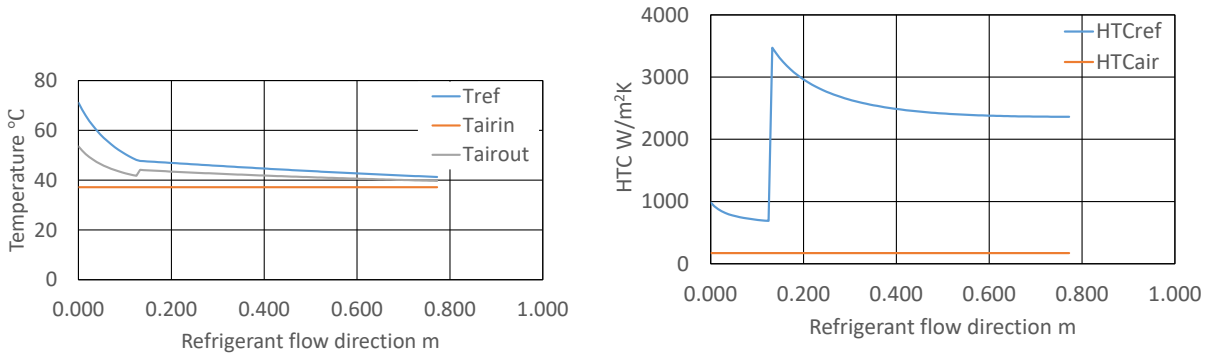

(a) Temperature distribution

(b) Local heat transfer coefficient

Figure 2.1-10 Analysis on local characteristics of a condenser test

2.2 Transport Properties of Refrigerants

2.2.1 Overview and status of measurements

Transport properties of refrigerants, namely viscosity and thermal conductivity, are essential for analyzing experimental data, designing heat exchangers, and conducting simulations of refrigeration and air-conditioning systems. For new refrigerants, accurate calculation models for predicting these properties from measured values must be developed. In this study, viscosity was measured using the tandem capillary tube method, and thermal conductivity was measured using the transient hot-wire method. Table 2.2-1 summarizes the measurement and calculation-model development status of viscosity and thermal conductivity reported in related publications. In the table, △ indicates refrigerants calculable using REFPROP (Lemmon *et al*., 2018) without measurement-based optimization, whereas × indicates refrigerants that cannot be calculated using REFPROP. For earlier measurements and calculation models, refer to Kariya (2026).

In REFPROP, which is widely used, viscosity and thermal conductivity are calculated based on the ECS principle proposed by Huber *et al*. (2003). In the ECS model, the transport properties of the target fluid are estimated from the equations of state of both the target and reference fluids—R134a, for refrigerants—together with the reference fluid's viscosity and thermal conductivity.

Table 2.2-1 Measurements and calculation models for refrigerants related to this project

	Viscosity			Thermal conductivity		
Refrigerant	Measure	Model	REFPROP	Measure	Model	REFPROP
Pure fluids						
R1132(E)	Duc *et al.* (2025)	Duc *et al.* (2025)	×	Taskira *et al.* (2026)	Taskira *et al.* (2026)	×
R13I1 or CF_3I	Tuhin *et al.* (2014a)	Tuhin *et al.* (2014a)	△	Tuhin *et al.* (2024b)	Tuhin *et al.* (2024b)	△
HFO1123			△	Silvia *et al.* (2025)	Silvia *et al.* (2025)	△
Mixtures						
R474A	Masumoto *et al.* (2025)		×			×
R454B	Duc *et al.* (2025)		△			△
R454C	Duc *et al.* (2025)		△	Owaleur *et al.* (2025)		△
HFO1123 + R32	Mondal *et al.* (2020)		△			△

2.2.2 Measurement method for viscosity and example measurements

Figure 2.2-1 shows the measurement principle of the tandem capillary tube method (Miyara *et al.*, 2019), which was used for viscosity measurement. By arranging two capillary tubes with different lengths in series, inlet and outlet losses in the capillaries can be canceled, enabling measurement of the pressure loss in the fully developed laminar-flow region.

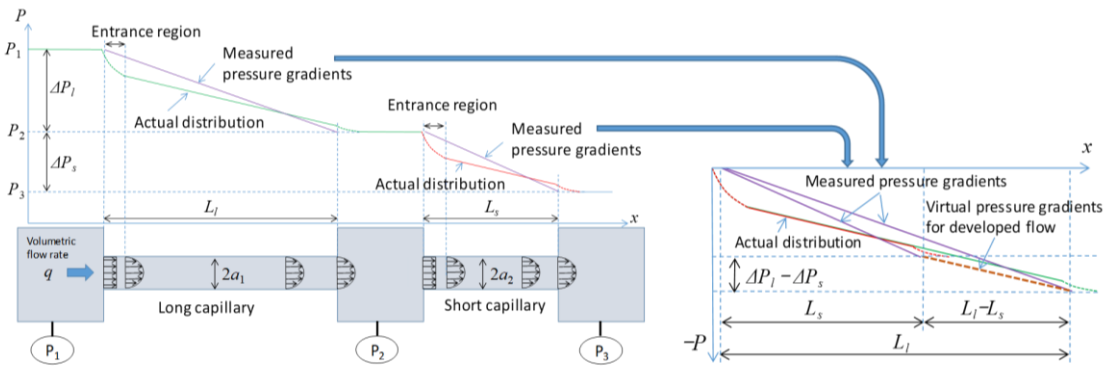

Figure 2.2-1 Measurement principle of measurement using tandem capillary tubes

As an example of the measurement results, Figure 2.2-2 shows the viscosity measurements for CF_3I. The symbols represent the measured values, and the dashed lines indicate values estimated using the ECS model in REFPROP. In REFPROP, partly because CF3I's parameters have not been adjusted using measured values, the predicted values are lower than the measured values.

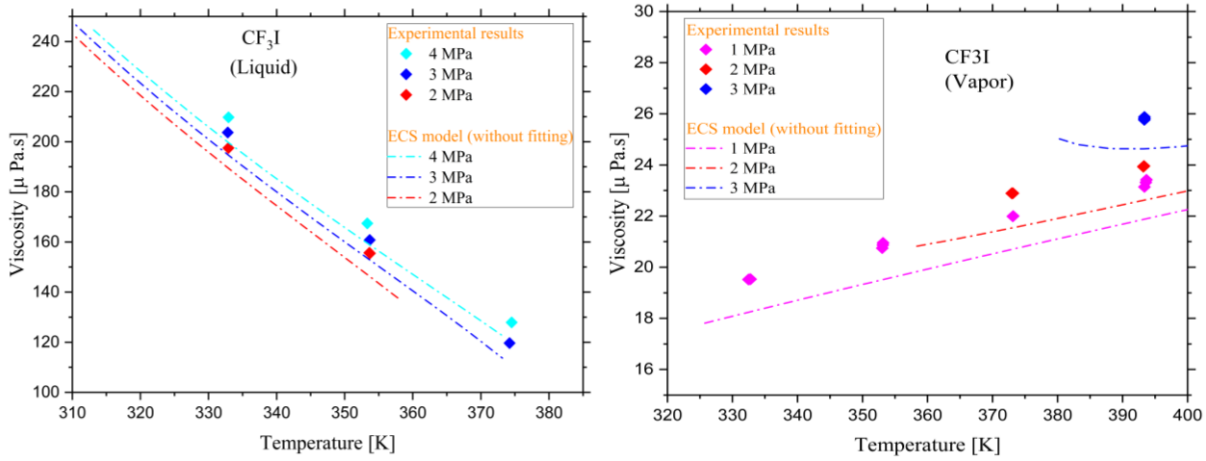

(a) Viscosity of liquid (b) Viscosity of vapor

Figure 2.2-2 Viscosity measurement of CF_3I

Figure 2.2-3 compares the measured values with the calculated values obtained using the ECS model after parameter adjustment. The adjusted ECS model predicted the measured values with an error of approximately ±1%. Figure 2.2-3(b) also includes results estimated using the residual entropy scaling (RES) method.

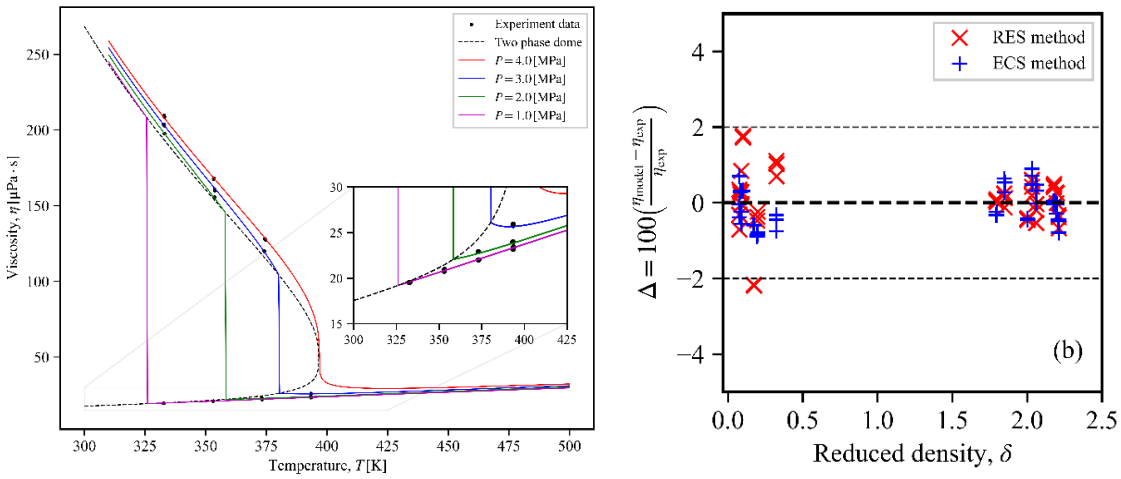

(a) Viscosity distribution as a function of temperature (b) Relative deviation plot

Figure 2.2-3 Viscosity calculations after parameter fitting

2.2.3 Measurement method for thermal conductivity and example measurements

Figure 2.2-4 shows the electrical circuit diagram of the transient hot-wire method used for thermal conductivity measurement and a schematic of the measurement apparatus. Two platinum wires with different lengths and a wire diameter of 15 μm, installed in a pressure vessel containing the refrigerant to be measured, were electrically heated in a step-function manner. The thermal conductivity was calculated by measuring the temporal change in wire temperature.

These platinum wires were incorporated into a Wheatstone bridge circuit, and the temperature change was obtained from the nonequilibrium potential difference.

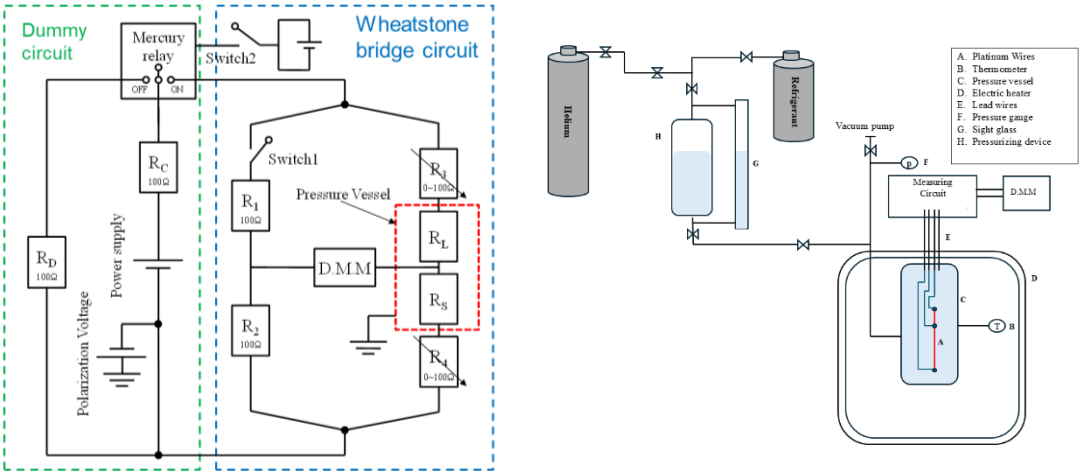

(a) Electrical circuit diagram (b) Schematic diagram of measuring apparatus

Figure 2.2-4 Thermal conductivity measurement using the transient hot wire method

Figure 2.2-5 shows results for R1132(E) as examples of measurement and parameter adjustment. As summarized in Table 2.2-1, R1132(E) cannot be calculated using REFPROP; however, calculations were performed by incorporating the equation of state developed under this NEDO project (Chapter 4 of Volume 2) into REFPROP. Figure 2.2-5(a) and (b) show prediction results before parameter adjustment of the ECS model used to calculate thermal conductivity; the predicted values were high for both the liquid and vapor phases. Figure 2.2-5(c) shows the prediction results after parameter adjustment, indicating good agreement between the calculated and measured values.

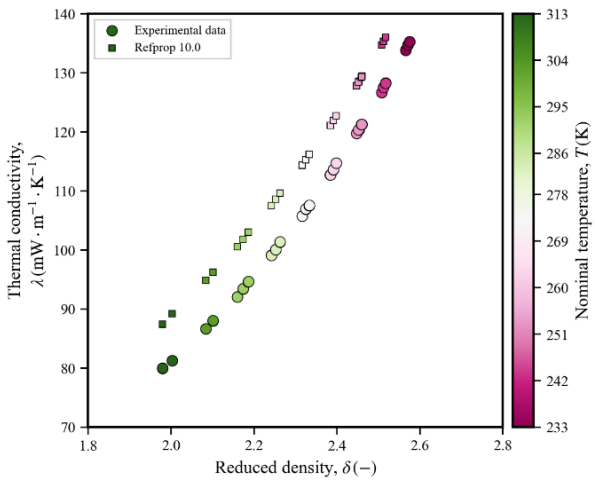

(a) Measured and calculated liquid thermal conductivity of R1132(E)

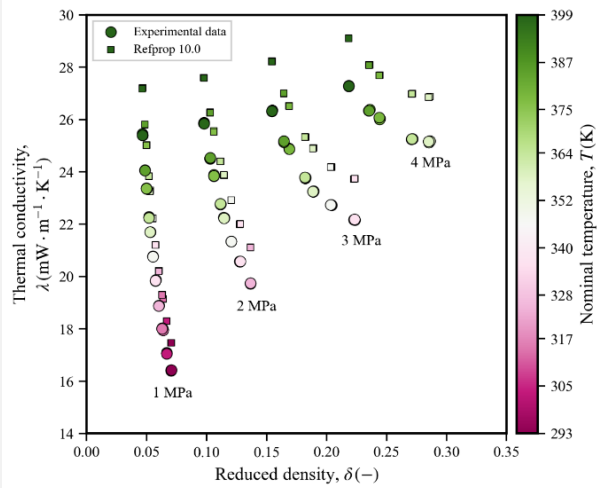

(b) Measured and calculated vapor thermal conductivity of R1132(E)

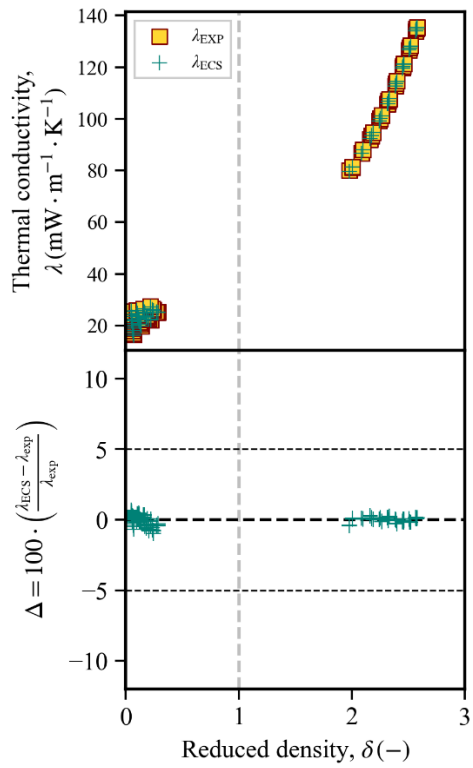

(c) Calculation values after parameter fitting and deviation plot for thermal conductivity of R1132(E)

Figure 2.2-5 Measured and calculated thermal conductivity of R1132(E)

2.2.4 Calculation model for transport properties: ECS model

In the ECS model, the temperature T_0 and density ρ_0 of the reference fluid corresponding to the temperature T and density ρ of the target fluid are obtained using the residual term α^r of the dimensionless Helmholtz free energy equation of state and the equation for the compressibility factor Z. In other words, the following simultaneous equations are solved.

$$\alpha^r(T,\rho) = \alpha_0^r(T_0,\rho_0) \tag{2.2-1}$$

$$Z(T,\rho) = Z_0(T_0,\rho_0) \tag{2.2-2}$$

Viscosity is considered here as an example of a transport property. The viscosity of a real gas, including the liquid-phase region, is expressed as the sum of the dilute-gas term $\eta_d(T)$, the residual term $\Delta\eta_r(T,\rho)$, and the critical enhancement term $\Delta\eta_c(T,\rho)$, as follows.

$$\eta(T,\rho) = \eta_d(T) + \Delta\eta_r(T,\rho) + \Delta\eta_c(T,\rho) \tag{2.2-3}$$

Here, $\eta_d(T)$ is adjusted based on a theoretically derived equation, and $\Delta\eta_c(T,\rho)$ is often neglected as the affected region is narrow and its magnitude is small. $\Delta\eta_r(T,\rho)$ is calculated using the ECS model as follows.

$$\Delta\eta_r(T,\rho) = +\Delta\eta_{r,0}(T_0,\rho_0\psi)F_\eta(T,\rho) \tag{2.2-4}$$

$F_\eta(T,\rho)$ is the shape factor for viscosity and is obtained by solving the simultaneous equations. ψ is an adjustable parameter expressed as a polynomial of density, and the polynomial coefficients are determined so that the measured and calculated values agree.

Thermal conductivity is calculated using a similar approach; however, as the variation near the critical point is extremely large, the critical enhancement is calculated using the model of Olchowy and Sengers (1989). For detailed descriptions of the ECS models for viscosity and thermal conductivity, refer to the literature (Huber *et al*., 2003; Morshed *et al*., 2024).

2.3 Heat Transfer Database

2.3.1 Collection and structure of heat transfer data

The heat transfer database (RECDB) developed in this study stores information on evaporation and condensation heat transfer and pressure loss in circular tubes, flat multiport tubes, and plate heat exchangers. The database includes experimental data obtained by research institutions participating in this NEDO project, as well as data collected from published literature. As of March 2026, more than 97,000 data points had been accumulated.

Figure 2.3-1(a) shows the procedure for recording heat transfer data and the data structure compiled in Excel sheets. All information related to heat transfer, including tube geometry, temperature, pressure, mass velocity, vapor quality, and thermophysical properties, is recorded in the same row and linked to each individual heat transfer coefficient data point. Information extracted from a single paper is compiled into one Excel file and registered in RECDB, a Web-based heat transfer database system. Figure 2.3-1(b) shows an example of experimental in-tube evaporation values registered in RECDB, displayed for several refrigerants. The Web-based system enables users to search and display heat transfer data, filter data by specified conditions, and access bibliographic information for the corresponding papers.

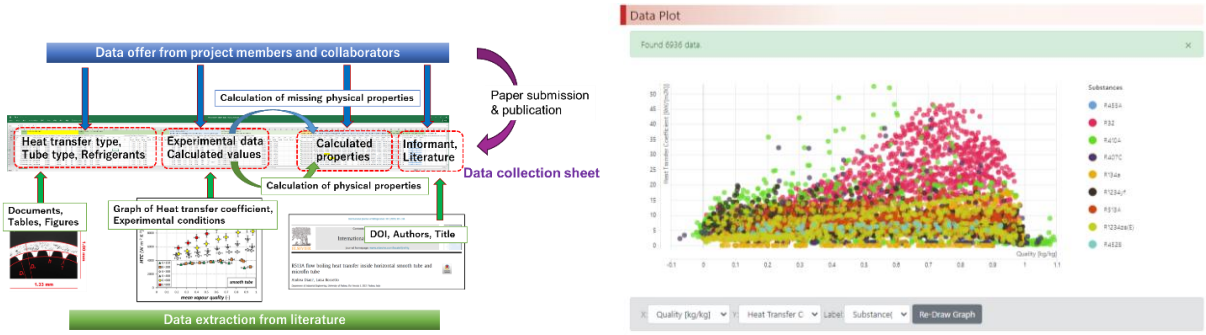

(a) Data collection and structure (b) Data display for in-tube evaporation as an example

Figure 2.3-1 Web system of heat transfer database (RECDB) for data collection and data analysis

2.3.2 Correlation evaluation function

As a new RECDB function, a correlation evaluation tool is under development. Although this function is still being developed and has not yet been released publicly, Figure 2.3-2 presents an example comparing experimental values with a correlation for in-tube condensation heat transfer for various refrigerants. The correlation is intended to predict the condensation heat transfer coefficient in smooth tubes. As the experimental dataset includes not only smooth-tube data but also internally grooved-tube data and pressure-loss data without corresponding heat transfer coefficient values, the overall data scatter is large. However, by using the RECDB data selection function, the dataset can be screened

appropriately, and the intended evaluation can be performed.

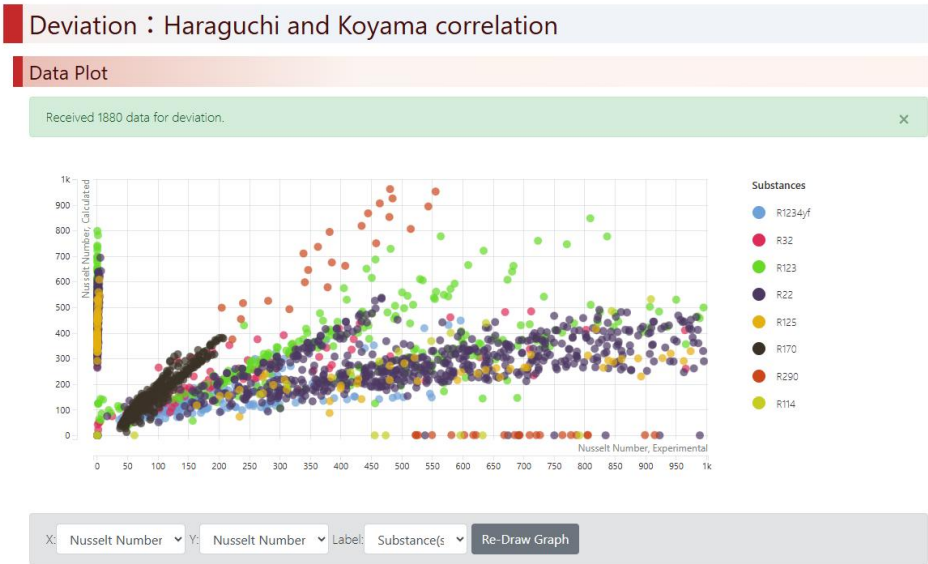

Figure 2.3-2 Correlation evaluation function

2.4 Prediction of Heat Transfer Coefficients Using Machine Learning

2.4.1 Machine learning and workflow

In this study, a new approach to predicting heat transfer coefficients was adopted, as shown in Figure 2.4-1. Information accumulated in the heat transfer database RECDB described in Section 2.3, including heat transfer coefficients, refrigerant types, heat transfer tube information, and thermophysical properties, served as the machine learning dataset. Machine learning was performed using these heat transfer data, and 27 model types were compared to identify the one with the highest prediction accuracy. The results are expected to enable highly accurate prediction of heat transfer coefficients, thereby contributing to resolving energy conservation issues.

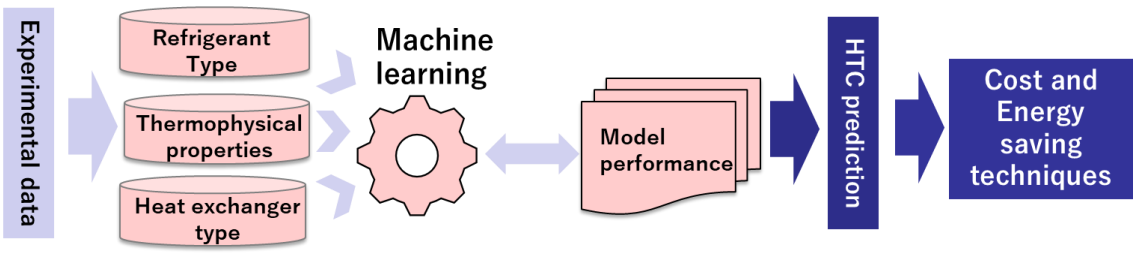

Figure 2.4-1 Proposed workflow for the machine learning approach

2.4.2 Prediction models used for machine learning

To clarify the relationships between input variables, such as flow conditions and thermophysical properties, and the heat transfer coefficient (HTC), machine-learning-based prediction models were constructed. Many correlations proposed to date have been derived from experimental data under limited conditions; accordingly, their applicability is restricted when refrigerant properties, heat transfer conditions, or heat exchanger geometries differ. By contrast, machine learning can provide highly accurate and broadly applicable predictions by learning nonlinear and complex

relationships from large-scale datasets. In this study, several representative machine learning methods were examined, and their predictive performance compared. In particular, three methods were investigated: linear regression (LR), wide neural network (WNN), and support vector machine (SVM).

Linear regression is the most basic statistical model and assumes a linear relationship between input variables and the output. It offers high interpretability and low computational cost. However, for problems involving strong nonlinearity, such as heat transfer phenomena, achieving sufficient accuracy may be difficult. Therefore, it was used as a baseline model.

A wide neural network (WNN) is an artificial neural network that achieves high expressive capability through a large number of neurons in each hidden layer. Whereas conventional deep networks emphasize depth, WNNs increase layer width to efficiently learn features from complex, high-dimensional data. This structure enables accurate capture of nonlinear interactions and multivariable dependencies in thermal-fluid phenomena. However, as the number of parameters increases, appropriate regularization and learning-condition settings are important to reduce the risk of overfitting and increased computational cost.

A support vector machine (SVM) is a method that performs regression and classification by mapping input data into a high-dimensional space and constructing an optimal separating hyperplane. By using kernel functions, such as polynomial and radial basis function (RBF) kernels, SVM can flexibly handle data that are difficult to separate linearly in the original space. As SVM exhibits high generalization performance even for relatively small datasets and is effective for nonlinear problems, it was included among the models examined.

These machine learning models enable comprehensive learning of the complex relationships between input parameters, including refrigerant type, thermophysical properties, thermal-fluid conditions, and heat exchanger geometry, and the heat transfer coefficient. By comparing and evaluating multiple models, this study aimed to identify the most accurate prediction model and establish a new design method that can complement or replace conventional empirical correlations.

2.4.3 Heat transfer data

This subsection reports the results obtained using a dataset comprising 22,608 experimental data points for saturated flow boiling conditions involving 18 pure refrigerants. The dataset covers diverse experimental conditions and heat exchanger configurations and therefore has practical and broad applicability. Refrigerant type, tube geometry, and heat exchanger configuration were treated as categorical variables so that differences among these variables were appropriately reflected in the model.

Each data point includes experimental conditions such as refrigerant type, saturation temperature, wall temperature, pressure, vapor quality, mass flux, and tube diameter, as well as tube type and heat exchanger type. Thermophysical properties in the liquid and vapor phases, including density, viscosity, surface tension, specific heat, and thermal conductivity, were also included, and model training was performed using a total of 20 input variables.

Table 2.4-1 shows the refrigerant types and experimental conditions of the heat transfer data used in this study. The dataset includes a large number of data points for R32 (3,609 points), R134a (3,100 points), R245fa (2,392 points), and R744 (2,387 points). Refrigerants with different thermophysical properties, including conventional and low-GWP refrigerants, are included in a balanced manner, enabling machine learning with high predictive performance and broad generality.

Table 2.4-1 Experimental parameters considered in the database

Refrigerant	T_{sat} [°C]	T_{wall} [°C]	Pressure [MPa]	Vapor Quality [x]	Mass Flux [kg/m²s]	Hidraulic Diameter D_h [mm]	Liquid Thermal Conductivity λ_l [mW/m· K]	Liquid Density ρ_l [kg/m³]	Boiling Data Points
R11	57–75	69–85	0.29–0.47	0−0.99	150–560	1.95	72.8–77.6	1348–1395	100
R123	49–81	51–132	0.208–0.50	−0.3–0.85	167–470	0.19–1.95	62.4–70	1306–1399	213
R1233zd(E)	25–145	0–173	0.129–2.49	0–0.9	30–1000	0.650–6	51.3–82.7	842–1263	1371
R1234yf	6–41	6–60	0.385–1.04	0–0.99	50–940	0.564–4	58.7–69.4	1029–1157	1828
R1234ze(E)	0–72	0–77.32	0.215–1.7	0–0.99	20–940	0.65–1.75	59–83.1	974–1240	2124
R1270	5–20	7–107	0.676–1.01	0–0.95	50–300	4–9.43	107–113	514–538	158
R134a	−7–70	−1.4–103	0.22–2.11	−0.1–1.07	1–3710	1.9–12.7	61.6–95.4	996–1319	3100
R141b	34–60	39–63	0.108–0.25	0–0.93	50–306	8.6–10.92	81–88.1	1162–1216	122
R152a	10–32	12–67	0.372–0.73	0.0–0.96	100–580	1.1284–2	95–104	881–936	251
R161	−5–8	−1–17	0.368–0.56	0–0.99	100–250	6.34	121.7–129	733–757	160
R22	−15.5–35	−14–287	0.29–1.354	−0.06–1	50–700	1.5–13.84	78.9–101.7	1150–1332	2104
R236fa	31	34–53	0.330780	−0.02–0.8	200–1200	1.03	71	1338	151
R245fa	18–130	0–204	0.116–2.34	−0.03–1	15–1500	0.636–1.75	55.4–90.2	938–1355	2392
R290	0–35	2–94	0.47–1.21	0–0.99	50–499	1.54–9.43	89.1–105.9	476–528.	731
R32	8–40	9–92	0.364–2.48	0–1	45–499	0.643–6	77.6–138.8	892–1195	3609
R600a	−20–41	−18–142	0.072–0.54	0–0.99	20–500	1–9.43	83.7–106.6	529–602	1460
R717	−25–10	−14–8	0.151–0.61	0–0.96	8–100	4	502–566	625–671	347
R744	−50–25	−44–28	0.687–6.43	0–1	76–720	0.81–11.46	80.7–168.7	710–1153	2387
								Total	22,608

Experimental parameters reported on the used database.

As shown in Figure 2.4-2, smooth tubes account for the largest number of data points among the tube geometries, exceeding 10,000. They are followed by microfin tubes, or internally grooved tubes, and flat multiport tubes, each of which includes several thousand data points. By contrast, the numbers of data points for plate heat exchanger geometries such as Oblique-Washboard and Zig-Zag are small. Considering these features, the dataset was judged sufficiently diverse and comprehensive to ensure model generalization.

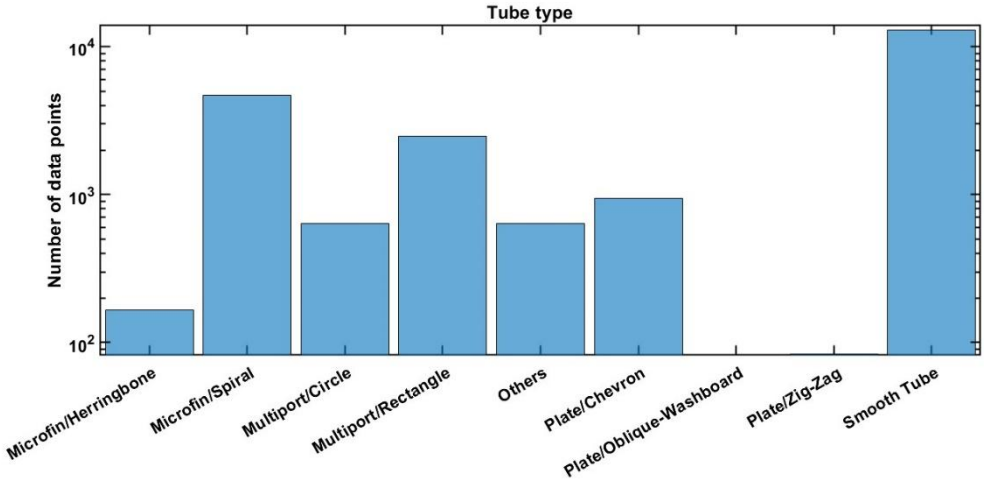

Figure 2.4-2 Number of data points considered for each tube type

2.4.4 Evaluation of machine learning

(1) Method for model evaluation and result analysis

Using the constructed dataset, model evaluation was performed by five-fold cross-validation ($K = 5$). In this method, the dataset was divided into five equal subsets; four subsets (80% of the total data) were used for training, and the remaining subset (20%) for testing and validation. This procedure was repeated five times, rotating the validation subset so that each was used once for validation, with all data contributing to both training and validation. This systematic approach enabled reliable evaluation of model prediction performance while suppressing overfitting.

After multiple machine learning models were trained and evaluated, the most accurate one was selected to construct the heat transfer coefficient prediction model. In this analysis, various input parameters, including both numerical and categorical variables, were considered, and relationships between experimental conditions and thermophysical properties were systematically extracted using machine learning. The resulting prediction model exhibited high

reproducibility consistent with the physical behavior of the experimental data.

(2) Evaluation of prediction performance

Root mean square error (RMSE) was adopted as the metric for evaluating each model's prediction performance. RMSE is the square root of the mean squared difference between predicted and measured values and is sensitive to large errors; accordingly, it is suitable for evaluating regression problems in thermal engineering. All analyses and model construction were performed using MATLAB 2024b.

Among the 27 evaluated models, the Bagged Trees model exhibited the best performance, with an RMSE of 1.9695. Gaussian Process Regression and Wide Neural Network also showed high performance, with RMSE values below 3. By contrast, the linear regression model and some tree-based models had RMSE values exceeding 4, indicating relatively large deviations from the experimental values. Detailed comparison results for each model are shown in Table 2.4-2.

Table 2.4-2 Evaluation results of the machine-learning models.

Trainig Model Preset	RMSE	MSE	RSquared	MAE	MAPE %
Bagged Trees	1.97	3.88	0.91	1.02	28.85
Fine Tree	2.20	4.86	0.88	1.07	28.35
Medium Tree	2.58	6.64	0.84	1.37	34.22
Exponential GPR	2.77	7.65	0.82	1.65	63.39
Rational Quadratic GPR	2.79	7.79	0.81	1.69	64.33
Matern 5/2 GPR	2.84	8.07	0.81	1.74	66.12
Wide Neural Network	2.87	8.21	0.80	1.86	75.15
Squared Exponential GPR	2.87	8.22	0.80	1.77	67.35
Trilayered Neural Network	3.10	9.62	0.77	2.14	77.29
Bilayered Neural Network	3.16	9.98	0.76	2.21	80.91
Coarse Tree	3.18	10.10	0.76	1.85	44.85
Fine Gaussian SVM	3.21	10.31	0.75	1.78	66.32
Least Squares Regression Kernel	3.23	10.44	0.75	2.11	76.95
Medium Neural Network	3.30	10.92	0.74	2.26	82.53
Narrow Neural Network	3.64	13.23	0.69	2.51	86.69
Boosted Trees	3.77	14.18	0.66	2.52	63.36
Cubic SVM	3.86	14.89	0.65	2.46	84.43
SVM Kernel	3.94	15.51	0.63	2.25	76.22
Medium Gaussian SVM	4.15	17.23	0.59	2.43	76.78
Quadratic SVM	4.28	18.33	0.56	2.58	85.87
Stepwise Linear	4.64	21.56	0.52	2.45	56.20
Coarse Gaussian SVM	5.05	25.53	0.39	3.09	98.68
Linear	5.12	26.21	0.41	3.40	86.95
Linear SVM	5.26	27.67	0.34	3.32	111.09
Robust Linear	5.56	30.94	0.31	3.29	69.42
Efficient Linear Least Squares	6.41	41.06	0.02	4.36	145.44
Efficient Linear SVM	6.62	43.77	-0.04	4.16	119.09
Interactions Linear	6.96	48.47	-0.08	2.37	53.53

Machine learning model type and performance.

(3) Result analysis of the bagged trees model

Figure 2.4-3 compares the experimental and predicted heat transfer coefficients for each refrigerant. The horizontal axis represents refrigerant type, and the vertical axis represents the heat transfer coefficient. For each refrigerant, the experimental and predicted values are shown using box-and-whisker plots. Overall, the predicted values agreed well with the experimental values for many refrigerants, confirming the high prediction accuracy of the model. For R11, in particular, the median and interquartile range were nearly identical, indicating that the model accurately reproduced the distribution characteristics of the data.

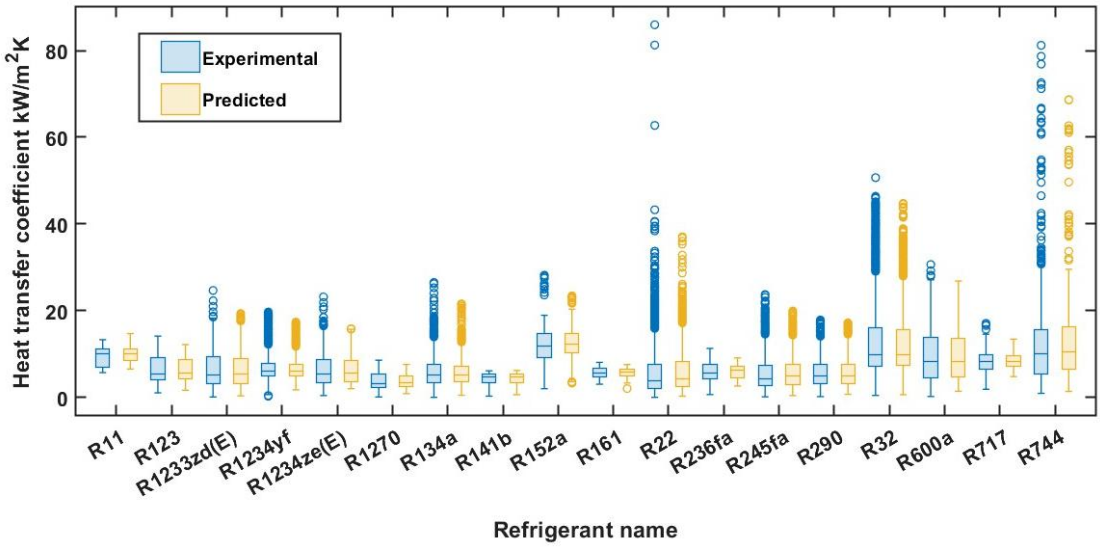

Figure 2.4-3 Comparison between the experimental and predicted heat transfer coefficients for each refrigerant

Figure 2.4-4 shows the residual analysis results. The residuals were distributed around zero for most data points, demonstrating the high stability and reliability of the model. However, residuals increased in the high heat transfer coefficient region. This is considered to be attributable to the limited number of data points under flow conditions near the superheated region and to the large scatter in values reported in the literature. Data in the range of 50–90 kW m^{-2} K^{-1} accounted for only approximately 0.11% of the total, indicating that errors in this region had a limited influence on the overall accuracy.

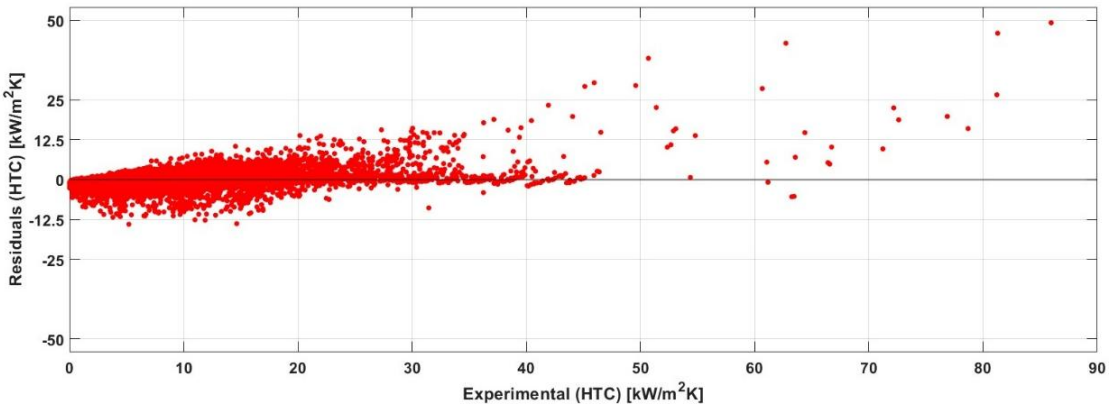

Figure 2.4-4 Experimental vs. residual heat transfer coefficient

Figure 2.4-5 shows the feature importance results based on SHAP (Shapley Additive Explanations) analysis. The horizontal axis indicates the mean absolute SHAP value for each input variable, with larger values indicating greater contributions to prediction. Refrigerant type was the most important factor, with the highest mean SHAP value of approximately 3.2. This reflects each refrigerant's differing thermophysical properties, which strongly affect phase-change heat transfer behavior. Tube geometry followed, with a SHAP value of approximately 1.9, identified as the second most important factor. This finding reflects the substantial influence of geometries such as microfin tubes and flat multiport tubes on boiling performance. Wall temperature and mass flux also made important contributions to prediction accuracy. In particular, wall temperature had a slightly greater influence as it is directly related to heat flux

and phase-change rate. Liquid-phase thermal conductivity and tube diameter had moderate influence; their SHAP values were around 1.0, confirming that they are important parameters although not dominant.

The next most influential factors were vapor quality, pressure, and saturation temperature, among which vapor quality had the greatest influence. Although these parameters are physically important, their influence may have been partly correlated with other dominant variables, and their variation ranges within the dataset were relatively small. Latent heat of vaporization was evaluated as the least influential variable, showing an extremely small SHAP value. This is because the variation range of latent heat of vaporization among the refrigerants considered was relatively limited, resulting in only a minor influence on the model output.

Notably, the combined influence of the other nine variables was comparable to that of liquid-phase thermal conductivity and tube diameter. This indicates that variables with small individual effects can still have a non-negligible influence when considered collectively, demonstrating the importance of comprehensive feature selection.

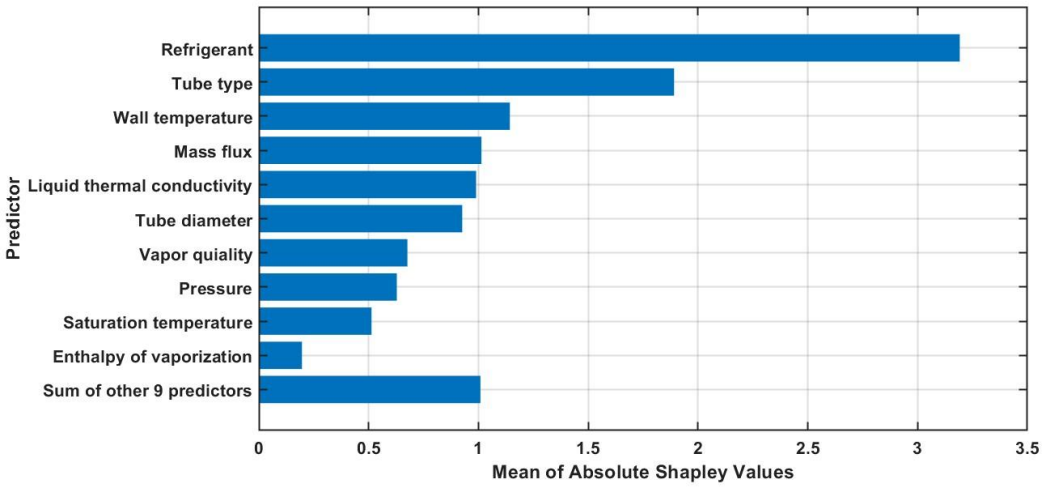

Figure 2.4-5 Mean absolute Shapley values corresponding to each input parameter

References (Section 2.1: Heat Exchangers)

Chang, Y.J., Wang, C.C., 1997, A generalized heat transfer correlation for louver fin geometry, *Int. J. Heat and Mass Trans.*, vol. 40, no. 3: p. 533-544.

Jige, D., Nobunaga, M., Inoue, N., 2023, Condensation heat transfer of binary and ternary mixtures inside multiport tubes, *Int. J. Heat and Mass Trans.*, vol. 207, no. 3: 123981.

Wang, C.C., Chi, K.Y., Chang, C.J., 2000, Heat transfer and friction characteristics of plain fin-and-tube heat exchangers, part II: Correlation, *Int. J. Heat and Mass Trans.*, vol. 43, no. 15: p. 2693-2700.

References (Section 2.2: Transport Properties)

Hoimontee, T.I., Morshed, M., Saber, M.T., Tuhin, A.R., Matsunaga, T., Dipankar, T., Miyara, A., 2026, Thermal Conductivity Measurement and Empirical Model of the Low-GWP Refrigerant R-1132(E), *Int. J. Thermophysics*, in press.

Huber, L.M., Laesecke, A., Perkins, A.R., 2003, Model for the Viscosity and Thermal Conductivity of Refrigerants, Including a New Correlation for the Viscosity of R134a, *Ind. Eng. Chem. Res.*, vol. 42.

Keishi Kariya, 2026, Transport Properties of the Next-Generation Refrigerants, J. HTSJ, Vol.65 No.270, pp.28-33.

Lemmon, E.W., Bell, I., Huber, M.L., McLinden, M.O., 2018, NIST Standard Reference Database 23: Reference Fluid Thermodynamic and Transport Properties-REFPROP, Version 10.0, National Institute of Standards and Technology.

Masumoto, T., Tuhin, A.R., Alam, M.J., Dipankar, T., Miyara, A., 2025, Viscosity Measurement of Low-GWP Refrigerant R474A Using the Tandem Capillary Method, *2025 JSRAE Annual Conference*, C234.

Miyara, A., Alam, M.J., Yamaguchi, K., Kariya, K., 2019, Development and Validation of Tandem Capillary Tubes Method to Measure Viscosity of Fluids, *Trans. of the JSRAE*, vol. 36, no. 1: p. 1-6.

Mondal, D., Hori, Y., Kariya, K., Miyara, A., 2020, Measurement of Viscosity of a Binary Mixture of R1123 + R32 Refrigerant by Tandem Capillary Tube Method, *Int. J. Thermophysics*, vol. 41, no. 6.

Morshed, M., Kariya, K., Miyara, A., 2024, Reporting of experimental viscosity data and modeling of transport properties of 1,1,1,3,3,3-hexafluoro-2-methoxypropane (HFE-356mmz) using extended corresponding states (ECS) and residual entropy scaling (RES) technique, *Int. J. Refrig.*, vol. 151.

Olchowy, G.A., Sengers, J.V., 1989, A simplified representation for the thermal conductivity of fluids in the critical region, *Int. J. Thermophys.*, vol. 10, no. 2: p. 417-426.

Rahman, M.O., Hoimontee, T.I., Dipankar, T., Saber, M.T., Alam, M.J., Miyara, A., 2025, Measurement of Thermal Conductivity of R-454C in Liquid Phase by Using the Transient Hot-Wire Method, *The 14th Asian Thermophysical Properties Conference (ATPC2025)*: p. 324-325.

Silvia, Morshed, M., Ogawa, R., Hoimontee, T.I., Alam, M.J., Miyara, A., 2025, Thermal Conductivity Measurement and Empirical Model of Low-GWP Refrigerant HFO1123, *Trans. of the JSRAE*, vol. 42, no. 3: p. 195-204.

Tran, D.X., Tuhin, A.R., Morshed, M., Hirata, R., Miyara, A., 2025**a**, Measurement and Empirical Model of Viscosity of the Novel Refrigerant R-1132(E), *Int. J. Thermophysics*, vol. 46: 65.

Tran, D.X., Tuhin, A.R., Morshed, M., Hirata, R., Miyara, A., 2025**b**, Measurement and Prediction Evaluation of Viscosity of Low GWP Mixtures R454B and R454C, *Trans. of the JSRAE*, vol. 42, no. 1: p. 21-30.

Tuhin, A.R., Morshed, M., Kariya, K., Miyara, A., 2024**a**, Experimental Investigation and Empirical Models of Viscosity of Trifluoroiodomethane (CF3I), *Int. J. Thermophysics*, vol. 45: 41.

Tuhin, A.R., Morshed, M., Kariya, K., Miyara, A., 2024**b**, Measurement and Empirical Models of Thermal Conductivity of Trifluoro-iodomethane (CF3I), *Int. J. Thermophysics*, vol. 45: 63.

References (Section 2.4: Machine Learning)

MathWorks, 2024, MATLAB, Version 24.1.0.2578822 (R2024a), The MathWorks Inc., Natick, MA, USA.

Refrigerant Evaporator and Condenser Database (RECDB). Available online: https://www.recdb.org/ (accessed 11 August 2025).

3. Basic Research on Suppression of Heat Transfer Degradation in Low-GWP Refrigerant Mixtures and Development of Heat Exchanger Application Technologies (Tokyo University of Marine Science and Technology)

3.1 Introduction

This project targets low-GWP refrigerant mixtures with global warming potentials (GWPs) of 150 or lower. Many of these refrigerants are zeotropic, and heat transfer deterioration caused by mass-transfer resistance during condensation and evaporation in heat exchangers remains a critical issue specific to refrigerant mixtures. The objective of this project is to elucidate the mechanisms of heat transfer deterioration in refrigerant mixtures and to establish technologies for suppressing it using surface-treated heat transfer surfaces and microchannel geometries, thereby supporting the development of heat exchangers compatible with low-GWP refrigerant mixtures. This section reports the results to date on the visualization of phase-change flow patterns of refrigerant mixtures in horizontal parallel microchannels simulating flat multiport tubes, evaluation of condensation and evaporation heat transfer coefficients, and verification of the effects of surface treatment and channel geometries on suppression of heat transfer deterioration. In addition, experimental data on evaporation and condensation heat transfer coefficients in flat multiport tubes have been provided to the heat transfer database described in Chapter 2, and future data will also be provided sequentially.

3.2 Experimental Apparatus and Data Reduction Method

3.2.1 Experimental apparatus

Figure 3.2-1 shows a schematic diagram of the experimental apparatus. The apparatus consists of a forced-circulation loop driven by a gear pump. The refrigerant delivered from the gear pump is heated to a prescribed quality in an electric preheater and then introduced into the test section. After condensing or evaporating in the test section, the refrigerant returns to the pump through the condenser and subcooler. The refrigerant flow rate is adjusted by the pump rotational speed and the opening of the flow control valve, while the refrigerant pressure is controlled primarily by the heat exchange rate in the condenser. In addition, the circulating refrigerant composition is measured by collecting a small amount of liquid refrigerant from a sampling port installed upstream of the flow meter and analyzing it by gas chromatography after expansion and vaporization.

Figure 3.2-2 shows a schematic diagram of the test section used in this experiment. The refrigerant flow channels consist of an aluminum alloy flow-channel plate machined with grooves simulating a flat multiport tube and a visualization window. The refrigerant is cooled or heated by a cooling/heating jacket or a sheet heater attached to the back side of the flow-channel plate. When the cooling/heating jacket is used, the heat flux is measured using a heat flux sensor inserted between the test section and the jacket. The effective heat transfer length is 100 mm, and the internal wall temperature is measured using K-type sheathed thermocouples inserted into the flow-channel plate. The refrigerant temperature is measured using K-type sheathed thermocouples inserted upstream and downstream of the test section, and the refrigerant pressure is measured at dedicated ports using an absolute pressure transducer and a differential pressure transducer.

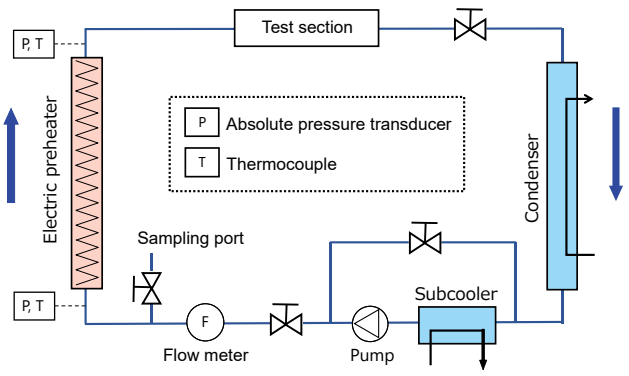

Figure 3.2-1 Schematic of the test loop

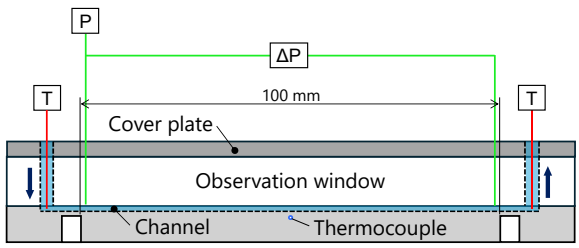

Figure 3.2-2 Schematic of test section

3.2.2 Data reduction method

The quality at the center of the test section was determined from the pressure and specific enthalpy at the center of the test section. The specific enthalpy at the center of the test section was calculated from the heat input in the test section and the refrigerant mass flow rate using the following equation.

$$h_{\mathrm{TS,center}} = h_{\mathrm{TS,in}} \pm \frac{Q_{\mathrm{TS}}}{2m} \tag{3.2-1}$$

where, Q_{TS} is the heat exchange rate in the test section, and m is the refrigerant mass flow rate. The refrigerant specific enthalpy at the test section inlet, $h_{\mathrm{TS,in}}$, was obtained from the following equation.

$$h_{\mathrm{TS,in}} = h_{\mathrm{EPH,in}} + \frac{Q_{\mathrm{EPH}}}{m} \tag{3.2-2}$$

where, $h_{\mathrm{EPH,in}}$ is the refrigerant specific enthalpy at the electric preheater inlet, and Q_{EPH} is the heat input in the electric preheater.

The condensation and evaporation heat transfer coefficient α was calculated using the following equation.

$$\alpha = \frac{q}{|T_{\mathrm{r}} - T_{\mathrm{w}}|} \tag{3.2-3}$$

where, q is the heat flux based on the actual heat transfer area, and T_{w} is the heat transfer surface temperature at the center of the test section, obtained by accounting for the one-dimensional heat conduction equation from the thermocouple insertion position to the heat transfer surface. T_{r} is the refrigerant temperature at the center of the test section, calculated from the refrigerant temperatures measured at the inlet and outlet of the test section.

3.3 Condensation and Evaporation Heat Transfer Characteristics of Low-GWP Refrigerant Mixtures

3.3.1 Evaluation of condensation heat transfer characteristics of the refrigerant mixture R474A

In zeotropic refrigerant mixtures, the high-boiling-point component preferentially condenses at the gas–liquid interface, resulting in an increased concentration of the low-boiling-point component on the vapor-phase side and a

concentration gradient. The refrigerant temperature on the vapor-phase side decreases from the bulk region toward the gas–liquid interface, thereby reducing the effective temperature difference for heat transfer. Consequently, the condensation heat transfer coefficient of zeotropic refrigerant mixtures is known to be lower than that of pure refrigerants. In this study, R474A—a refrigerant mixture containing R1132(E), a prospective next-generation refrigerant—was used as the test refrigerant, and the condensation heat transfer coefficient was evaluated in parallel microchannels with 1.0 mm × 1.0 mm square channels.

Figure 3.3-1 shows the condensation heat transfer coefficient of the refrigerant mixture R474A (R1132(E)/R1234yf = 23/77 mass%) in parallel microchannels with a hydraulic diameter of 1.0 mm (Nishizaki *et al*., 2025). For comparison, the heat transfer coefficient of the pure refrigerant R1234yf, measured using the same test section, is also shown. Under all mass velocity conditions, the heat transfer coefficients of both R474A and R1234yf decreased with decreasing quality. This decrease is attributable to the increasing condensate liquid-film thickness at lower quality, which raises the thermal resistance of the liquid film. At a mass velocity of 100 kg m^{-2} s^{-1}, the heat transfer coefficient of R474A was approximately 30–40% lower than that of R1234yf. This is considered to result from stronger heat transfer deterioration caused by mass-diffusion resistance under low mass velocity conditions, where channel flow velocity is small. By contrast, at a mass velocity of 400 kg m^{-2} s^{-1}, the heat transfer coefficients of R474A and R1234yf were comparable over the entire quality range, indicating that the influence of heat transfer deterioration was smaller than under low mass velocity conditions. At this mass velocity, annular flow was observed in $1\text{-}x < 0.8$ (Nogami *et al*., 2025), confirming that, under high mass velocity conditions where flow agitation is substantial, the effect of heat transfer deterioration caused by mass-diffusion resistance is reduced.

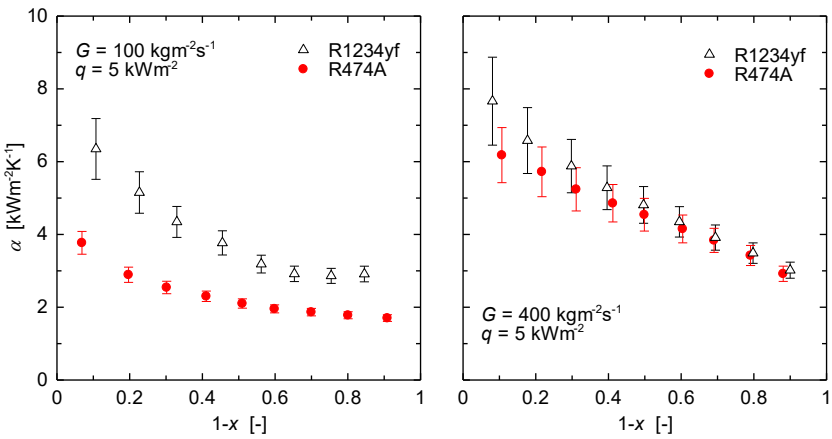

Figure 3.3-1 Condensation heat transfer coefficients of R474A and R1234yf in the multiport channels with hydraulic diameter of 1.0 mm (T_r = 40 °C, q = 5 kW m^{-2})

3.3.2 Evaluation of evaporation heat transfer characteristics of the refrigerant mixture R474A

Figure 3.3-2 shows the evaporation heat transfer coefficient of the refrigerant mixture R474A in parallel microchannels with a hydraulic diameter of 1.0 mm as a function of quality x (Numata *et al*., 2025a). For comparison, the heat transfer coefficient of the pure refrigerant R1234yf, measured using the same test section, is also shown. The heat transfer coefficient of R474A was approximately 15–50% lower than that of R1234yf at all mass velocities, and the difference was particularly pronounced under low mass velocity conditions. This is because, in microchannels where surface tension effects are considerable, a thin, largely undisturbed liquid film forms under low mass velocity conditions, and heat transfer deterioration owing to mass diffusion resistance becomes pronounced as heat transfers through this film. Under high mass velocity conditions, annular flow and churn flow with strong gas–liquid interfacial disturbance are observed even in microchannels, as in conventional-diameter tubes. Under low mass velocity conditions, however, flow patterns characteristic of microchannels, such as plug flow and slug–annular flow, appear. For pure

refrigerants, the thin liquid film with little disturbance formed in plug flow and slug–annular flow has low thermal resistance, resulting in a high heat transfer coefficient. For refrigerant mixtures, however, heat transfer deterioration owing to mass diffusion resistance has been reported to become pronounced (Jige *et al*., 2023). A similar tendency was observed in this experiment, confirming that heat transfer deterioration in zeotropic refrigerant mixtures becomes significant under low mass velocity conditions. In addition, compared with the condensation flow shown in Figure 3.3-1, the reduction in heat transfer coefficient was more pronounced during evaporation, demonstrating the greater importance of suppressing heat transfer deterioration in evaporation flow.

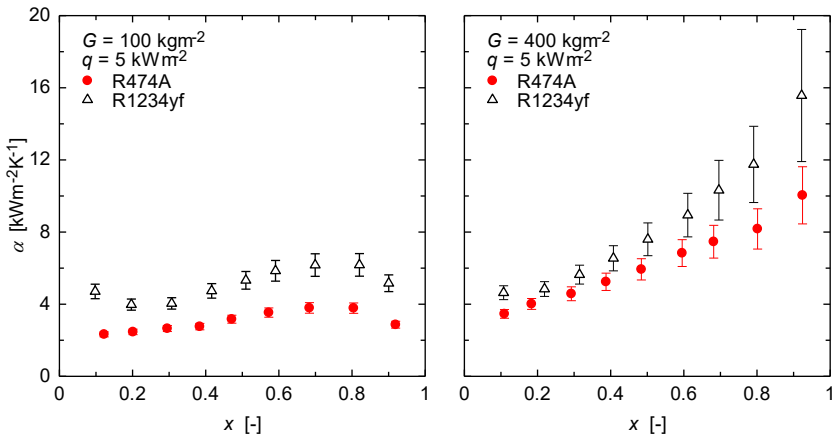

Figure 3.3-2 Evaporation heat transfer coefficients of R474A and R1234yf in the multiport channels with hydraulic diameter of 1.0 mm (T_r = 15 °C, q = 5 kW m^{-2})

3.4 Evaluation of Heat Transfer Enhancement by Surface Characteristics and Flow-Channel Geometry

3.4.1 Heat transfer enhancement by surface characteristics

As evaporation heat transfer in zeotropic refrigerant mixtures in parallel microchannels deteriorates relative to that of pure refrigerants owing to the effects of mass diffusion resistance, developing technologies for boiling enhancement and suppressing heat transfer deterioration in parallel microchannels is important. Many studies have focused on heat transfer surface characteristics as a means of enhancing nucleate boiling heat transfer; however, knowledge remains limited, particularly regarding the influence of surface characteristics on the heat transfer behavior of refrigerant mixtures in microchannels. In this study, a porous layer was formed in parallel microchannels machined into an aluminum alloy flow-channel plate, and the heat transfer coefficient on the surface-treated, namely anodized, surface was measured to evaluate the surface treatment's heat transfer enhancement effect. Details of the anodizing treatment are described in Chapter 4.

Figure 3.4-1 shows the heat transfer coefficient of the refrigerant mixture R454C on the treated surface as a function of heat flux q. For comparison, the heat transfer coefficients of the pure refrigerant R1234yf and of R454C on a smooth surface are also shown. For all heat transfer surfaces and refrigerants, the heat transfer coefficients rose with increasing heat flux owing to enhanced nucleate boiling heat transfer. At a heat flux of 10 kW m^{-2}, the heat transfer coefficient on the treated surface was comparable to that on the smooth surface, indicating that the surface treatment's enhancement effect was limited. Under higher heat-flux conditions, however, the heat transfer coefficient of R454C on the treated surface was approximately 15% higher than that on the smooth surface. Compared with the pure refrigerant R1234yf, the heat transfer coefficient of R454C on the treated surface was lower under low heat-flux conditions, whereas under relatively high heat-flux conditions it exceeded that of R1234yf.

Because the heat transfer experiments confirmed the boiling enhancement effect of the surface treatment, boiling behavior was observed using a high-speed camera. Figure 3.4-2 shows visualization results for the boiling behavior of R454C on the smooth and treated surfaces under conditions of a mass velocity of 100 kg m^{-2} s^{-1}, a quality of 0.2, and a heat flux of 30 kW m^{-2}. On both heat transfer surfaces, bubbles formed in the thick liquid film at the corners of the square channels. Compared with the smooth surface, the treated surface produced finer and more numerous bubbles. This is considered to be because the porous layer formed by surface treatment acted as effective boiling cavities and promoted bubble nucleation. These results confirmed that, under relatively high heat-flux conditions, the porous layer on the heat transfer surface effectively enhances boiling heat transfer of refrigerant mixtures in parallel microchannels.

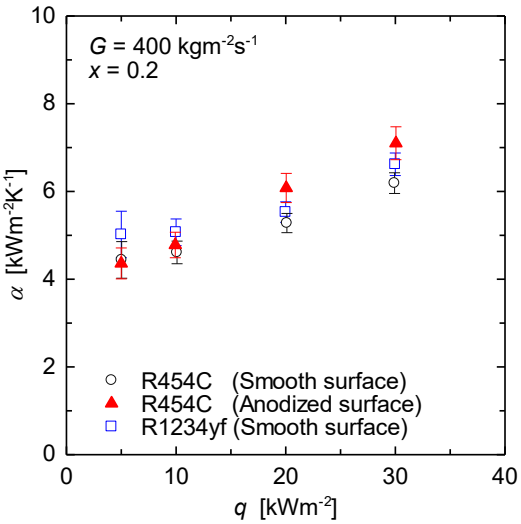

Figure 3.4-1 Effect of surface treatment on boiling heat transfer coefficients in the multiple channels with hydraulic diameter of 1.0 mm (T_r = 15 °C, G = 400 kg m^{-2} s^{-1}, x = 0.2)

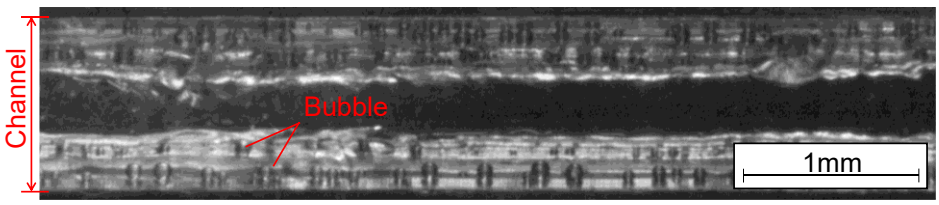

(a) Smooth surface

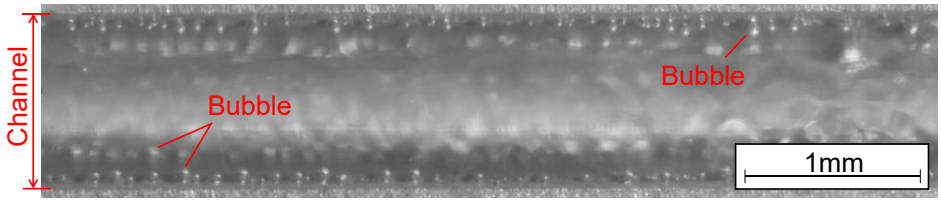

(b) Treated surface

Figure 3.4-2 Boiling behaviors of R454C in the multiple channels with smooth and treated surfaces (T_r = 15 °C, G = 100 kg m^{-2} s^{-1}, x = 0.2, q = 30 kW m^{-2})

3.4.2 Heat transfer enhancement by flow-channel geometry

As the influence of heat transfer deterioration is pronounced under low mass velocity conditions for zeotropic refrigerant mixtures, suppressing such deterioration and enhancing heat transfer under these conditions are important. In this study, the heat transfer enhancement effect of flow-channel geometry for refrigerant mixtures was evaluated to promote heat transfer through flow agitation. First, the evaporation heat transfer coefficient of the refrigerant mixture

R454C was evaluated in channels in which fins were interrupted in the flow direction, with a fin length of 8 mm, fin spacing of 2 mm, and fin pitch of 10 mm (Numata *et al*., 2025b). Under a mass velocity of 400 kg m^{-2} s^{-1}, a heat transfer enhancement effect of approximately 1.35 times was observed owing to flow agitation; however, the effect was limited under low mass velocity conditions. Accordingly, channels with numerous inclined microfins, hereafter referred to as microfin channels, were fabricated to further promote flow agitation and disrupt the boundary layer, and their effects on suppressing heat transfer deterioration and enhancing heat transfer were evaluated.

Figure 3.4-3 shows the evaporation heat transfer coefficient of the refrigerant mixture R474A in the microfin channels (Numata *et al.*, 2026). For comparison, the heat transfer coefficient of R474A in parallel microchannels with a hydraulic diameter of 1.0 mm is also shown. Even under a low mass velocity condition of 50 kg m^{-2} s^{-1}, the heat transfer coefficient in the microfin channels was approximately 1.3–2.7 times higher than that in the parallel microchannels, confirming a substantial enhancement effect precisely where heat transfer deterioration is most pronounced. This is considered to be because flow agitation by the microfins not only enhanced convective heat transfer but also disrupted the concentration boundary layer caused by mass-diffusion resistance, thereby suppressing heat transfer deterioration. In addition, compared with the parallel microchannels, the microfin channels suppressed dryout up to higher quality. This is considered to be attributable to enhanced rewetting caused by the inflow and outflow of gas and liquid between adjacent channels. To verify these enhancement and suppression effects, the flow patterns and liquid film structures were visualized (Numata *et al*., 2025a). Figure 3.4-4 shows the observed flow patterns at a mass velocity of 50 kg m^{-2} s^{-1} and qualities of 0.2 and 0.8. Under low-quality conditions, vapor plugs observed in the parallel microchannels were segmented by the microfins, and the flow proceeded, deflected along the microfins' incline in the channel-width direction. In addition, a relatively thick liquid film formed around the microfins, within which boiling bubbles were observed. Under high-quality conditions, the liquid film around the microfins was thinner than under low-quality conditions, and strong disturbance at the gas–liquid interface was also observed. These results confirmed that flow agitation promoted by microfins effectively enhances heat transfer and suppresses heat transfer deterioration in zeotropic refrigerant mixtures. However, pressure loss also increased compared with the parallel microchannels as heat transfer was enhanced; accordingly, a comprehensive evaluation of both heat transfer enhancement and the accompanying increase in pressure loss will be conducted in future work.

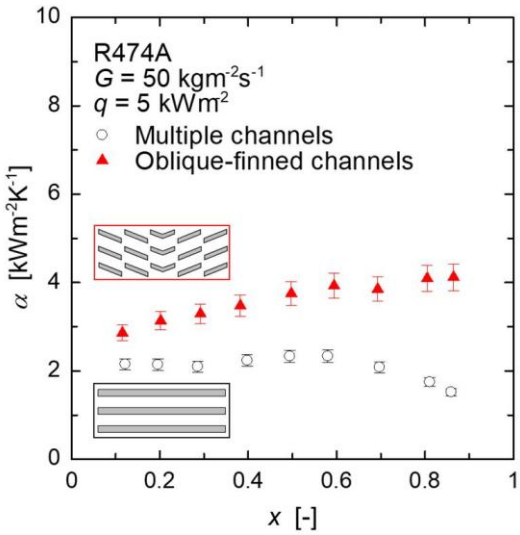

Figure 3.4-3 Evaporation heat transfer coefficients of R474A in the multiple and oblique-finned channels (T_r = 15 °C, G = 50 kg m^{-2} s^{-1}, q = 5 kW m^{-2})

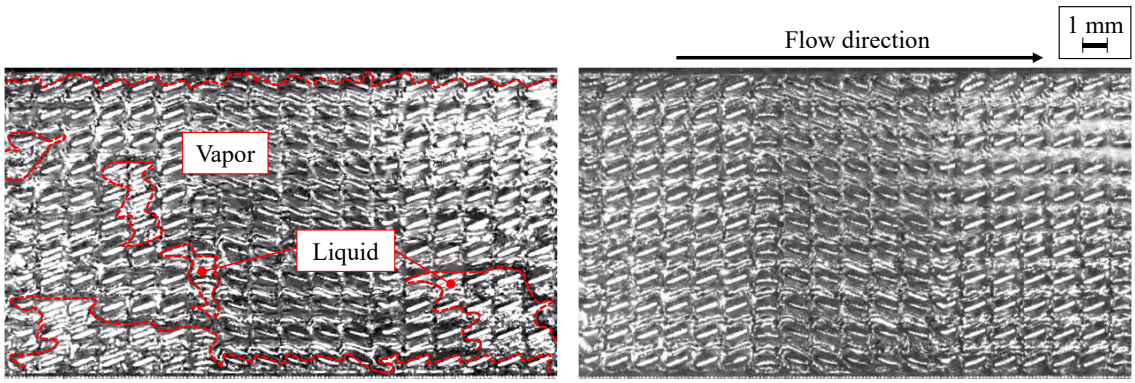

(a) $x = 0.2$ (b) $x = 0.8$

Figure 3.4-4 Flow characteristics of R474A in the oblique-finned channels
($T_r = 15$ °C, $G = 50$ kg m^{-2} s^{-1}, $q = 5$ kW m^{-2})

3.5 Conclusions

In this project, flow patterns and liquid-film structures of zeotropic refrigerant mixtures in horizontal parallel microchannels simulating flat multiport tubes were visualized, and condensation and evaporation heat transfer coefficients were evaluated, to develop technologies for suppressing heat transfer deterioration caused by mass-diffusion resistance and enhancing heat transfer through surface treatment and fine flow-channel structures. In addition, the effects of heat transfer surface treatment and flow-channel geometry on enhancing heat transfer and suppressing heat transfer deterioration were investigated. The results confirmed that, even in parallel microchannels, heat transfer enhancement can be achieved by forming a porous layer under relatively high heat-flux conditions. It was also confirmed that, even under low mass velocity conditions, flow agitation induced by microfins is effective for suppressing heat transfer deterioration and enhancing heat transfer in zeotropic refrigerant mixtures. In this project, the R454 series and R474A were evaluated as test refrigerants from the viewpoint of availability. In future work, evaluations will also be conducted for low-GWP refrigerant mixtures containing other candidate refrigerants, to develop elemental technologies for suppressing heat transfer deterioration and enhancing heat transfer in heat exchangers.

References (Section 3)

Jige, D., Nobunaga, M., Nogami, T., Inoue, N., 2023, Boiling heat transfer of binary and ternary mixtures in multiple rectangular microchannels, *Appl. Therm. Eng.*, vol. 229: 120613. https://doi.org/10.1016/j.applthermaleng.2023.120613

Nishizaki, A., Numata, N., Jige, D., Inoue, N., 2025, Experiment on Condensation Heat Transfer Characteristics of R474A in Parallel Minichannels, *2025 JSRAE Annual Conference*: B313.

Nogami, T., Jige, D., Inoue, N., 2025, Flow regimes of R32, R1234yf, and R454C in horizontal multiport mini/micro-channels: Development of a new flow regime prediction method, *International Journal of Refrigeration*, vol. 179: p. 226-237. https://doi.org/10.1016/j.ijrefrig.2025.08.015

Numata, N., Nishizaki, A., Nogami, T., Jige, D., Inoue, N., 2024, Experiment on Boiling Heat Transfer Characteristics of R454C in Electric Discharge Machined Parallel Microchannels, *2024 JSRAE Annual Conference*: A331.

Numata, N., Nishizaki, A., Jige, D., Inoue, N., 2025a, Experimental Examination of Suppression of Heat Transfer Deterioration by Zeotropic Refrigerant Mixture by Micro Fin, *2025 JSRAE Annual Conference*: B322.

Numata, N., Nishizaki, A., Jige, D., Inoue, N., 2025b, Experimental study on boiling heat transfer and flow regime of R454C in parallel staggered-finned minichannels, *7th IIR Conference on Thermophysical Properties and Transfer Processes of Refrigerants*, Maryland, USA: 1140.

Numata, N., Nishizaki, A., Jige, D., Inoue, N., 2026, An experimental investigation on boiling heat transfer of R474A in oblique-finned minichannels, *12th International Conference on Boiling and Condensation Heat Transfer*, Massachusetts, USA.

4. Research and Development on Improving the Evaporation and Condensation Performance of Refrigerant Mixtures by Controlling the Surface Structure of Aluminum and Applying the Technology to Heat Transfer Tubes (UACJ)

4.1 Application of Refrigerant Mixtures to Heat Exchangers

4.1.1 Aluminum multiport tubes used in heat exchangers

Aluminum multiport tubes were first used in automotive air-conditioning heat exchangers, where space saving and weight reduction are required. Since the 2010s, their application to stationary air-conditioning systems as microchannel heat exchangers has expanded. Conventional heat exchangers for stationary air-conditioning systems have mainly used circular internally grooved copper tubes. However, driven by growing demands for energy conservation and higher performance, multiport tubes have seen increasing application because their flat geometry reduces air-side flow resistance and increases the internal heat transfer area. Aluminum multiport tubes are generally manufactured by extrusion and typically comprise approximately 10–20 fine channels with hydraulic diameters of approximately 0.5–1 mm arranged in parallel.

In heat transfer inside flat multiport tubes, surface tension effects in gas–liquid two-phase flow in microchannels enhance heat transfer. During filmwise condensation and liquid-film evaporation in triangular or rectangular channels, surface tension draws liquid into the channel corners and forms thin liquid films along the channel sides, thereby improving the heat transfer coefficient compared with that of circular channels (*e.g.*, Miyara, 2015).

4.1.2 Issues and countermeasures for heat transfer tubes in the application of refrigerant mixtures

In response to the Kigali Amendment to the Montreal Protocol, Japan is advancing the phasedown of hydrofluorocarbon (HFC) refrigerants, and reducing the HFC charge in heat exchangers has become an urgent issue. Furthermore, to reduce greenhouse gas (GHG) emissions toward carbon neutrality by 2050, low-GWP refrigerant mixtures are regarded as a promising option for stationary air-conditioning equipment. However, zeotropic refrigerant mixtures, which are considered promising candidates, suffer from reduced in-tube heat transfer performance compared with single-component refrigerants. In multiport tubes and heat exchangers, the flow distribution of the gas and liquid phases tends to become nonuniform owing to gravity and surface tension. The resulting component separation causes nonuniform liquid-film formation and reduces heat transfer efficiency. In addition, during refrigerant evaporation, the low-boiling-point component preferentially evaporates, causing the high-boiling-point component to become concentrated near the liquid-film surface, and the heat transfer coefficient decreases below the weighted average for the corresponding single-component refrigerants. Accordingly, conventional multiport tube structures must be improved to counter this mixture-specific performance loss.

4.1.3 Improvement of refrigerant boiling characteristics by surface treatment of aluminum

In refrigerant boiling heat exchange, which utilizes gas–liquid phase change, the interface design between the heat transfer surface and the refrigerant critically determines heat transfer performance. For example, in boiling heat transfer using refrigerants with low surface tension and high wettability, such as hydrofluoroethers, bubble nuclei for boiling incipience are difficult to form, resulting in a higher superheat required for the onset of boiling (Shen *et al*., 2021). Such a delay in boiling incipience is particularly pronounced on smooth mirror-like surfaces. However, previous studies have shown that boiling and heat transfer can be enhanced by forming appropriate fine surface roughness, for example as reported by Jabardo *et al*. (2009), or by forming regions with different wettability on the surface (Hamazaki *et al*.,

2018), owing to differences in surface characteristics.

Aluminum is a metallic material whose surface characteristics can be modified by various methods, including mechanical treatments such as polishing and blasting, coatings such as painting, chemical treatments such as chemical conversion treatment and chemical polishing, and electrochemical treatments such as anodizing and plating. When aluminum is polarized as the anode in an appropriate aqueous electrolyte solution, an oxide film is formed on the aluminum surface according to Equation (4.1-1).

$$2Al + 3H_2O \rightarrow Al_2O_3 + 6H^+ + 6e^- \quad (4.1\text{-}1)$$

Many studies have reported that the nanostructure of oxide films formed on aluminum surfaces strongly depends on the anodizing conditions (*e.g.*, Kikuchi *et al.*, 2015). As representative nanostructures, a thin and dense barrier-type oxide film is formed when aluminum is anodized in a neutral solution, whereas a porous-type oxide film is formed in an appropriate acidic solution. Even for porous-type oxide films, the nanostructure strongly depends on the electrolyte species and electrolysis conditions, and the nanopore size in the oxide can be controlled from several tens to several hundred nanometers. Figure 4.1-1 shows a surface SEM image of a porous-type oxide film formed on an aluminum surface by anodizing in phosphoric acid. Numerous fine pores with diameters of approximately 100 nm were formed in the oxide. On surfaces with such porous structures, nucleation sites for bubble formation during boiling increase, producing a marked improvement in the heat transfer coefficient when used as boiling surfaces (Shen *et al.*, 2021). However, heating after long-term refrigerant immersion produced a large delay in boiling incipience, with the incipience temperature increasing by more than 40 K at maximum. This increase was considered to occur because microscopic bubbles serving as boiling nuclei trapped in the surface microstructure disappeared as the refrigerant gradually penetrated the structure over time, requiring a large degree of superheat for bubble-nucleus formation. Based on these findings, Nakajima *et al*. (2025) investigated the effects of oxide nanostructures formed on aluminum surfaces on boiling heat transfer enhancement in the NEDO Energy and Environmental New Technology Leading Research Program, "Development of Heat and Mass Transfer Enhancement Process Technologies by Phase Interface Control," conducted from FY2021 to FY2022. Using a hydrofluoroether as the refrigerant, they reproduced the delay in boiling incipience after long-term immersion, as reported in previous studies, when a porous structure was formed on the heat transfer surface by anodizing. They also clarified that the delay in boiling incipience can be suppressed by controlling the surface nanostructure through anodizing conditions. Thus, because heat transfer surface microstructure strongly affects refrigerant boiling characteristics and heat transfer efficiency, this project verified the effect of surface structure on refrigerant-mixture boiling on heat transfer tube surfaces.

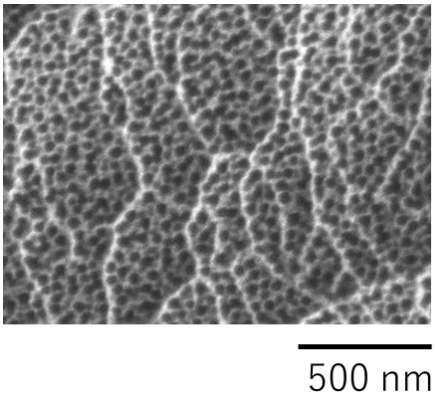

Figure 4.1-1 SEM image of anodic porous oxide fabricated by anodizing

4.1.4 Objectives of this project

The project "Development of High-Efficiency Refrigeration and Air-Conditioning Technologies toward the Practical Application of Next-Generation Low-GWP Refrigerants / Development and Evaluation of Low-GWP Refrigerant Mixtures Suitable for Residential Air Conditioning and Other Applications / Evaluation of Thermophysical Properties, Safety, and Environmental Impact of Low-GWP Refrigerant Mixtures, Development of Elemental Technologies for Compatible Equipment, and System Performance Evaluation / Development of Elemental Technologies Compatible with Refrigerant Mixtures" was launched in FY2023. Our company joined the project in FY2024 and has been verifying elemental technologies for improving heat transfer characteristics using aluminum multiport tubes. In this project, the effects of heat exchanger surface microstructures on the evaporation and condensation of low-GWP refrigerant mixtures are investigated, elemental technologies for maximizing heat exchange performance are developed, and issues associated with applying these functions to heat transfer tubes are identified. In addition, research and development toward practical application address aluminum geometry, processing methods, and material properties. To control the surface structure of aluminum, fine porous structures are being formed on aluminum surfaces that serve as refrigerant flow channels, for example, using anodizing technology as shown in Figure 4.1-2. Furthermore, aluminum geometries, processing methods, and material properties that allow these functions to exert their effects optimally are examined, and practical examples contributing to performance improvement are identified.

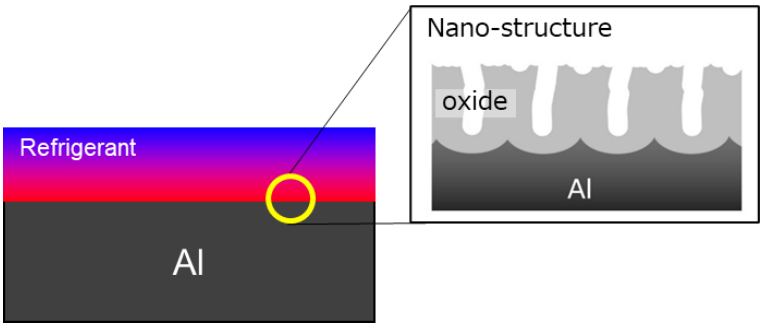

Figure 4.1-2 Schematic illustration of heat transfer surface with nano-structure

Only limited reports are available on surface treatment of long, closed surfaces such as the internal flow channels of multiport tubes, and the treatment behavior is expected to differ from that for bulk materials. Accordingly, in this project, the effects of various surface structures on refrigerant heat transfer characteristics are evaluated together with their applicability to multiport tubes. As an interim target for FY2025, the project aimed to verify the effects of surface microstructures on the boiling characteristics of refrigerant mixtures and to test whether surface structure formation methods can be applied to materials with poor treatability, such as the inner walls of flow channels in multiport tubes. In parallel, heat transfer enhancement through the cross-sectional geometry of multiport tubes was examined, and desirable configurations for suppressing heat transfer deterioration were investigated from the perspectives of the microstructure of the flow-channel surface and flow-channel geometry of multiport tubes.

In FY2027, the final year of this project, the objective is to optimize the flow-channel structure based on the heat transfer deterioration mechanisms of candidate refrigerants using evaluation results obtained from FY2026 for heat exchangers incorporating deterioration-suppression technologies, and to fabricate prototype heat exchangers equipped with surface-treated heat transfer tubes that suppress heat transfer deterioration.

4.2 Approaches for Improving Heat Transfer Characteristics

4.2.1 Improvement of heat transfer performance by forming porous structures on aluminum surfaces

In this study, constant-current anodizing was used to form oxide films on aluminum surfaces. Figure 4.2-1 shows the voltage–time curves measured during constant-current anodizing in prescribed aqueous electrolyte solutions. At an electrolyte concentration of 0.7 M, the voltage–time curve exhibited typical behavior: the voltage initially increased linearly, reached a peak, and then approached a steady value, indicating stable oxide film formation on the aluminum surface. By contrast, when the electrolyte was diluted, the voltage fluctuated unstably, suggesting that the oxide film was not formed uniformly on the aluminum surface. Therefore, an electrolyte concentration of 0.7 M was adopted as the standard condition for subsequent tests.

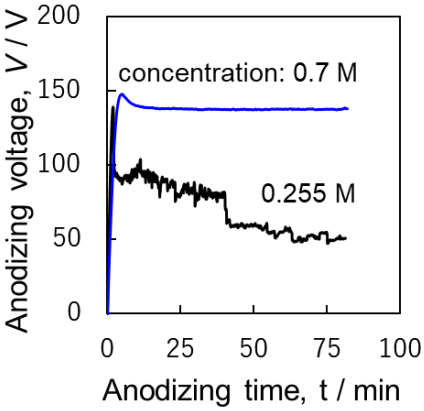

Figure 4.2-1 Changes in the anodizing voltage with time during constant current anodizing

Figure 4.2-2 shows scanning electron microscope (SEM) images of the porous oxide film formed on the aluminum surface by anodizing (Figure 4.2-2(a)). To enlarge the pore size of the porous oxide film, the specimens were immersed in acid for prescribed periods after anodizing to chemically dissolve the oxide, as shown in Figure 4.2-2(b) and (c). The anodizing treatment formed an oxide film with numerous pores on the aluminum surface, clearly indicating that a porous surface was produced. In addition, the pore size gradually increased with increasing acid immersion time, t_p, demonstrating that a porous-type oxide film with larger pore diameters was formed by chemical dissolution of the oxide.

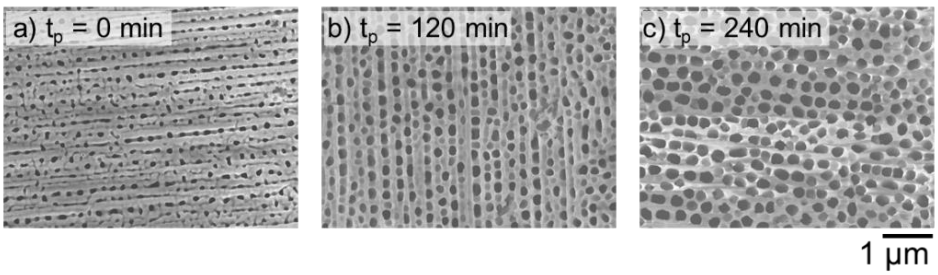

Figure 4.2-2 SEM images of the surface of the anodized specimens after pore widening treatment for (a) 0 min to (c) 240 min

To observe the formed oxide film in detail, the specimen shown in Figure 4.2-2(a) was embedded in resin, mechanically polished to expose its cross section, and observed by SEM; the results are shown in Figure 4.2-3. Cross-sectional observation revealed that the oxide film formed by anodizing on the aluminum surface had a thickness of approximately 700 nm and a pore diameter of approximately 70 nm. Forming such porous oxides with surface

nanostructures on the heat transfer surface and evaluating their heat transfer characteristics verified the effect of surface structure on refrigerant boiling. As an initial step, these treatments were applied to specimens with parallel channels simulating the flow channels of multiport tubes; the specimens were sealed on one side with a visualization window. This configuration enabled comparison of boiling behavior and heat transfer characteristics relative to untreated channels. When R454C was supplied as the refrigerant and a heat flux of approximately 30 kW m^{-2} was applied, the measured heat transfer coefficient was approximately 13% higher than that of the untreated channel, confirming the heat transfer enhancement effect of the surface treatment. In addition, the heat transfer coefficient under these conditions was approximately 8% higher than that obtained when R1234yf was used on the untreated surface, demonstrating the effectiveness of surface treatment for heat transfer enhancement. Based on observations of boiling behavior, this improvement in heat transfer coefficient was attributed to the increase in nucleation sites for nucleate boiling caused by the surface structure, which promoted the generation of fine bubbles and enhanced heat exchange as the bubbles detached.

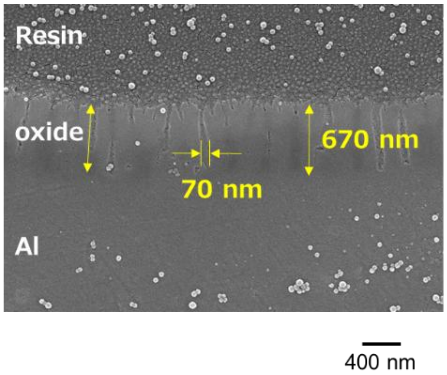

Figure 4.2-3 Cross-sectional images of anodic oxide formed by anodizing

4.2.2 Verification toward anodizing treatment of the inner walls of multiport tubes

(1) Attempt to form oxide films by direct electrolysis of multiport tubes

The investigation described in Section 4.2.1 showed that forming fine structures on refrigerant flow-channel surfaces can increase the heat transfer coefficient. Therefore, experiments verified whether anodizing could form porous structures on the inner walls of actual multiport tube flow channels. Prior to this investigation, treatment of multiport tube materials was attempted at the beaker scale. In the preliminary test, a multiport tube with a 0.5 mm square flow-channel cross section was cut to a length of approximately 4 cm, immersed in an electrolyte solution in a beaker, and anodized. Cross sections at the positions shown in Figure 4.2-4 were then observed by SEM. Observation point a was the outer surface of the multiport tube facing the counter electrode, observation point b was the inner wall of the multiport tube, and observation point c was the outer surface on the side opposite the counter electrode.

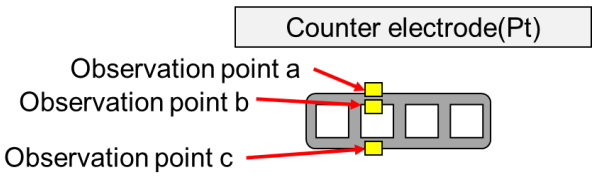

Figure 4.2-4 Observation point of anodized multi-hole tube

Figure 4.2-5 shows cross-sectional SEM images of oxide films formed on the aluminum multiport tube surface at each observation point by constant-current anodizing at a current density of 1 mA cm^{-2}. The observation points were

located approximately 1 cm from the tube end. The oxide films formed on the outer surfaces of the multiport tube, shown in Figure 4.2-5(a) and (c), had nearly uniform thickness regardless of whether the surface faced the counter electrode. By contrast, as shown in Figure 4.2-5(b), the oxide film on the inner wall was thinner than that on the outer surface, indicating that the flow channel's inner wall has lower treatability than the outer surface. Figure 4.2-6 shows cross-sectional SEM images of specimens obtained when the same electrolysis treatment was performed with the current density changed to 3 mA cm^{-2}. As the electric charge increased with current density, the oxide films formed at all observation points were thicker than those in Figure 4.2-5. The ratio of the oxide film thickness on the outer surface of the multiport tube to that on the inner wall of the flow channel was 1.67 for the specimen anodized at 1 mA cm^{-2} and 1.73 for the specimen anodized at 3 mA cm^{-2}. Thus, as the current density during anodizing increases, the difference in oxide film thickness between the inner wall of the flow channel and the outer surface of the multiport tube tends to increase. This is considered to be because, inside a flow channel with a narrow inlet such as that of a multiport tube, ion diffusion in the aqueous solution is limited and charge transfer by ions becomes rate-limiting, thereby reducing the throwing power of oxide film formation.

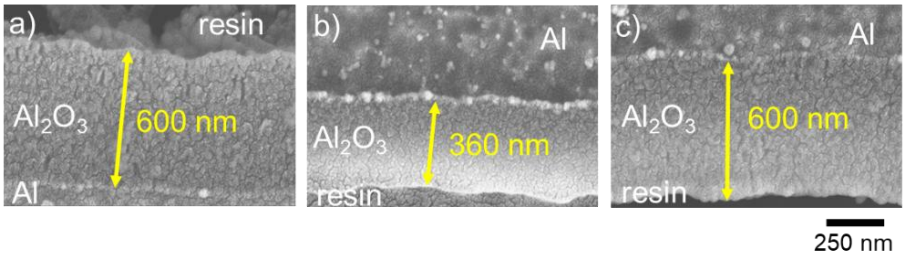

Figure 4.2-5 Cross-sectional SEM images of an oxide film formed on the surface of a multi-hole tube fabricated by constant current anodizing at 1 mA cm^{-2}

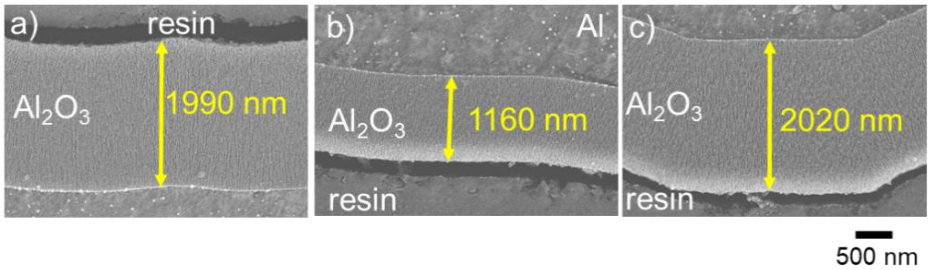

Figure 4.2-6 Cross-sectional SEM images of an oxide film formed on the surface of a multi-hole tube fabricated by constant current anodizing at 3 mA cm^{-2}

The above investigation showed that oxide films are formed preferentially on the outer surface of multiport tubes and that this tendency becomes more pronounced as the applied current density increases. Therefore, to suppress oxide film formation on the outer surface, anodizing of long multiport tubes was attempted after masking the outer surface. Figure 4.2-7 shows photographs of a long tube, approximately 40 cm in length, before and after electrolysis treatment. During electrolysis, as shown in Figure 4.2-7(a), the outer surface was protected with PVC film masking tape to prevent reaction there. After electrolysis, however, as shown in Figure 4.2-7(b), the reaction was concentrated at the tube end, and part of the specimen had dissolved. Visual observation clearly indicated that a uniform oxide film had not been formed.

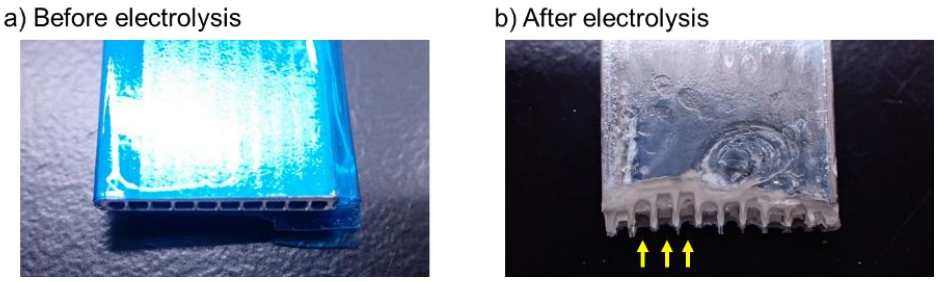

Figure 4.2-7 Appearance of the edge of a multi-hole tube (40 cm in length) before and after anodizing

Figure 4.2-8 shows cross-sectional SEM images of the inner wall of the multiport tube shown in Figure 4.2-7(b), sampled at approximately 1 cm and 5 cm from the tube end. On the inner wall surface of the flow channel, oxide film formation by anodizing was observed 1 cm from the end but not at the deeper 5 cm position. This is considered to be because, as was also evident from visual observation, current concentrated only near the flow channel's inlet, preventing uniform oxidation of the inner wall.

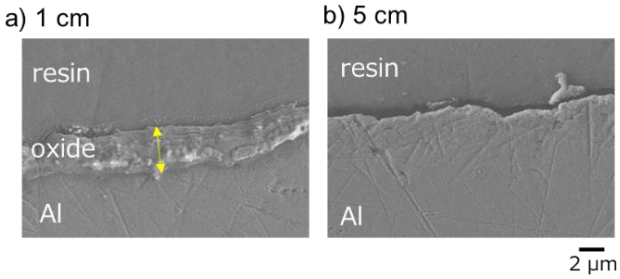

Figure 4.2-8 Cross-sectional SEM images of the inner surface of multi-hole tube at (a) 1 cm and (b) 5 cm from the edge

(2) Attempt to stabilize oxide film formation using an auxiliary electrode

The investigation in Section 4.2.2(1) showed that simply immersing a multiport tube in an aqueous electrolyte solution concentrated the reaction near the flow channel closest to the counter electrode, making uniform surface treatment of the inner walls of the flow channels difficult. Based on this result, as schematically shown in Figure 4.2-9, a counter electrode serving as an auxiliary electrode was installed inside the tube, and its ability to improve treatability to the tube inner wall was examined. Figure 4.2-10 shows photographs of the platinum wire and alumina tube used as the auxiliary electrode. When the conductive platinum wire was inserted into the tube, even slight contact with the inner wall would short-circuit the system and prevent polarization. Therefore, the platinum wire was passed through an alumina tube to maintain the distance between the electrodes.

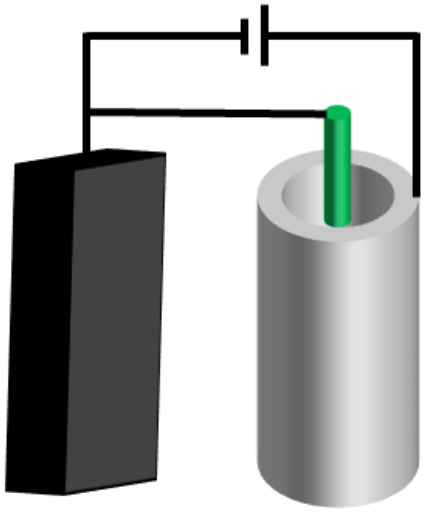

Figure 4.2-9 Schematic illustration of electrolysis with auxiliary electrode

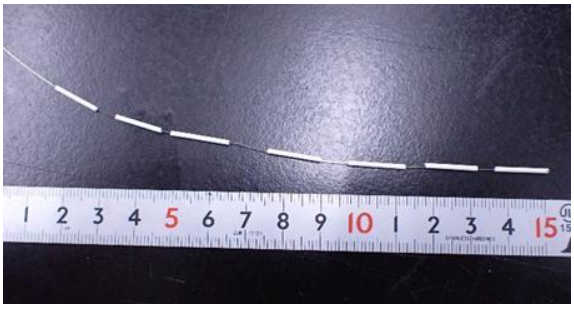

Figure 4.2-10 Platinum wire with alumina tube

Figure 4.2-11 shows SEM observations of the surface and cross section after anodizing was applied to a thin aluminum tube into which an auxiliary electrode had been inserted. As in the previous results, a relatively uniform porous oxide film was observed on the outer surface of the tube; however, no anodic oxide film was formed on the inner wall, and partial irregular dissolution was observed.

These results indicate that uniformly forming a porous oxide film on the inner walls of multiport tubes by anodizing using a simple immersion method is difficult. To improve anodizing treatability, the process likely needs to be combined with a procedure that suppresses localized reactions by eliminating diffusion-limited ion transport, for example through forced electrolyte flow within the flow channels.

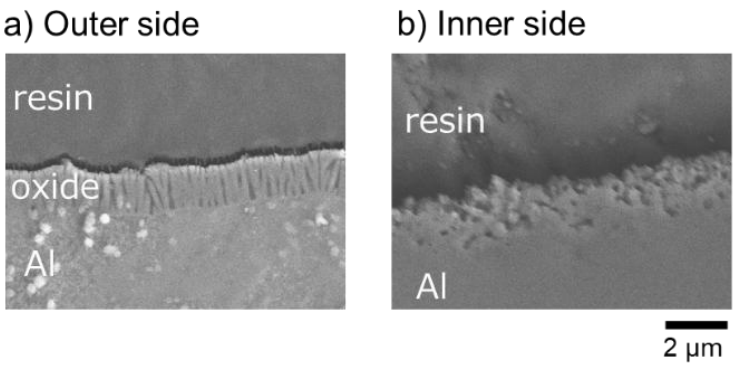

Figure 4.2-11 Cross-sectional SEM images of the (a) outer and (b) inner surface of multi-hole tube after anodizing with auxiliary electrode

(3) Approach to improving heat transfer characteristics by the cross-sectional geometry of multiport tubes

In heat transfer inside multiport tubes, surface tension effects in gas–liquid two-phase flow within microchannels contribute to heat transfer enhancement. Maintaining a high heat transfer coefficient during evaporation requires a structure that continuously supplies the liquid phase to regions where dryout may occur, while retaining a thin liquid film on the heat transfer surface. Therefore, flow-channel cross-sectional geometries aimed at optimizing liquid-film retention were examined, and prototypes were fabricated by extrusion. At present, each heat transfer evaluation group is verifying these samples' heat transfer characteristics, assessing both the improvement in heat transfer coefficient and the effectiveness of the proposed designs.

4.3 Future Issues

The investigations conducted to date have shown that forming fine structures, such as porous structures, on refrigerant flow-channel surfaces can improve the heat transfer coefficient even when refrigerant mixtures are used. By contrast, when anodizing, an electrochemical method for forming porous film structures, was applied using a simple immersion process, uniform fine structures could not be formed inside the flow channels. Accordingly, the heat transfer coefficient will be improved in the latter half of the project through the following two approaches.

The first approach is to continue improving the heat transfer coefficient of refrigerant mixtures through surface treatment. As previous investigations confirmed that forming fine structures on refrigerant flow-channel surfaces can improve the heat transfer coefficient, surface treatment methods that account for throwing power will be examined, and their effects will be verified. The second approach is to improve heat transfer performance by optimizing the structure of multiport tubes. Specifically, heat transfer will be enhanced in extruded multiport tubes by optimizing flow-channel cross-sectional geometry for refrigerant-mixture heat exchange.

Although these investigations will mainly be conducted through laboratory-scale evaluations, a prototype heat exchanger incorporating the knowledge from these approaches is planned for fabrication in the final year of the project, with its heat exchange performance evaluated through wind-tunnel experiments.

References (Section 4)

Hamazaki, T., Takata, Y., Hidaka, S., Shen, B., Takahashi, A., Iwata, N., 2018, Boiling Enhancement of Ethanol by Halloysite Nanotube Coating, *Proc. Therm. Eng. Conf.*, no. 18-2.

Jabardo, J.M.S., Ribatski, G., Stelute, E., 2009, Roughness and Surface Material Effects on Nucleate Boiling Heat Transfer from Cylindrical Surfaces to Refrigerants R-134a and R-123, *Exp. Therm. Fluid Sci.*, vol. 33: p. 579-590.

Kikuchi, T., Nakajima, D., Nishinaga, O., Natsui, S., Suzuki, R.O., 2015, Porous Aluminum Oxide Formed by Anodizing in Various Electrolyte Species, *Curr. Nanosci.*, vol. 11, no. 5: p. 560-571.

Miyara, A., 2015, Recent Directions in Heat Exchanger and Heat Transfer Enhancement, *J. Heat Transfer Soc. Jpn.*, vol. 54, no. 227: p. 12-18.

Nakajima, D., Kurotani, S., Shen, B., Betsuki, Y., Mori, S., Takata, Y., 2025, Lowering the Boiling Initiation Point of Refrigerants on Aluminum Surfaces *via* Formation of Porous Type Anodic Oxide with Re-Entrant Structures, *J. Surf. Sci. Soc. Jpn.*, vol. 76, no. 1: p. 50-53.

Shen, B., Hamazaki, T., Kamiya, K., Hidaka, S., Takahashi, K., Takata, Y., Nunomura, J., Fukatsu, A., Betsuki, Y., 2021, Persistent Reduction of Boiling Incipience of Ethanol on Biphilic Porous Textured Surfaces, *Int. J. Multiphase Flow*, vol. 142: 103739.

5. Elucidation of Thermal-Fluid Mechanisms of Low-GWP Refrigerant Mixtures and Research and Development of Heat Transfer Enhancement Technologies (Kobe University)

HFO-based refrigerants under development as low-GWP refrigerants have low heat transport capacity when used as single-component refrigerants; therefore, their practical application generally requires blending with HFC-based refrigerants. In most refrigerant mixtures, the saturation temperatures of the constituent components differ at the same pressure, resulting in deterioration of heat transfer characteristics during phase-change processes such as evaporation and condensation. For example, during evaporation, the low-boiling-point component preferentially evaporates at the gas-liquid interface, increasing the concentration of the high-boiling-point component in the liquid phase near the interface. Because this concentration exceeds that in the vapor-liquid equilibrium state of the refrigerant mixture, the gas-liquid interface temperature increases, thereby reducing the evaporation heat transfer coefficient. Meanwhile, improving the coefficient of performance of air-conditioners is strongly required from the perspective of energy saving, which necessitates reducing the temperature difference between the refrigerant and air in heat exchangers. At present, because substantial improvement of the overall heat transfer coefficient is difficult, increasing the heat transfer area, that is, enlarging the heat exchanger, is required. Against this background, key issues for heat exchangers include increasing heat transfer area density by reducing refrigerant channel diameter and eliminating concentration non-equilibrium in the liquid phase through refrigerant mixing. Accordingly, the use of flat multiport tubes is considered essential, and research and development are being conducted on the following three topics.

a. Development of prediction models for the thermal-fluid characteristics and void fraction of refrigerant two-phase flow in mini-channels

b. Development of heat transfer enhancement technologies for refrigerant evaporating flow in parallel mini-channels through flow-channel geometry control and oscillatory flow

c. Measurement of the wall superheat at the onset of nucleate boiling and development of methods for its reduction

The outcomes of each topic are presented below.

5.1 Void Fraction and Pressure Loss Characteristics of Zeotropic Refrigerant Mixture Two-Phase Flow in a Horizontal Mini-channel

5.1.1 Background and Objectives

Flat multiport tubes have flow-channel diameters of approximately 1 mm. Because the refrigerant flow-channel diameter is smaller than that in conventional fin-and-tube heat exchangers, whose flow-channel diameters are 4 mm or larger, the influence of surface tension on the gas-liquid interface structure becomes relatively significant when the refrigerant flows as gas-liquid two-phase flow. For example, in horizontal flow through conventional-diameter heat transfer tubes, wavy flow or stratified flow is observed, in which liquid and vapor separates vertically and liquid flows along the bottom of the channel due to gravity. In contrast, in mini-channels, meniscus formation becomes more likely, and the influence of flow direction relative to gravity on heat transfer and flow characteristics becomes smaller; that is, differences in the characteristics among horizontal, vertical upward, and vertical downward flows are considered to be negligible. Such flow-channel diameters are classified as microchannels, and the transition from conventional-diameter channels to microchannels is organized using the Bond number or confinement number, which are defined by the ratio of gravity to surface tension acting on gas-liquid two-phase flow, as shown in Eq. (5.1-1).

$$Bo = \frac{(\rho_{\mathrm{L}} - \rho_{\mathrm{G}})gD^2}{\sigma} = \frac{1}{Co^2} \tag{5.1-1}$$

where, g is the gravitational acceleration, D is the hydraulic equivalent diameter of the flow channel, ρ is the density, and σ is the surface tension; the subscripts L and G denote the liquid and gas phases, respectively. Ong and Thome (2009) defined the transition region to microchannels as Bo = 1.0–11.1, Jige and Koyama (2011) defined it as Bo = 1.1–1.4, and Gomyo and Asano (2016) reported that the influence of surface tension appears when $Bo < 15$. For example, when R1234yf two-phase flow at a saturation temperature of 20 °C flows through a channel with D = 1 mm, the Bond number is 1.55, corresponding to the transition region from conventional-diameter channels to microchannels. In flow with phase change, surface tension is determined by the gas-liquid interface temperature, that is, the saturation temperature corresponding to the vapor pressure. However, for zeotropic refrigerant mixtures, the gas-liquid interface temperature during phase change is unknown because of concentration nonequilibrium, and clarifying its influence is therefore important. Accordingly, in this study, void fraction and pressure loss were measured in an adiabatic section immediately downstream of the heating section for a horizontal channel with an inner diameter of 1 mm. Differences from conventional-diameter channels were evaluated for a pure refrigerant, and the characteristics of a zeotropic refrigerant mixture were also evaluated to find the effect of the concentration nonequilibrium. Void fraction is defined as volumetric fraction of vapor in gas-liquid two-phase flow and is an important parameter characterizing gas-liquid two-phase flow behaviors. If a correlation for the cross-sectional average void fraction is available, the mean velocities of the gas and liquid phases can be obtained from the vapor quality and void fraction. In addition, the amount of refrigerant in a heat exchanger during operation can be evaluated by using void fraction.

5.1.2 Experimental Apparatus and Methods

A schematic diagram of the experimental apparatus is shown in Figure 5.1-1. R1234yf was used as the pure refrigerant, and R454C was used as the zeotropic refrigerant mixture. The working fluid charged in the loop was circulated by a magnetically coupled gear pump, and its mass flow rate was measured using a Coriolis mass flow meter. The gear pump was driven by a motor equipped with a constant-speed control mechanism, enabling a constant flow rate to be supplied regardless of pressure fluctuations in the test section. This feature is essential in experimental systems for very-low-flow-rate gas-liquid two-phase flow. The preheater was a double-tube heat exchanger and maintained the inlet subcooling degree of the main heater within the range of 5–10 K. If electric heating were used for the preheater, the heat input would be accurate; however, the wall superheat would become high, potentially causing subcooled boiling. In that case, the heat input of the main heater and the inlet subcooling degree of the test section could not be measured accurately; therefore, the counterflow double-tube heat exchanger capable of suppressing wall superheat was adopted in this experiment. Upstream of the test section, a thin-walled stainless-steel heat transfer tube with the same inner diameter as the test section, namely the main heater, was installed, and the vapor quality was set by direct electrical heating. Here, the accuracy of heat input is important. In preliminary experiments, heat loss from the main heater was measured under pressurized subcooled-liquid conditions and correlated with the temperature difference between the heat transfer wall and the surrounding environment. The void fraction measurement test section was arranged coaxially and horizontally in series immediately downstream of the main heater. The surrounding environment was maintained at the refrigerant saturation temperature. The refrigerant was condensed in the condenser, became subcooled liquid, and returned to the pump. The pressure in the loop was set by adjusting the temperature of a thermal accumulator installed in a branch line upstream of the pump. In experiments using the refrigerant mixture R454C, liquid refrigerant was collected from a sampling port at the pump outlet, vaporized into superheated vapor, and analyzed for composition using gas chromatography. To monitor the circulating refrigerant composition, a capacitance sensor was installed at the sampling port, enabling real-time monitoring based on capacitance values.

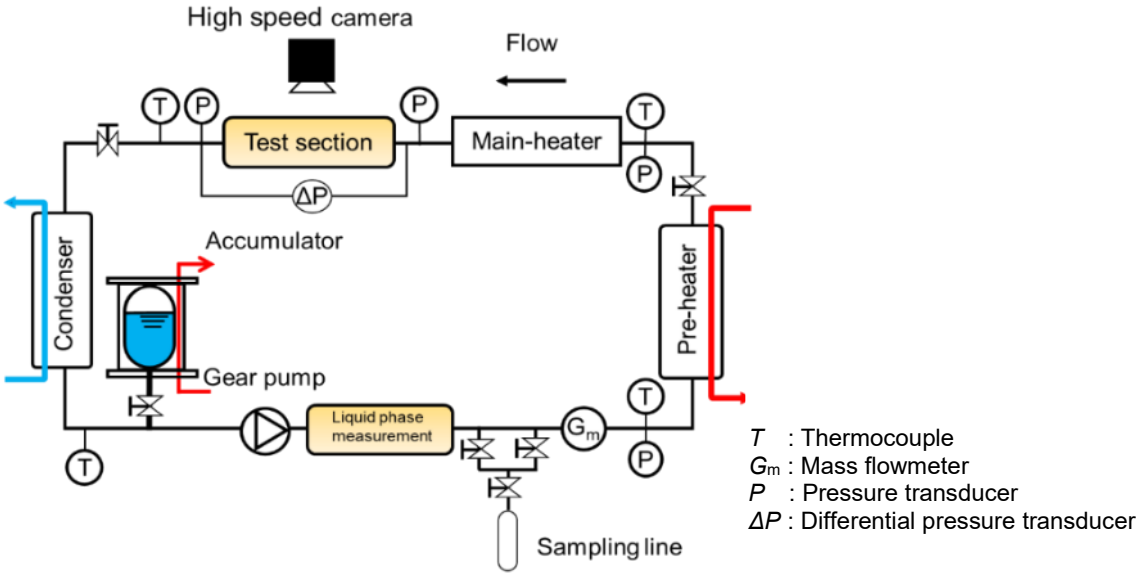

Figure 5.1-1 Schematic diagram of experimental apparatus for two-phase flow experiments in mini-channel.

Details of the measurement test section and the flow-channel cross-sectional geometry are shown in Figure 5.1-2. The measurement test section was made of transparent polycarbonate resin, and a circular channel with a diameter of 1 mm was machined along the central axis and polished to ensure transparency. The inlet and outlet connections were designed to fit into stainless-steel and brass flanges, respectively, and were sealed with O-rings. A capacitance-type void fraction sensor was installed in the recessed portion of the outer wall. The electrodes consisted of stainless-steel plates arranged to sandwich the flow channel from above and below. The flow behavior in the measurement section could be observed from the horizontal direction parallel to the electrode surfaces. A guard electrode was arranged around the sensor electrode to eliminate the influence of floating capacitance in the surroundings. The measurement section of the capacitance sensor was 4.4 mm in the flow direction and 2.0 mm in the channel-width direction; therefore, the measured values represent volume-averaged values over a 4.4 mm section.

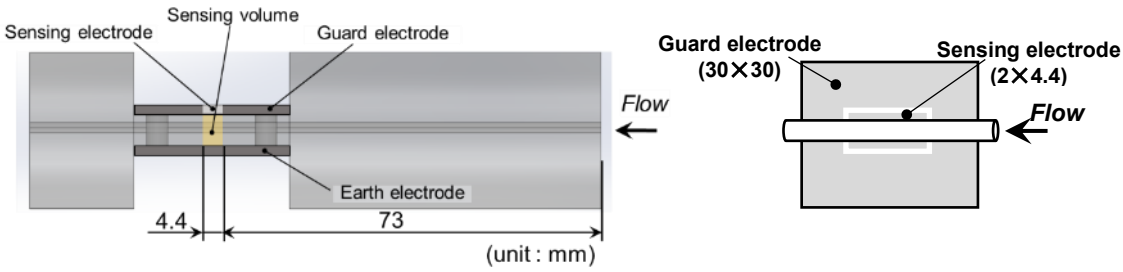

(a) Side view (b) Top view of capacitance sensor

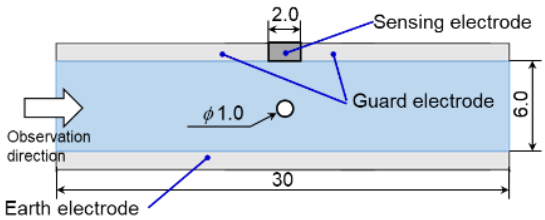

(c) Cross-section at the center of the capacitance sensor

Figure 5.1-2 Detail configuration of measure section.

5.1.3 Experimental Results and Discussion

The flow patterns identified from images captured with a high-speed camera were organized using the Weber number, a dimensionless number representing the ratio of inertia force to surface tension. The definitions of the Weber numbers for the gas and liquid phases are shown in Eq. (5.1-2), respectively.

$$We_{\mathrm{G}} = \frac{\rho_{\mathrm{G}} {j_{\mathrm{G}}}^2 D}{\sigma} \quad , \qquad We_{\mathrm{L}} = \frac{\rho_{\mathrm{L}} {j_{\mathrm{L}}}^2 D}{\sigma} \tag{5.1-2}$$

Here, j_G and j_L are the volumetric fluxes [m/s] of the gas and liquid phases, respectively. These values are calculated from the thermodynamic equilibrium vapor quality. Figure 5.1-3 shows the flow pattern map with the gas-phase Weber number We_{G} on the horizontal axis and the liquid-phase Weber number We_{L} on the vertical axis, together with the flow pattern transition boundaries proposed by Akbar and Ghiaasiaan (2003).

Under high vapor quality conditions, annular flow without disturbance waves was observed, in which the liquid-film interface was smooth and undisturbed. The transition boundary between the inertia-dominated region and the transition region roughly agreed with the model of Akbar and Ghiaasiaan ($We_{\mathrm{G}} = 11 We_{\mathrm{L}}$). Although the model of Akbar and Ghiaasiaan was developed based on experimental results for air–water systems with hydraulic equivalent diameters of 0.866–1.6 mm, the use of the Weber number enables flow patterns to be broadly determined while accounting for tube diameter and fluid properties. For the zeotropic refrigerant, the gas-phase Weber number at which transition to slug flow (intermittent flow), occurred tended to be slightly lower; however, overall, no clear difference from the pure refrigerant was observed.

The temporal fluctuation of void fraction of R1234yf two-phase flow and its probability density function (PDF) are shown in Figures 5.1-4(a)–(c) for each flow pattern: (a) annular flow without disturbance waves, (b) annular flow, and (c) slug flow. The vapor quality x and the average void fraction under each condition are indicated in each figure. Figure 5.1-4(a) shows that the void fraction fluctuation was small and smooth, indicating that no disturbance waves were generated. In contrast, in annular flow (Figure 5.1-4(b)), pulse-like decreases caused by the passing of disturbance waves were observed. Although the length of the measurement section was 4.4 mm, disturbance waves could be detected. As the vapor quality decreased, the flow pattern changed to slug flow, in which liquid slugs blocked the channel. In Figure 5.1-4(c), large decreases in void fraction were caused by the passing of liquid slugs. It was confirmed that the passing frequency of liquid slugs decreased and the liquid velocity decreased with decreasing mass flux; however, no peak at the low void fraction due to liquid-slug passing was observed in the PDF.

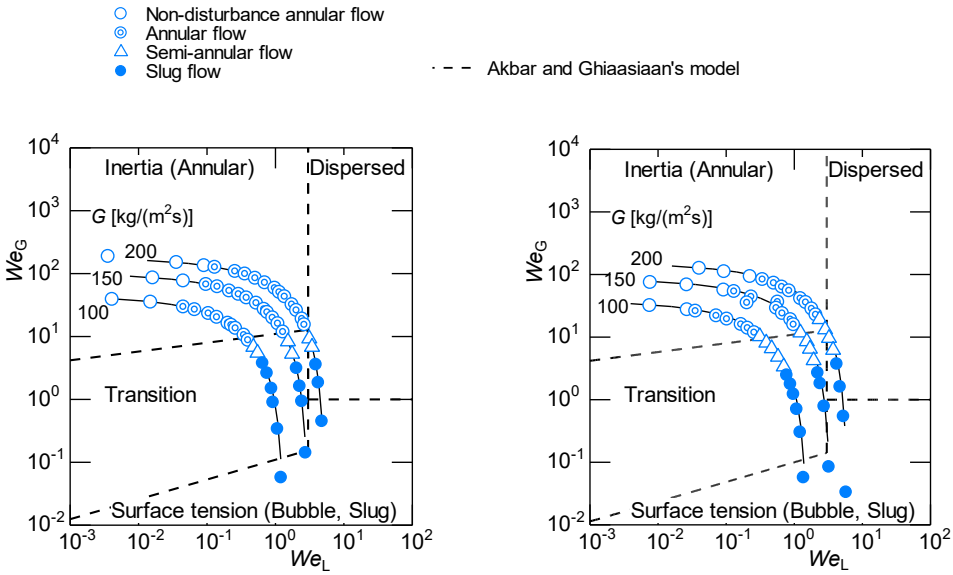

(a) R1234yf (b) R454C

Figure 5.1-3 Flow pattern map with flow pattern transition boundaries proposed by Akbar and Ghiaasiaan

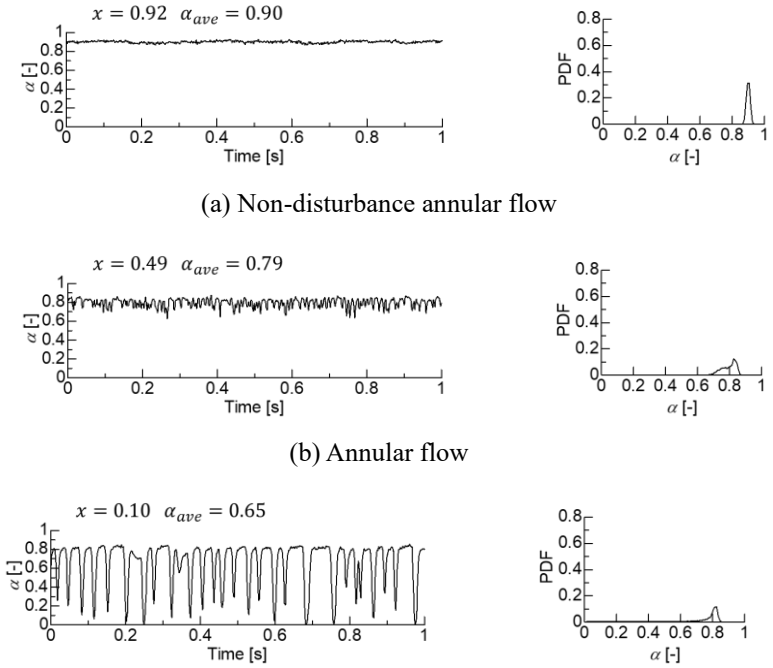

(a) Non-disturbance annular flow

(b) Annular flow

(c) Slug flow

Figure 5.1-4 Void fraction fluctuation and its PDFs (R1234yf, G = 200 kg/(m^2・s)).

Figure 5.1-5 shows the measured time-averaged, volume-averaged void fraction plotted against thermodynamic equilibrium vapor quality. In void fraction measurements of gas-liquid two-phase flow by using the capacitance sensor, the capacitance of the liquid phase is required. For zeotropic refrigerant mixtures, however, the capacitance of the liquid phase varies because the liquid-phase refrigerant composition changes during phase change. Therefore, in this study, the liquid-phase capacitance as a function of refrigerant composition was determined in advance through preliminary measurements using liquid single-phase refrigerant with varied composition. During the void fraction measurements, the capacitance of the liquid phase was calculated from these preliminary results based on the liquid-phase composition assumed under equilibrium conditions. In the figure, the correlation proposed by Cioncolini and Thome (2012) for annular flow in channels, including microscale channels, is shown by the dashed line. For conventional-diameter channels, it is known that the average void fraction is independent of the mass flux. The variation in void fraction with increasing vapor quality roughly agreed with that predicted by the Cioncolini and Thome correlation; however, the void fraction did not asymptotically approach unity and was lower than the correlation. The lower values show the characteristic of gas-liquid two-phase flows in small-diameter channels. For the zeotropic refrigerant mixture, the trend was qualitatively similar to that of the pure refrigerant, although the measured values were slightly lower and the scatter with respect to mass flux was larger. In particular, the large scatter at low vapor quality is considered to be caused by nonequilibrium in the liquid-phase composition. Under the high mass flux condition (G = 200 kg/(m^2・s)), the void fraction was clearly lower at the same vapor quality. This result is also considered to be caused by liquid-phase nonequilibrium. Two effects of nonequilibrium may be involved. The first is its effect on the actual vapor quality. When concentration nonequilibrium exists in the liquid phase, the gas-liquid interface temperature increases and heat transfer deteriorates; therefore, the actual vapor quality at the test section outlet is considered to be lower than the value estimated under equilibrium conditions. The second is its effect on the capacitance sensor. In void fraction measurements, the capacitance value corresponding to a flow channel completely filled with liquid refrigerant at the measurement point is required. For zeotropic refrigerant mixtures, because the liquid-phase concentration changes during phase change, the capacitance of the liquid single phase at prescribed concentrations was measured in preliminary experiments. However, as described above, if nonequilibrium exists in the liquid phase, an error occurs in

the estimated capacitance of liquid single-phase flow.

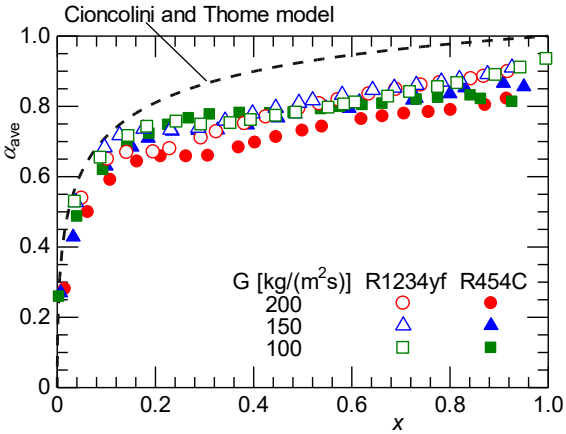

Figure 5.1-5 Time and cross-sectional average void fraction of R1234yf and R454C

The measured pressure loss were organized using the separated-flow model proposed by Lockhart and Martinelli (1949). The organized results are shown in Figure 5.1-6. The horizontal axis represents the Martinelli parameter χ, and the vertical axis represents the two-phase multiplier ϕ_L relative to the pressure loss of liquid single-phase flow. In the figure, the solid lines were obtained by applying the correlation of Kim and Mudawar (2012) to the Chisholm parameter (Chisholm, 1967). The symbols from *t-t* to *l-l* denote the flow states of the gas and liquid phases; *t* denotes turbulent flow, *l* denotes laminar flow, and *t-l* denotes turbulent gas flow and laminar liquid flow. The experimental data are plotted according to flow pattern. For the zeotropic refrigerant mixture, the measured pressure loss of liquid single-phase flow was used to calculate χ and ϕ_L. The results show that the influence of mass flux on the two-phase multiplier is small. For R1234yf, the data agreed with the trend for laminar liquid flow and turbulent gas flow (*l-t*), although the values tended to increase in slug flow. In contrast, for R454C, the trend with respect to χ was largely the same, but the values were lower than those predicted by the Kim and Mudawar correlation. In addition, the tendency for the values to increase in slug flow was more pronounced.

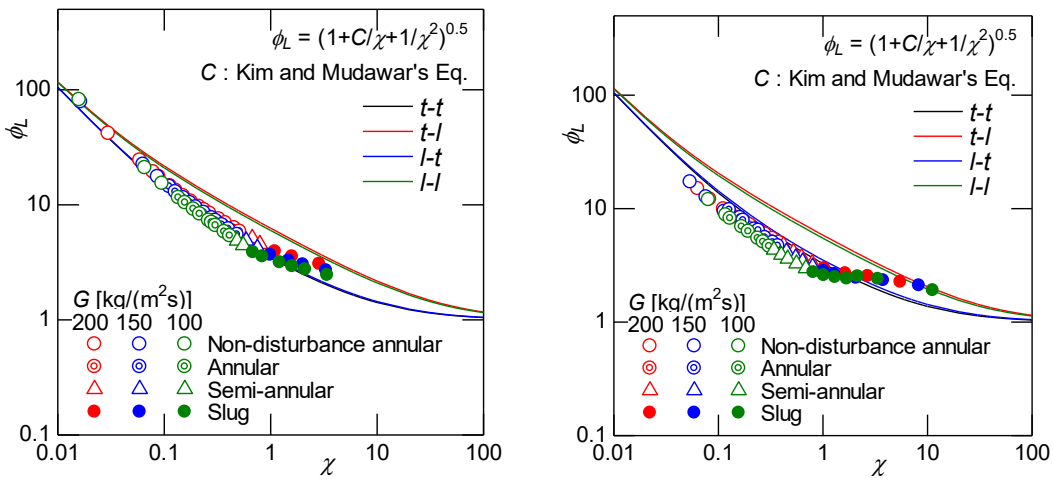

(a) R1234yf (b) R454C

Figure 5.1-6 Frictional pressure loss arranged by the Lockhart-Martinelli method

5.2 Heat Transfer and Flow Characteristics of Refrigerant Evaporating Flow in Parallel Mini-Channels

5.2.1 Background and Objectives

Flat multiport tubes have multiple mini-channels arranged in parallel to reduce pressure loss. Gas-liquid two-phase flow through parallel channels is distributed so that the pressure difference between the inlet and outlet becomes equal. However, because the frictional pressure loss of gas-liquid two-phase flow depends not only on mass flow rate but also on vapor quality, both the flow rate and vapor quality can differ substantially among channels. For evaporative flows, refrigerant distribution becomes complex because acceleration pressure loss accompanies phase change, frictional pressure loss depends on the boiling mode, and flow patterns change as vapor quality increases. In mini- channels, flow-pattern transitions and frictional pressure loss characteristics also differ from those in conventional-diameter channels. Therefore, the factors and occurrence conditions for flow instability, such as refrigerant maldistribution and oscillatory flow in which the flow rate in each channel fluctuates over time, are expected to differ from those in conventional-diameter channels. In general, flow instability leads to deterioration in heat transfer performance and increased pressure loss; however, oscillatory flow may also enhance rewetting of dry-patches and thereby improve heat transfer. Previous studies on parallel evaporator tubes simulating flat multiport tubes (Jige et al., 2014; Ohno et al., 2017; Kurose et al., 2018; Huang et al., 2024) reported the effects of flow-channel geometry, mass flux, and header structure on flow distribution and heat transfer. However, the possibility that the results depend on the experimental apparatus, including the entire refrigerant loop, remains a concern. Therefore, in this study, evaporation experiments using R1234yf as the refrigerant were conducted in horizontal parallel channels consisting of twelve square channels with a hydraulic equivalent diameter of 1 mm, simulating a flat multiport tube, under bottom heating by a heater. Based on flow visualization from the top surface, the presence or absence of flow instability and its influence on heat transfer characteristics were evaluated. The experiments were conducted using a pump-driven refrigerant loop, and a thermal accumulator connected to a branch line of the loop was used to stabilize the loop pressure against volume changes in the loop. The two connection locations were selected, namely the pump inlet and the test section inlet, and the resulting differences were evaluated.

5.2.2 Experimental Apparatus and Methods

A schematic diagram of the experimental apparatus is shown in Figure 5.2-1. The refrigerant circulation loop was driven by a gear pump and consisted of a pre-heater, a test section, and a condenser. The gear pump was of the same type as that used in Section 5.1 and could supply refrigerant at a constant mass flow rate even when the flow resistance in the test section changed. The circulating mass flow rate was measured using a Coriolis mass flow meter installed downstream of the pump. The thermal accumulator used to maintain the loop pressure constant was designed so that it could be connected to either of two locations in the loop: upstream of the pump, position A, or at the test section inlet, position B. In evaporators used in air-conditioners, the inlet pressure is considered to be approximately constant. In contrast, when thermo-fluid experiments on flat multiport tubes are conducted using a pump-driven loop, the boundary condition at the test section inlet is often set as a constant flow rate. When a thermal accumulator is connected at the position A or a refrigerant reservoir is placed upstream of the pump, the pump inlet becomes the fixed-pressure point. In this case, changes in pressure loss in the evaporation test section cause the test section inlet pressure to fluctuate in order to maintain a constant circulating flow rate. Connecting the accumulator to the test section inlet, position B, was intended to simulate practical conditions under which the test section inlet pressure is constant. The vapor quality at the test section inlet was set by the heat input in the preheater.

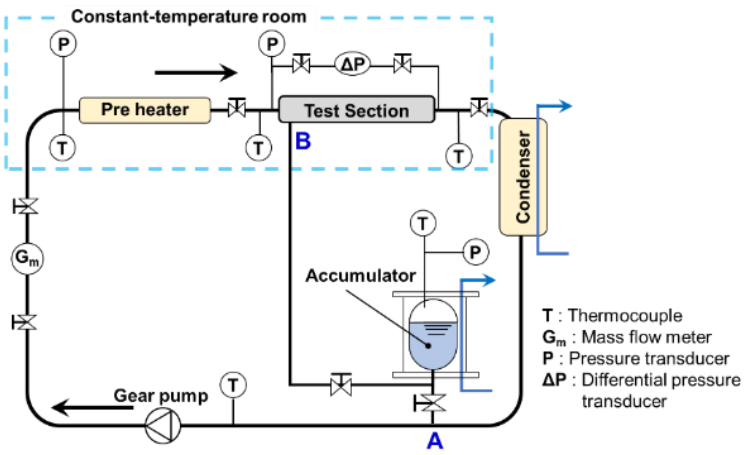

Figure 5.2-1 Schematic diagram of experimental apparatus for evaporating flow experiments in parallel mini-channel.

The structure of the test section is shown in Figure 5.2-2. The test section consisted of an aluminum plate machined with refrigerant channels, sandwiched between a copper heater and a transparent polycarbonate block, and was installed horizontally with the heater facing downward. The heater was heated by two cartridge heaters with a diameter of 6.25 mm embedded in a copper block. The heating length was 200 mm, and the width of the heating surface was the same as the machined channel width. In the inlet header, gas-liquid separation and the resulting maldistribution may occur. Therefore, a foamed aluminum metal plate was installed in the header, and the influence of header volume was evaluated by varying the space Δh between the channel inlet and the foamed metal plate. The heat input Q was defined as the heater input, and the heat flux and heat transfer coefficient were defined based on the wetted perimeter area of the heating section. The wall temperature was defined as the value measured by a sheathed thermocouple installed between the aluminum plate and the heater, assuming that the thermal resistance at the tube wall was sufficiently small. The saturation temperature was calculated from the pressure at the measurement point, obtained by interpolation between the inlet and outlet pressures. The vapor quality at the measurement point was defined as the thermodynamic equilibrium vapor quality, assuming uniform heat-flux heating and neglecting the influence of flow instability.

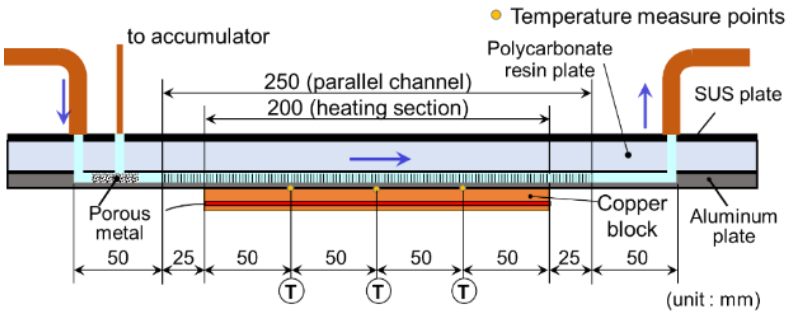

(a) Side view of cross-section in flow direction

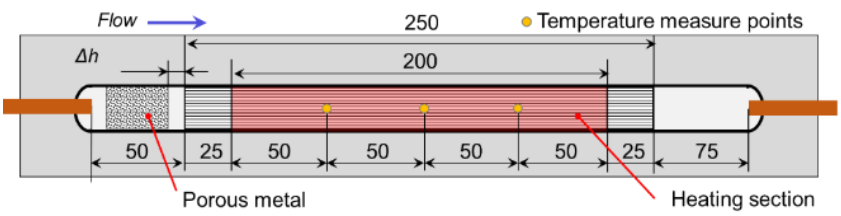

(b)Top view of test section.

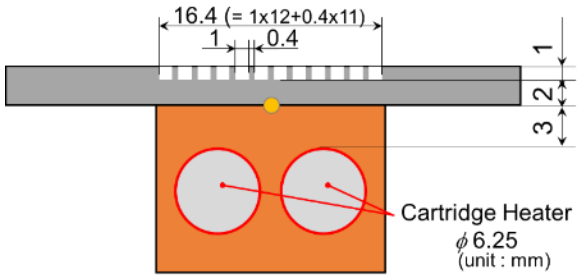

(c) Channel cross-section at the heating section.

Figure 5.2-2 Detail configuration of parallel channel test section.

5.2.3 Experimental Results and Discussion

When the accumulator was connected to the pump inlet, neither maldistribution nor clear oscillatory flow was observed in the test section. In contrast, when the accumulator was connected to the test section inlet, fluctuations in pressure loss in the test section were directly linked to changes in the flow rates entering the parallel channels, confirming that oscillatory flow tended to occur and that its amplitude increased. This effect was particularly pronounced under low mass flux conditions. In addition, when a space was present at the inlet of the parallel channels, backflow occurred owing to changes in pressure loss in each channel, and redistribution was observed from bubble behaviors. The following experimental results correspond to the case in which the accumulator was connected to the test section inlet and the space Δh in the parallel channels was varied.

Figure 5.2-3 shows the local heat transfer coefficient plotted against vapor quality for the varied Δh of 0, 2, and 4 mm. The results correspond to a mass flux of G = 100 kg/(m^2·s) and a heat input of Q = 120 W, corresponding to a heat flux of q = 8.33 kW/m^2. Conditions where no oscillatory flow was observed are plotted using open symbols, whereas conditions where oscillatory flow was observed are plotted using filled symbols. Because there are three measurement points in the flow direction in the test section, the results measured at each point are connected by solid lines. In all cases, the heat transfer coefficient decreased with increasing vapor quality. When Δh = 0 mm, uniform flow distribution would be expected; however, the heat transfer coefficient decreased compared with the case of Δh = 2 mm. At a vapor quality of 0.2, the heat transfer coefficient was lowest for Δh = 4 mm and highest for Δh = 2 mm. In contrast, at a vapor quality of 0.6, the heat transfer coefficient decreased markedly for Δh = 0 mm, where no oscillatory flow was observed. When Δh = 4 mm, the measured results exhibited scatter, with values distributed between those for Δh = 0 mm and Δh = 2 mm. This scatter is considered to be attributable to the dependence of the flow state on the inlet flow conditions.

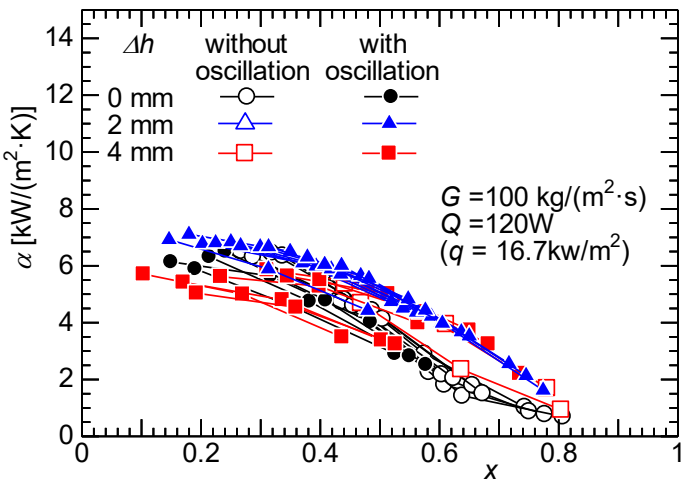

Figure 5.2-3 Local heat transfer coefficient

Since these results are considered to be due to differences in the internal flow structure, the factors causing them were examined based on the visualization images. An example of the observed images is shown in Figure 5.2-4, where continuous frames are presented at intervals of 1/30 s. Because the entire test section was captured, the spatial resolution was insufficient; therefore, for annular flow, the liquid film was too thin to be detected. However, at low vapor quality, liquid plugs and bubbles in the channels could be observed in the videos because gas-liquid interfaces crossing the channel cross-section appeared white. For example, the red lines in the figure connect the same interfaces, showing that their moving velocities differed among channels. When a gas-liquid interface exists such that the channel is blocked by bubbles or liquid plugs, the image brightness changes significantly. The motion of this interface is considered to correlate with the flow rate fluctuation in each channel. Therefore, oscillatory flow can be evaluated by tracking the interface over time. Accordingly, the brightness distribution in the flow direction at the center of a channel was extracted and stacked with respect to time to create time-strip images. The obtained results for Δh = 0 mm and Δh = 4 mm are shown in Figures 5.2-5(a) and (b), respectively. In each figure, the left side shows the brightness distribution for the outermost channel, channel 1, and the right side shows that for the central channel, channel 6. The inlet vapor quality of the test section was low, 0.27, and the vapor quality reached 0.97 at the outlet. In the figure, the heating section is indicated by a red frame. The horizontal axis represents the flow direction, and the vertical axis represents the progression of time from top to bottom. The white lines indicate movement of the gas-liquid interface. Unless the flow reverses, the interface moves toward the lower left, and its slope indicates the velocity. Movement toward the left indicates reverse flow. For Δh = 0 mm, no oscillatory flow was observed, whereas for Δh = 4 mm, fluctuations were observed, indicating that oscillatory flow occurred throughout the channels. This flow-rate fluctuation is considered to have suppressed bubble nucleation near the test section inlet and expanded the periods and area of low-flow-velocity, thereby deteriorating the heat transfer coefficient. At low vapor quality, nucleate boiling plays a major role in heat transfer, so the influence of mass flux was small; however, temporal changes in flow velocity enhance bubble departure, and oscillatory flow consequently led to heat transfer deterioration. In contrast, near the outlet at high vapor quality, no gas-liquid interface was observed at the channel center along the flow direction for the Δh = 0 mm case, and the brightness was uniform. For the Δh = 4 mm case, however, gas-liquid interfaces were observed, indicating that liquid phase remained. Oscillatory flow is therefore considered to have rewetted dry patches downstream, resulting in a higher heat transfer coefficient for Δh = 4 mm than for Δh = 0 mm.

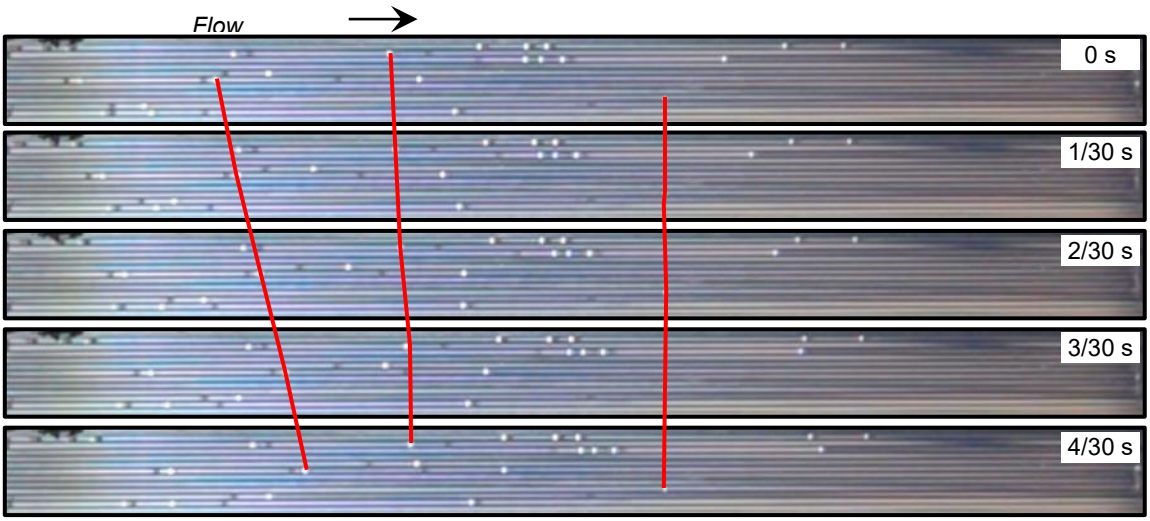

Figure 5.2-4 Continuous images of evaporating flow behaviors.

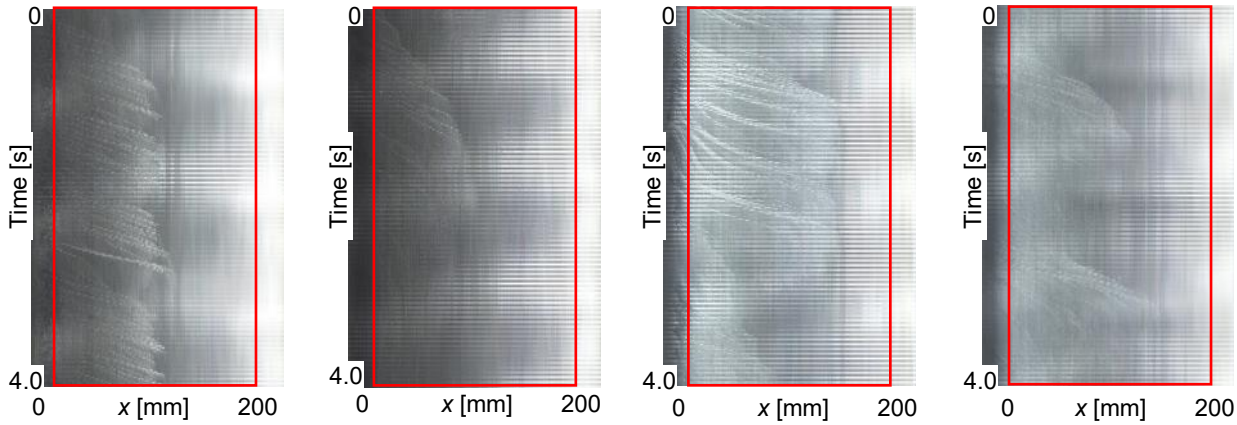

(a) Δh = 0 mm, x_{in} = 0.271, x_{out} =0.945 (b) Δh = 4 mm, x_{in} = 0.270, x_{out} =0.9445

Figure 5.2-5 Time strip visualization of experimental results:
Effect of the gap between porous metal and parallel flow channels
at G = 100 kg/(m^{2}s), Q = 120 W, q = 8.33 kW/m^2.

5.3 Development of Evaluation and Improvement Methods for Nucleate Boiling Heat Transfer and Boiling Incipience Superheat in Non-Azeotropic Refrigerant Mixtures

5.3.1 Background and Objectives

The results of the study on the flow characteristics of refrigerant two-phase flow in mini-diameter channels described in Section 5.1 showed that the influence of surface tension becomes relatively large compared with that of gravity, resulting in a lower void fraction, that is, a thicker liquid film, than in conventional-diameter channels. In addition, the results of the study on the heat transfer and flow characteristics of refrigerant two-phase flow in parallel evaporating channels described in Section 5.2 showed that, when the inlet pressure of the parallel channels is maintained constant, oscillatory flow occurs in response to changes in pressure loss through the parallel channels. Oscillatory flow decreased the heat transfer coefficient at low vapor quality by suppressing nucleate boiling, whereas at high vapor quality it improved the heat transfer coefficient by rewetting dry patches. Meanwhile, previous studies (Shiga et al., 2024) have reported that, in evaporation flow experiments using flat multiport tubes heated by a heat transfer medium, extremely low heat transfer coefficients were observed at low vapor quality due to delayed onset of nucleate boiling. During evaporation of zeotropic refrigerant mixtures, the concentration non-equilibrium in the liquid phase near the gas-liquid interface increases the gas-liquid interface temperature, thereby reducing the evaporative heat transfer coefficient (Takamatsu et al., 1993; Watanabe et al., 2016; Kondou et al., 2014). Therefore, eliminating the concentration non-equilibrium is essential to improve the heat transfer coefficient, and liquid-film agitation is an effective means for achieving this. Although disturbing the boundary layer by microstructures on the channel wall is effective for the agitation, boiling bubble nucleation within a thick liquid film is expected to promote liquid-film agitation and prevent formation of a stable thick liquid film. Accordingly, this study was conducted to clarify the wall superheat at the onset of nucleate boiling and to develop methods for reducing it. The nucleate boiling heat transfer coefficient in forced convection flow is governed by gas-liquid interface formation near the heat transfer surface, bubble growth, and liquid-film agitation caused by bubble departure, and the heat transfer coefficient can be organized in the same manner as nucleate boiling heat transfer in pool boiling. Therefore, the wall superheat at the onset of nucleate boiling and nucleate boiling heat transfer coefficient were evaluated through pool boiling experiments.

5.3.2 Experimental Apparatus and Experimental Methods

A schematic diagram of the experimental apparatus is shown in Figure 5.3-1. The refrigerant was charged into a stainless-steel pressure vessel, and a copper heat transfer surface was installed on the bottom flange. The saturated vapor pressure was controlled using a chilled-water coil installed in the upper space of the pressure vessel. The heat transfer surface was heated by a cartridge heater inserted from the lower end of a copper cylinder. To observe the boiling behavior, an observation window was installed on the side of the pressure vessel, and images were captured from the horizontal direction using a high-speed camera at 1000 fps. After the pressure vessel was evacuated using a vacuum pump, refrigerant was charged so that the liquid level was approximately 50 mm above the heat transfer surface. Refrigerant vapor generated by boiling was condensed on the cooling coil, and the condensed liquid returned to the liquid pool by gravity. To prevent heat loss from the pressure vessel and heat input from the surroundings, the pressure vessel was covered with thermal insulation, and the ambient temperature was maintained at approximately the saturation temperature by using insulated walls and A chilled-water coil. Liquid refrigerant was sampled from the lower part of the pressure vessel, and its composition ratio was measured by gas chromatography. The thermophysical properties of the zeotropic refrigerant mixture were calculated using REFPROP Ver. 10.0 based on the measured composition ratio.

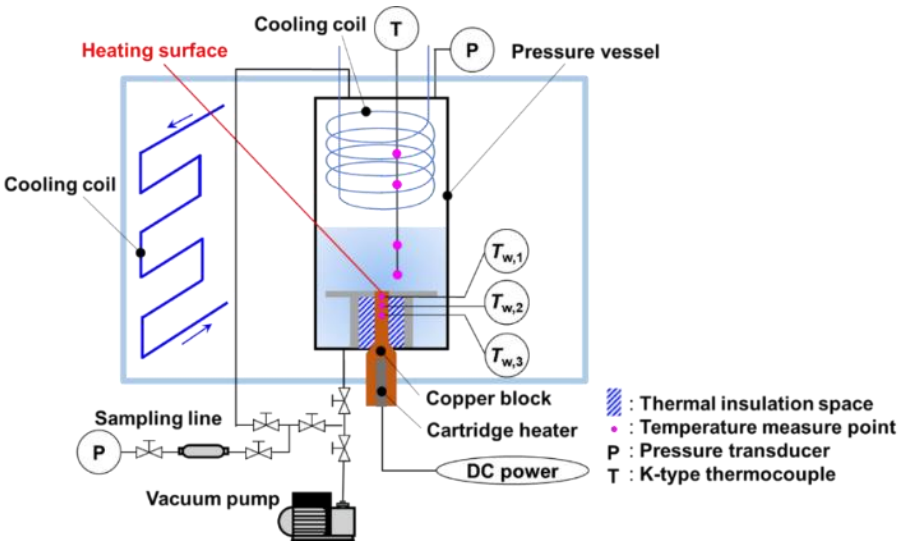

Figure 5.3-1 Schematic diagram of experimental apparatus for pool boiling experiments

Details of the heating test section are shown in Figure 5.3-2. The heating test section consisted of a copper cylinder with a circular smooth heat transfer surface 10 mm in diameter. The heater insertion section had a diameter of 15 mm and a length of 60 mm, and a cartridge heater with a diameter of 6 mm and a length of 50 mm was inserted from the bottom. The temperature of the copper cylinder was measured using K-type sheathed thermocouples inserted at three points along the central axis of the cylinder: one point located 5 mm from the heat transfer surface and two additional points located at 5 mm intervals from that point. The heater input was controlled by the voltage supplied from a stabilized DC power source. The heat transfer surface was polished with #400 sandpaper, assuming the surface roughness of a typical heat transfer tube. In the experiment, the temperatures of refrigerant vapor and liquid, ambient temperature, temperature distribution in the copper cylinder, pressure inside the pressure vessel, pressure in the sampling vessel, and heat input were measured using a data logger at a sampling frequency of 2 Hz. In temperature measurements using K-type thermocouples, external cold-junction was applied using a Zerocon unit (Coper Electronics Co. Ltd., ZA 114A). The heat flux q was obtained from the temperature gradient dT/dx in the copper cylinder, and the wall superheat ΔT_{wall} and heat transfer coefficient α were determined using the following equations.

$$\alpha = q/\Delta T_{\mathrm{wall}} \tag{5.3-1}$$

$$q = -\lambda(dT/dx) \tag{5.3-2}$$

$$\Delta T_{\mathrm{wall}} = T_{\mathrm{wall}} - T_{\mathrm{sat}} \tag{5.3-3}$$

The pressure inside the vessel was maintained by adjusting the temperature of the cooling water in the condenser, and the saturation temperature was maintained at 20 °C. The heat input Q was varied stepwise over the range of 0.25–25 W. To evaluate the onset of nucleate boiling, measurements of the nucleate boiling heat transfer coefficient were conducted during the heat-input increasing process. In measuring the nucleate boiling heat transfer coefficient, after the maximum heat input was reached during the heat-flux increasing process, measurements were also conducted during the heat-flux decreasing process to evaluate hysteresis in the boiling curve. In order to accurately measure the wall superheat at the onset of nucleate boiling, the heat-input increment was reduced under heating conditions close to the onset of nucleate boiling, and measurements were performed under conditions approximating a quasi-steady state.

The refrigerants used were R454C, a zeotropic refrigerant mixture; R1234yf, the high-boiling-point constituent refrigerant of R454C; and R134a, which was used as a reference pure refrigerant. Experiments using pure R32 were not conducted because of limitations of the pressure vessel.

5.3.3 Experimental Results and Discussion

Figure 5.3-3 shows the temporal change in the wall temperature of the heating section for the zeotropic refrigerant mixture R454C. The wall temperature increased with a first-order delay as the heat input was increased stepwise. The point at which the wall temperature decreased abruptly corresponds to the onset of nucleate boiling (ONB), which occurred during the wall-temperature increasing process in this case. In this experiment, the heat transfer surface temperature was measured from the temperature gradient in the copper cylinder. However, during transient changes involving abrupt temperature drop, a large error occurs between the actual heat transfer surface temperature and the surface temperature estimated under the assumption of a linear wall-temperature distribution. During the heat-input increasing process, the temperature rise is larger at locations closer to the heater, and therefore the heat flux calculated from the temperature gradient increases with increasing distance from the heat transfer surface. Thus, the heat transfer surface temperature estimated from the temperature distribution during transient changes is likely to be underestimated. Accordingly, the increment in heat input was reduced under heating conditions close to ONB so that a quasi-steady state could be obtained. Figure 5.3-4 shows the temporal change in the wall temperature of the heating section when the heat-input increment was reduced. The temporal variation in wall temperature at ONB was suppressed to a small level, indicating that the system was in a quasi-steady state. Under this condition, the wall-temperature distribution in the heating section obtained just before boiling incipience is shown in Figure 5.3-5. Because the temperatures measured at the three points were nearly linear, the boiling incipience superheat was confirmed to have been measured accurately.

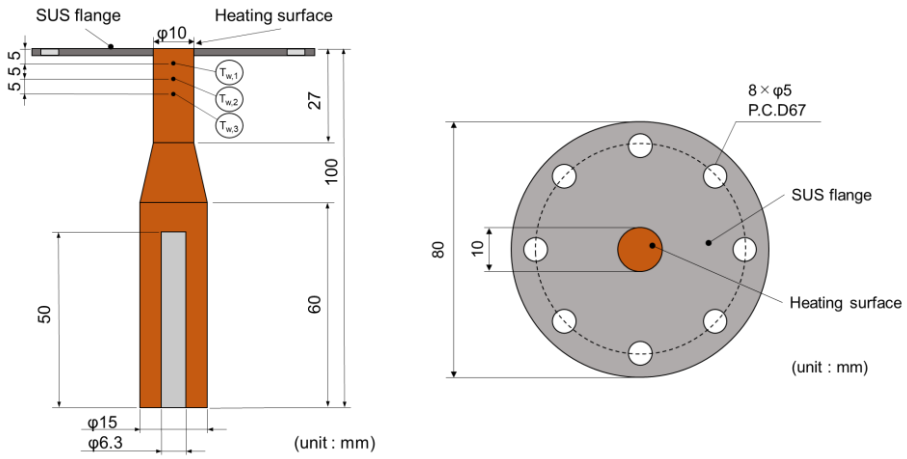

(a) Cross-sectional side view (b) Top view

Figure 5.3-2 Detail configuration of heating section for pool boiling.

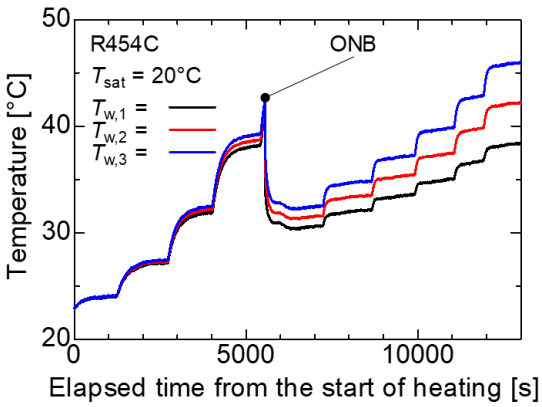

Figure 5.3-3
Temporal change of heating block temperature in rough measurement.

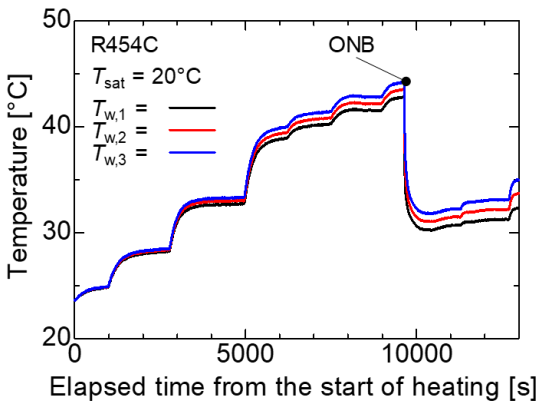

Figure 5.3-4
Temporal change of heating block temperature in precise measurement.

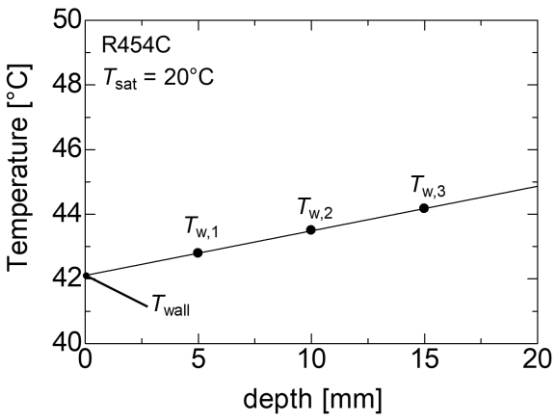

Figure 5.3-5 Temperature distribution in copper block just before the ONB.

The boiling curves obtained for each refrigerant are shown in Figure 5.3-6, and the heat transfer coefficients are shown in Figure 5.3-7. In these figures, the wall superheat at the onset of nucleate boiling (ONB) is indicated by double-line symbols, and the corresponding values are summarized in Table 5.3-1. The wall superheat is defined as the

temperature difference between the wall temperature and the saturation temperature corresponding to the pressure inside the vessel; for zeotropic refrigerant mixtures, it is defined as the temperature difference between the wall temperature and the bubble-point temperature. At the lowest heat flux in the experiment, the system was in a non-boiling state. When the heat flux was increased under non-boiling condition, the wall superheat increased under natural-convection conditions. No significant difference was observed between R134a and R1234yf, whereas R454C showed a lower wall superheat, particularly under low-heat-flux conditions. The wall superheat at the ONB was lowest for R134a. As shown in Figure 5.3-6, boiling incipience for R454C occurred at a heat flux comparable to that for R1234yf; however, the wall superheat was approximately 3 K higher. This is considered to be because, in zeotropic refrigerant mixtures, the low-boiling-point component preferentially evaporates in the initial bubble, and the liquid refrigerant near the gas-liquid interface becomes enriched in the high-boiling-point component, thereby increasing the interface temperature. As a result, bubble growth in R454C requires a larger wall superheat than R1234yf. Focusing on the heat transfer coefficient in the developed nucleate boiling region, the heat transfer coefficient of R454C was approximately 40% lower than those of the pure refrigerants. As described above, this decrease is considered to result from suppression of vaporization due to the increase in interface temperature, which increases the temperature of the superheated liquid layer.

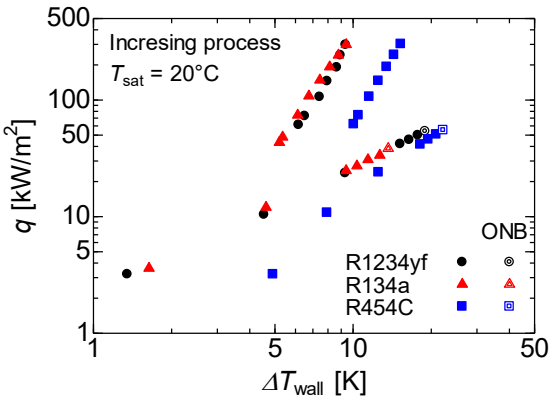

Figure 5.3-6
Boiling curve for each refrigerant measured in heat flux increasing process.

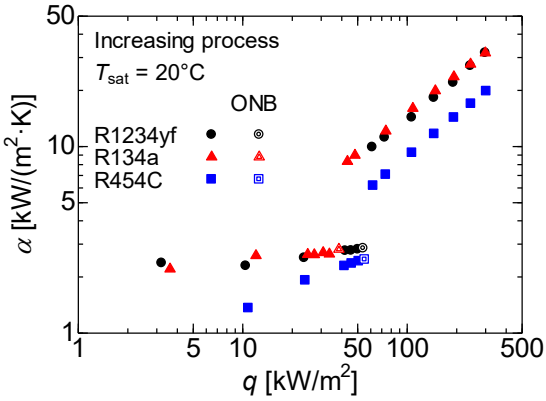

Figure 5.3-7
Heat transfer coefficient for each refrigerant measured in heat flux increasing process.

Table 5.3-1 Wall superheat at onset of nucleate boiling.

	R454C	R1234yf	R134a
q [kW/m^2]	55.16	53.99	38.43
ΔT_{wall} [K]	22.24	18.94	13.65

Figure 5.3-8 shows snapshots from high-speed camera images of boiling behavior under the same heat-input condition. The boiling behaviors are shown for R454C (Figure 5.3-8(a)), R1234yf (Figure 5.3-8(b)), and R134a (Figure 5.3-8(c)). The images confirmed differences in bubble departure diameter among the refrigerants. Compared with R454C, the pure refrigerants exhibited larger bubble departure diameters, indicating that a larger amount of vapor was generated on the heat transfer surface. This effect is considered to have resulted in higher heat transfer coefficients for the pure refrigerants. Thus, the cause of the heat transfer deterioration in zeotropic refrigerant mixtures were confirmed based on the observed boiling behavior.

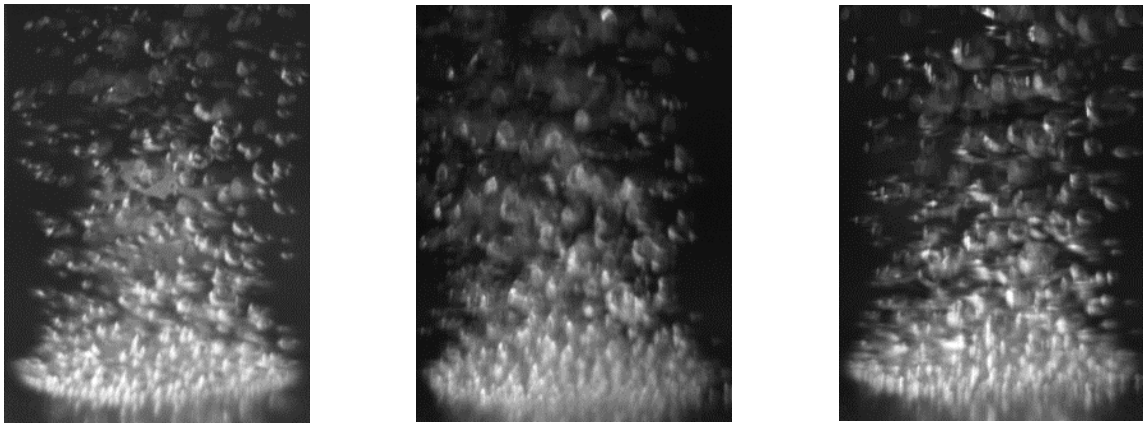

(a) R454C (b) R1234yf (c) R134a

Figure 5.3-8 Boiling behaviors for each refrigerant at the same heating rate.

Next, the effects of saturation temperature and composition ratio were evaluated for zeotropic refrigerant mixtures. The refrigerants used were R32/R1234yf zeotropic refrigerant mixtures and the pure refrigerant R1234yf. The composition ratios of the refrigerant mixtures used in this experiment are summarized in Table 5.3-2; hereafter, each refrigerant is denoted by the fraction of R32. For the 20% case, the measured composition obtained by sampling was 22.9/77.1%, which was close to that of R454C (21.5/78.5%). Figure 5.3-9 shows the boiling curves during the heat-flux increasing process for the zeotropic refrigerant mixture in the 10% case. The onset of nucleate boiling is indicated by open symbols. As the mode transitioned from natural convection to nucleate boiling after the ONB, the wall superheat decreased sharply and the heat transfer coefficient increased. The effect of saturation temperature on heat transfer performance in the developed nucleate boiling was small. Table 5.3-3 shows the wall superheat at the ONB together with the saturation pressure and surface tension. The surface tension is the value at a saturation temperature of 20 °C for the composition ratio of 9.6/90.4%. The wall superheat at the ONB decreased with increasing saturation temperature, which is considered to be attributable to an increase in vapor pressure inside the bubbles and a decrease in surface tension.

Table 5.3-2 Mixture ratio of R1234yf in R32/R1234yf zeotropic refrigerant mixtures.

	0%	10%	20%	40%	50%
Mass fraction of R32 [wt%]	0	9.6	22.9	40.8	49.7
Mass fraction of R1234yf [wt%]	100	90.4	77.1	59.2	50.3

Table 5.3-3 Wall superheat at the onset of nucleate boiling, saturation pressure, and surface tension.

T_{sat} [°C]	5	10	20
$\Delta T_{wall, ONB}$ [K]	35.11	23.62	14.36
P_{sat} [MPa]	0.5571	0.6463	0.8561
σ [mN/m]	8.572	7.867	6.507

Figure 5.3-10 shows the boiling curves obtained when the composition ratio was varied at a saturation temperature of 20 °C, and Table 5.3-4 shows the corresponding wall superheat at the ONB. The influence of composition ratio on the wall superheat at the ONB was small, and the values were nearly identical to those of the pure refrigerant R1234yf. When the R32 fraction was set to 50%, the wall superheat at the ONB became lower than that of the pure refrigerant.

This is considered to be because, although the low-boiling-point component, R32, preferentially evaporates during initial bubble formation, the change of local concentration in the liquid near the gas-liquid interface remains small even when sufficient vapor is generated for bubble departure, thereby suppressing the increase in boiling point. The nucleate boiling heat transfer coefficients of all refrigerant mixtures were lower than that of R1234yf. However, the heat transfer coefficient increased as the fraction of the low-boiling-point component increased.

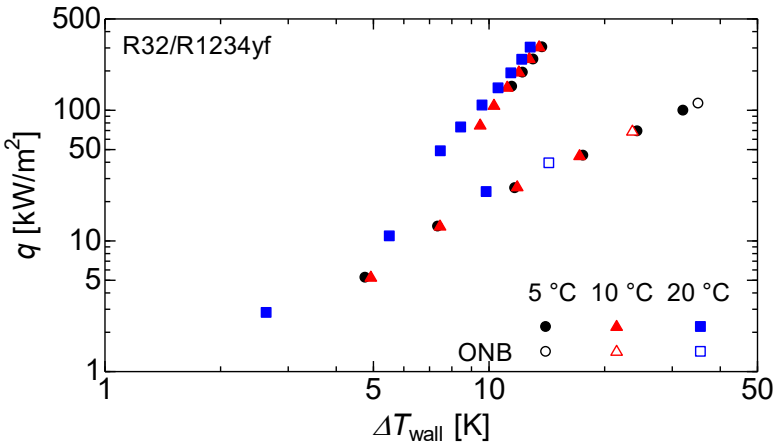

Figure 5.3-9 Boiling curves of zeotropic refrigerant mixtures (R32/R1234yf : 9.6/90.4 %)

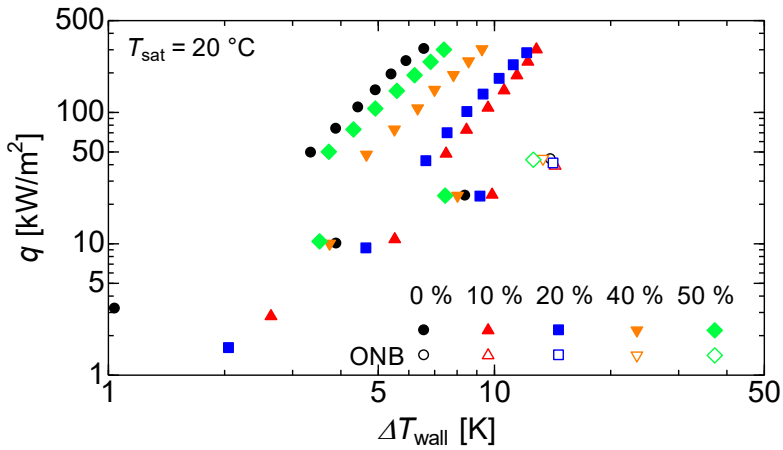

Figure 5.3-10 Boiling curve for refrigerant with several mixing ratio at T_{sat} = 20 °C.

Table 5.3-4 Wall superheat at the onset of nucleate boiling for each refrigerant with varied mixing ratio.

Mass fraction of R32 [wt%]	0%	10%	20%	40%	50%
$\Delta T_{wall,\ ONB}$ [K]	13.99	14.36	14.23	13.35	12.61

5.4 Summary

At Kobe University, research and development were conducted on the flow characteristics of refrigerant two-phase flow in min-channels, the heat transfer and flow characteristics of refrigerant evaporating flow in parallel mini-channels, and nucleate boiling heat transfer characteristics, all of which play important roles in evaporative heat transfer in noncircular mini-channels. The principal outcomes of these research and development activities are summarized below.

a. Heat transfer and flow Characteristics and Void Fraction Characteristics of Refrigerant Two-Phase Flow in Mini-channels

Horizontal gas-liquid two-phase flow experiments were conducted in a circular tube with an inner diameter of 1 mm using the pure refrigerant R1234yf and the zeotropic refrigerant mixture R454C. Flow patterns, void fraction, and pressure loss were evaluated. Slug flow, semi-annular flow, annular flow, and annular flow without disturbance waves were observed. The flow-pattern map organized using the gas- and liquid-phase Weber numbers, WeG and WeL, roughly agreed with the flow-regime transition model proposed by Akbar and Ghiaasiaan. However, for R454C, the transition to annular flow tended to occur at slightly higher WeG values, corresponding to higher gas velocities. The void fraction exhibited a trend similar to that predicted by the correlation of Cioncolini and Thome, although the measured values were lower than the correlation. The void fraction of R454C was slightly lower than that of R1234yf. Because the measurements were conducted just downstream of the heated section, the actual vapor quality of R454C may have been lower owing to delayed phase change. Frictional pressure loss could be correlated using the Lockhart-Martinelli method. The two-phase multiplier of R454C was lower than that predicted by the correlation of Kim and Mudawar, suggesting a possible influence of large temperature variation at low vapor quality.

b. Oscillatory Flow in Refrigerant Evaporating Flow within Parallel Mini-Channels and Its Effect on Heat Transfer Characteristics

Evaporation heat transfer experiments were conducted in horizontal parallel mini-channels simulating flat multiport tubes, and the effects of inlet-header volume on flow behavior and heat transfer characteristics were evaluated. Under conditions in which a mechanical gear pump supplied a constant mass flow rate and the pump inlet pressure was maintained constant, no significant oscillatory flow or flow maldistribution was observed in the parallel channels. In contrast, when the pressure at the inlet of the parallel channels was maintained constant to simulate practical heat exchangers by using a thermal accumulator, the flow became increasingly unstable as the inlet-header volume increased, and reverse flow from the parallel channels into the inlet header was also observed. This oscillatory flow reduced the heat transfer coefficient at low vapor quality by suppressing nucleate boiling. However, at high vapor quality, heat transfer deterioration was suppressed through the rewetting of dry patches, resulting in an increase in the average heat transfer coefficient.

c. Identification of Wall Superheat at Onset of Nucleate Boiling and Influence of Zeotropic Refrigerant Composition Ratio

Pool boiling experiments were conducted to evaluate wall superheat at the onset of nucleate boiling and nucleate boiling heat transfer characteristics. Compared with pure refrigerants, R454C exhibited a higher wall superheat of 22.24 K, which was 1.17 times that of R1234yf. The heat transfer coefficient in the developed nucleate boiling region for R454C was approximately 40% lower than those of the pure refrigerants. However, the dependence on heat flux was nearly the same as that of the pure refrigerants. In addition, experiments were conducted using R32/R1234yf zeotropic refrigerant mixtures with varying R32 composition ratios. The results showed that the effect of composition ratio on wall superheat at the onset of nucleate boiling was small and that the values were nearly the same as those for pure R1234yf, the higher-boiling-point component. In contrast, the nucleate boiling heat transfer coefficient decreased as the R32 fraction decreased. The reduction in the nucleate boiling heat transfer coefficient in pool boiling is attributed to a decrease in the evaporation rate during bubble growth. Therefore, if nucleate boiling becomes dominant in forced-flow evaporation within mini-channels, liquid-film agitation is expected to suppress deterioration in heat transfer performance.

These results clarified that, in refrigerant two-phase flow within small diameter square channels, the influence of

refrigerant surface tension becomes relatively strong, resulting in thicker and smoother liquid films in annular flows. For zeotropic refrigerant mixtures, this characteristic further deteriorates evaporation heat transfer performance compared with that in conventional-diameter channels. This tendency is also consistent with the slightly lower average void fraction observed for zeotropic refrigerant mixtures than for pure refrigerants. Therefore, agitation of the stable liquid film is essential. In future work, three approaches will be pursued. The first is utilization of flow instability. Although the conditions for flow instability occurrence under uniform heat-flux conditions were clarified in Section 5.2, evaluations under more practical conditions involving longer heated sections and nonuniform heating will be conducted. The second is promotion of nucleate boiling through surface modification aimed at reducing wall superheat at the onset of nucleate boiling. The third is control of flow direction relative to gravity. Although flat multiport tubes are generally installed horizontally from the viewpoint of air-side drainage, vertical installation may be advantageous from the standpoint of refrigerant distribution into parallel channels. Therefore, the effects of tube orientation and flow direction on evaporation heat transfer in a single flat multiport tube will be evaluated. Furthermore, to assess the effect of refrigerant distribution, a simple wind tunnel capable of evaluating heat exchanger performance with different installation angles will be developed. The system will consist of a refrigerant supply loop and a wind tunnel with the cross-sectional area of 200 × 200 mm². This system will be used to verify the effectiveness of flow agitation.

References (Section 5)

Akbar, M.K., Plummer, D.A., Ghiaasiaan, S.M., 2003, On Gas-Liquid Two-Phase Flow Regimes in Microchannels, *International Journal of Multiphase Flow*, vol. 29: p. 855-865.

Chisholm, D., 1967, A Theoretical Basis for the Lockhart–Martinelli Correlation for Two-Phase Flow, *International Journal of Heat and Mass Transfer*, vol. 10: p. 1767-1778.

Cioncolini, A., Thome, J.R., 2012, Void Fraction Prediction in Annular Two-Phase Flow, *International Journal of Multiphase Flow*, vol. 43: p. 72-84.

Gomyo, T., Asano, H., 2016, Void Fraction Characteristics of One-Component Gas-Liquid Two-Phase Flow in Small Diameter Tubes, *Interfacial Phenomena and Heat Transfer*, vol. 4: p. 1-18.

Huang, Y., Chen, K., Tang, X., Fang, Y., 2024, Two-Phase Flow Oscillation and Distribution in Parallel Channels During R1233zd(E) Subcooled Flow Boiling: A Numerical Study, *International Journal of Heat and Mass Transfer*, vol. 218: paper no. 124778.

Jige, D., Koyama, S., 2011, Experiments on Condensation of R1234ze(E) in a Multi-Port Extruded Tube, *Trans. of the JSRAE*, vol. 28, no. 3: p. 225-232. (in Japanese)

Jige, D., Komiya, Y., Kondou, C., Koyama, S., 2014, Boiling Heat Transfer and Pressure Drop of R1234ze(E) and R32 in a Multi-Port Tube, *Trans. of the JSRAE*, vol. 31, no. 2: p. 57-65. (in Japanese)

Kim, S.M., Mudawar, I., 2012, Universal Approach to Predicting Two-Phase Frictional Pressure Drop for Adiabatic and Condensing Mini/Micro-Channel Flows, *International Journal of Heat and Mass Transfer*, vol. 55: p. 3246-3261.

Kondou, C., Mishima, F., Koyama, S., 2014, Condensation and Evaporation of Low GWP Refrigerant Mixture R32/R1234ze(E) in Horizontal Microfin Tubes, *Trans. of the JSRAE*, vol. 30, no. 4: p. 404-411. (in Japanese)

Kurose, K., Miyata, K., Hamamoto, Y., Mori, H., 2018, Characteristics of Flow Boiling Heat Transfer in Non-Uniformly Heated Parallel Mini-Channels, *Trans. of the JSRAE*, vol. 35, no. 2: p. 101-108. (in Japanese)

Lockhart, R.W., Martinelli, R.C., 1949, Proposed Correlation of Data for Isothermal Two-Phase, Two Component Flow in Pipe, *Chemical Engineering Progress*, vol. 45: p. 723-737.

Ohno, M., Enoki, K., Kanja, K., Nakamura, T., Okawa, T., Nishida, K., Kato, M., 2017, Elucidation of Flow Distribution of Two-Phase Flow in the Parallel Mini-Channel Evaporator, *Trans. of the JSRAE*, vol. 34, no. 4: p. 413-424. (in Japanese)

Ong, C.L., Thome, J.R., 2009, Flow Boiling Heat Transfer of R134a, R236fa and R245fa in a Horizontal 1.030 mm Circular Channel, *Experimental Thermal and Fluid Science*, vol. 33: p. 651-663.

Shiga, K., Yamakawa, N., Sugimoto, K., Asano, H., 2024, Evaporative Heat Transfer Characteristics by Heating with Heating Medium in Horizontal Multiport Tubes, *Proc. of the 11th Asian Conference on Refrigeration and Air Conditioning*: paper ID ACRA2024-B7-07.

Takamatsu, H., Momoki, S., Fujii, T., 1993, A Correlation for Forced Convective Boiling Heat Transfer of Non-Azeotropic Refrigerant Mixture of HCFC22/CFC114 in a Horizontal Smooth Tube, *International Journal of Heat and Mass Transfer*, vol. 36, no. 14: p. 3555-3563.

Watanabe, K., Jige, D., Inoue, N., 2016, Evaporation and Condensation Characteristics of Refrigerant Mixtures R245fa/R134a inside

Horizontal Tubes, *Trans. of the JSRAE*, vol. 33, no. 4: p. 383-395. (in Japanese)

6. Elucidation of Refrigerant Dissolution Behavior and Compatibility Evaluation of Refrigeration Oil in Compressors and Compression Characteristics of Low-GWP Mixed Refrigerants (Shizuoka University)

6.1 Overview of Research and Development

In recent years, the refrigeration and air-conditioning field has been strongly required to transition to low-global-warming-potential (GWP) refrigerants to counter global warming. In the refrigeration cycle, the refrigerant compressor plays a major role and accounts for a large proportion, approximately 70% to 80%, of the total power consumption of refrigeration and air-conditioning equipment; therefore, developing refrigerant compressors compatible with low-GWP refrigerants is essential to this transition. As a result of many years of technological development, Japan possesses world-class compressor technologies, and presenting compressor design guidelines for low-GWP compatibility is expected to enable a relatively swift transition.

To establish design guidelines for refrigerant compressors compatible with low-GWP refrigerants, the following issues related to compressor peripheral technologies need to be examined.

- Refrigeration oil in refrigerant compressors lubricates sliding parts, seals leakage paths, and cools compressor components; therefore, oil compatible with low-GWP refrigerants must be developed and evaluated. However, the dissolution behavior of refrigerants in refrigeration oil and the physical properties of refrigeration oil/refrigerant mixtures when low-GWP refrigerants are used remain insufficiently clarified in many respects.
- For practical application of refrigeration cycles using low-GWP refrigerants, oil-return characteristics must be evaluated. In actual compressor suction piping, an annular two-phase flow pattern forms, and many aspects remain unclear regarding the extent to which highly viscous refrigeration oil is transported by the refrigerant flow. Accordingly, oil-return characteristics must be evaluated by observing flow patterns and measuring temporal changes in oil-film thickness.
- Zeotropic mixed refrigerants are being considered as promising alternative candidates for low-GWP refrigerants. However, because the thermophysical properties of mixed refrigerants vary depending on the composition ratio, they may markedly affect compressor performance and loss characteristics. Therefore, a compressor prediction model that can predict compressor characteristics across compositions is needed.
- The low-GWP refrigerants currently being considered as alternative candidates tend to have lower volumetric refrigeration capacity than conventional refrigerants. Directly applying low-GWP refrigerants to existing compressors is expected to reduce refrigeration capacity. Accordingly, using low-GWP refrigerants requires either larger compressors or higher operating speeds; however, given market needs, increasing compressor speed is preferable to enlarging equipment. Meanwhile, the issues caused by high-speed operation remain unclear, and design guidelines suitable for such operation must be established through prototyping and evaluation.

As described above, ensuring the performance and reliability of refrigerant compressors using low-GWP mixed refrigerants requires developing and evaluating suitable refrigeration oils, understanding the dissolution characteristics of these refrigerants and oils, and clarifying their compression characteristics. Against this background, the research was conducted by dividing it into the following research items.

- Dissolution characteristics of refrigeration oil/refrigerant mixtures: solubility, physical-property measurement, and volume change
- Dissolution characteristics of refrigeration oil/refrigerant mixtures: dissolved components and solubility prediction

- Formulation of oil-return amount based on oil-film measurements in a vertical upward pipe
- Construction of a compressor-characteristics prediction model considering composition changes in mixed refrigerants and evaluation of applicability of alternative refrigerants
- Development of design guidelines for high-speed compressors using low-GWP refrigerants and testing of prototype compressors

From FY2023 to FY2025, tests were conducted on zeotropic mixed refrigerants that are currently readily available, and their basic characteristics and physical properties were clarified. In addition, for compressor development and practical application, compressor calculation models that incorporate these basic characteristics were constructed and model calculations were performed, compressor design guidelines were examined, and preparations for prototype compressor testing were advanced. The results, issues, and related matters for each research item are described in the following sections.

6.2 Solubility Characteristics of Refrigeration Oil/Refrigerant Mixtures: Solubility, Physical-Property Measurement, and Volume Change

6.2.1 Background and objectives

In refrigerant compressors, refrigeration oil is used to lubricate sliding parts, seal leakage paths, and cool compressor components. In refrigeration cycles, oils that are miscible with refrigerants are generally employed to ensure oil return after discharge from the compressor and to maintain compressor and cycle performance. Consequently, refrigerant dissolves in the oil inside the compressor, causing various physical properties to change according to the solubility. These changes directly affect phenomena and losses occurring in the cycle. For example, the viscosity of a refrigerant/refrigeration oil mixture affects compressor friction losses and oil return, the dielectric constant affects motor insulation, and surface tension affects foaming behavior in the compressor. Therefore, selecting refrigeration oil for a refrigeration cycle requires understanding both refrigerant solubility in the oil under various temperature and pressure conditions and the corresponding changes in mixture properties. In the low-GWP zeotropic mixed refrigerants targeted in this project, multiple pure refrigerants with different boiling points are blended, and their dissolution behavior may differ from that of pure refrigerants. Furthermore, the volume of a mixture formed by dissolving refrigerant in refrigeration oil is well known to be smaller than the sum of the individual volumes of the oil and refrigerant. Because this volume change is related to the density change of the refrigerant/refrigeration oil mixture, it hinders accurate measurement of viscosity and surface tension.

Accordingly, in this research item, solubility measurements were performed for mixtures of POE (polyol ester) or PVE (polyvinyl ether) oil with R454C and its constituent components, R32 and R1234yf, and the refractive index was measured as a representative physical property. The measurements were conducted at temperatures of 30–90 °C and refrigerant concentrations of 0–100%. In addition, the volume of each refrigerant/refrigeration oil mixture was measured, and the volume change due to mixing was investigated (Rakpakdee *et al*., 2024, 2025).

6.2.2 Experimental apparatus and method

A schematic of the experimental apparatus is shown in Figure 6.2-1. The test vessel is a cylindrical high-pressure-resistant vessel with a height of 55 mm and an inner diameter of 45 mm. To observe the inside of the test vessel, sight glasses were installed on the pressure vessel, and a light source was attached to one of them. A scale was attached to the inner wall of the vessel to measure the liquid level in the pressure vessel. The pressure vessel was covered with a heater and thermal insulation material, and temperature was controlled using a thermocouple installed inside the vessel and a PID controller. A pressure gauge was attached to the vessel's upper section, enabling *in-situ* pressure measurement during testing. A refractive-index sensor was also installed on the side of the vessel to measure the mixture’s refractive index. The refrigerant/refrigeration oil mixture was stirred using a magnetic stirrer, and the mixture mass was measured

by disconnecting the test vessel using a flare connector equipped with a service valve. Before charging the refrigerant into the pressure vessel, the mass of the refrigeration oil under vacuum was measured in advance, and the solubility could be calculated from these measurement results.

In this test, R454C, a zeotropic mixed refrigerant composed of R32, an HFC refrigerant, and R1234yf, an HFO refrigerant, was used. POE oil and PVE oil supplied by a domestic oil manufacturer were used as refrigeration oils.

6.2.3 Solubility and refractive index of refrigeration oil/refrigerant mixtures

(1) Method for calculating the solubility of zeotropic mixed refrigerants

Before charging the refrigerant into the test pressure vessel, the mass of the refrigeration oil (M_{oil}) is measured. Next, the refrigerant is charged into the test pressure vessel, and once the liquid level stabilizes, the mass of the mixture is measured. From this, the mass of the refrigerant (M_{ref}) is obtained, and the refrigerant mass fraction (Mf_{ref}) is given by the following equation.

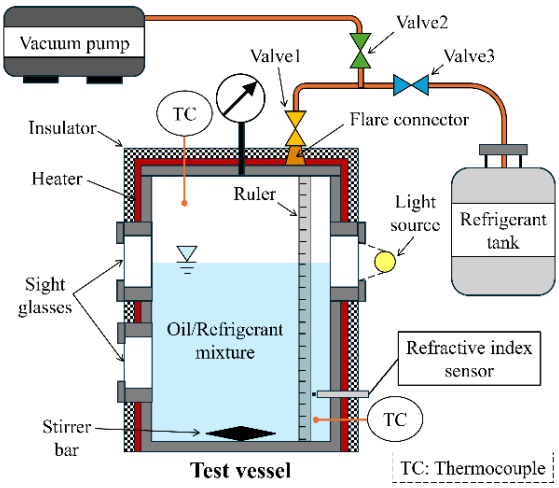

Figure 6.2-1 Experimental apparatus for solubility measurement

$$Mf_{ref} = \frac{M_{ref}}{M_{ref} + M_{oil}} \tag{6.2-1}$$

However, because the dew-point pressure and bubble-point pressure at a given temperature differ for zeotropic mixed refrigerants, it is suggested that vapor–liquid equilibrium is established in a state different from that of a pure refrigerant or an azeotropic mixed refrigerant in the pressure range above the dew-point pressure and below the bubble-point pressure, as well as in the supercritical state. Figure 6.2-2 shows a conceptual diagram of the mixing state in the test vessel under equilibrium conditions for a zeotropic mixed refrigerant. The components in the vessel are classified as refrigeration oil (Oil), refrigerant dissolved in the refrigeration oil (Ref(oil)), gas refrigerant (Ref(gas)), liquid refrigerant (Ref(liq)), and supercritical refrigerant (Ref(sc)); accordingly, the three equilibrium states shown in the figure can be considered. Figure 6.2-2(a) and (b) show states in which gas refrigerant and liquid refrigerant exist, at a quality corresponding to the pressure and temperature at that time, in the space other than that occupied by the refrigeration oil/refrigerant mixture, and the vertical relationship between the liquid refrigerant and this mixture differs depending on the density difference caused by temperature. Figure 6.2-2(c) shows the refrigerant in a supercritical state in the high-temperature region. Therefore, in addition to the solubility obtained using Equation (6.2-1), it is necessary to estimate the refrigerant concentration considering only the refrigerant dissolved in the refrigeration oil.

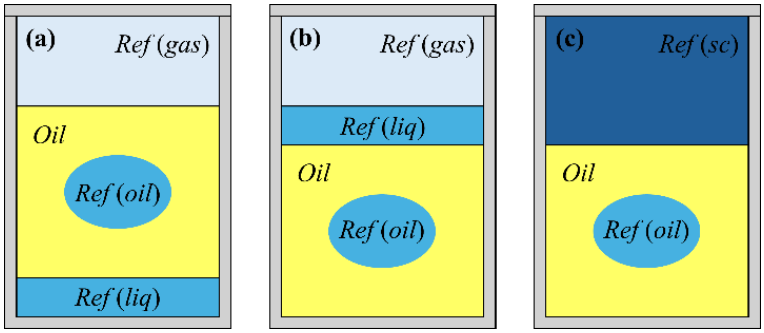

Figure 6.2-2 Conceptual diagram of mixing conditions in the test vessel

In this study, the system volume (V_{sys}) was determined in advance, and the masses of the refrigeration oil and refrigerant were measured using an electronic balance. Here, under the mixing conditions shown in Figure 6.2-2(a) and (b), the system volume is equal to the sum of the following individual volumes.

$$V_{sys} = \frac{M_{oil}}{\rho_{oil}} + \frac{M_{ref(gas)}}{\rho_{ref(gas)}} + \frac{M_{ref(liq)}}{\rho_{ref(liq)}} + \frac{M_{ref(oil)}}{\rho'_{ref(liq)}} \tag{6.2-2}$$

Here, M_{oil} and ρ_{oil}, $M_{ref(gas)}$ and $\rho_{ref(gas)}$, $M_{ref(liq)}$ and $\rho_{ref(liq)}$, $M_{ref(oil)}$ and $\rho'_{ref(liq)}$ are the mass and density of the refrigeration oil, gas refrigerant, liquid refrigerant, and liquid refrigerant in the refrigeration oil, respectively. The value of $\rho'_{ref(liq)}$ was estimated by linearly approximating the density data of the liquid refrigerant from 0–50 °C obtained from REFPROP ver.10.0 and extrapolated above 50 °C using the same approximation.

The mass of the refrigerant in the system at equilibrium is expressed as follows.

$$M_{ref} = M_{ref(gas)} + M_{ref(liq)} + M_{ref(oil)} \tag{6.2-3}$$

In addition, the quality in the space other than the refrigeration oil/refrigerant mixture in the system is expressed by the following equation.

$$X = \frac{M_{ref(gas)}}{M_{ref(gas)} + M_{ref(liq)}} \tag{6.2-4}$$

As the refrigerant quality in the pressure range from the dew-point pressure to the bubble-point pressure can also be obtained from REFPROP ver.10.0, the masses of the gas refrigerant, liquid refrigerant, and liquid refrigerant in the refrigeration oil can be estimated from Equations (6.2-2) to (6.2-4).

On the other hand, in the supercritical state, the system volume is equal to the sum of the following individual volumes.

$$V_{sys} = \frac{M_{oil}}{\rho_{oil}} + \frac{M_{ref(sc)}}{\rho_{ref(sc)}} + \frac{M_{ref(oil)}}{\rho'_{ref(liq)}} \tag{6.2-5}$$

Here, $M_{ref(sc)}$ and $\rho_{ref(sc)}$ are the mass and density of the refrigerant in the supercritical state, respectively. The mass of the refrigerant in the system is also expressed as follows.

$$M_{ref} = M_{ref(sc)} + M_{ref(oil)} \tag{6.2-6}$$

Therefore, the masses of the refrigerant in the supercritical state and the liquid refrigerant in the refrigeration oil can also be estimated from Equations (6.2-5) to (6.2-6). From the refrigerant mass calculated as described above, the refrigerant concentration (C_{ref}) of the refrigeration oil/refrigerant mixture for the zeotropic refrigerant can be determined using the following equation.

$$C_{ref} = \frac{M_{ref(oil)}}{M_{ref(oil)} + M_{oil}} \times 100\% \tag{6.2-7}$$

(2) Measurement results of solubility and refractive index

As an example of the refrigerant-solubility measurement results, the solubility of the POE/R454C mixture determined using Equation (6.2-1) is shown in Figure 6.2-3, and the refrigerant concentration determined using Equation (6.2-7), considering only the refrigerant dissolved in the refrigeration oil, is shown in Figure 6.2-4. These figures also show the dew-point and bubble-point pressures at each temperature, except at 90 °C, which is above the critical temperature. As shown in Figure 6.2-3, the pressure increased with increasing refrigerant mass fraction. Up to a mass fraction of approximately 0.5, the pressure increased steeply, whereas at mass fractions of approximately 0.5 or higher, the increase became gradual within the range between the dew-point and bubble-point pressures. The mass fraction at which the pressure increase became gradual shifted to larger values at higher temperatures and was approximately 0.4 at 30 °C. The refrigerant concentration in the refrigeration oil, calculated by considering only the refrigerant dissolved in the oil as shown in Figure 6.2-4, exhibited nearly the same trend, suggesting that the difference between the dew-point and bubble-point pressures of the zeotropic refrigerant has little effect on the solubility. At 30 °C and 50 °C, however, some data were missing in the high-concentration region. This is because, in this region, the refrigerant approaches a pure liquid state and the calculated mass of liquid refrigerant in the refrigeration oil became negative; thus, volume change must be considered in the calculation.

As an example of the refractive-index measurement results for the refrigeration oil/refrigerant mixture, Figure 6.2-5 shows the relationship between the refrigerant concentration and refractive index of the POE/R454C mixture, over the temperature range of 30 to 90 °C. The refractive index was measured at a position 10 cm above the bottom of the test vessel. As shown in the figure, at 30 °C, 50 °C, and 70 °C, the refractive index tended to decrease as the refrigerant concentration in the oil increased, and it decreased slightly with increasing temperature even at nearly the same concentration. At 90 °C, however, the refractive index changed little at refrigerant concentrations of 60% or higher, which is considered to be due to phase separation, resulting in no change in density (Rakpakdee *et al.*, 2024).

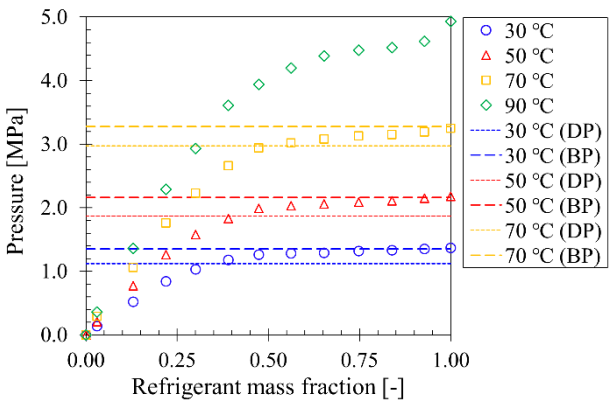

Figure 6.2-4

Refrigerant mass fraction of POE/R454C mixture calculated by Equation (6.2-1)

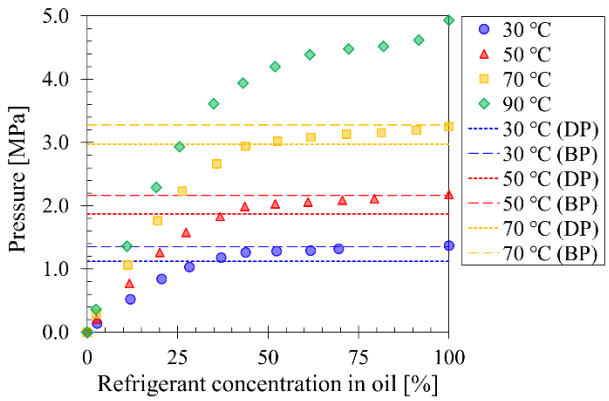

Figure 6.2-3

Refrigerant mass fraction of POE/R454C mixture calculated by Equation (6.2-7)

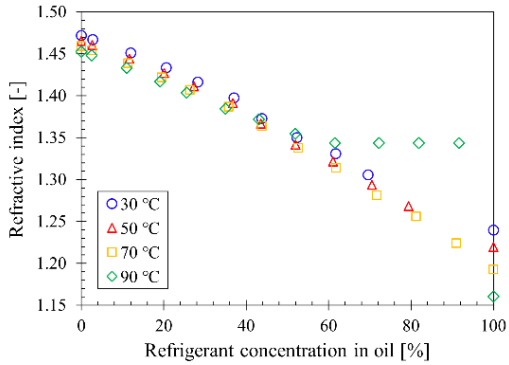

Figure 6.2-5 Refractive index of POE/R454C mixture depending on the refrigerant concentration in oil

6.2.4 Volume change associated with refrigerant dissolution in refrigeration oil

(1) Method for calculating volume change

When refrigerant dissolves in refrigeration oil, the mixture's volume becomes smaller than the sum of the oil and liquid refrigerant volumes. Figure 6.2-6 shows a conceptual diagram of the volume change. The volume change of the refrigeration oil/refrigerant mixture can be represented by the relationship shown in Figure 6.2-6(a) and (b). In Figure 6.2-6(a), the volume of the mixture (V_{calc}) can be calculated from the mass and density of the refrigeration oil and liquid refrigerant, respectively, using the following equation.

$$V_{calc} = \frac{M_{oil}}{\rho_{oil}} + \frac{M_{ref(liq)}}{\rho_{ref(liq)}} \tag{6.2-8}$$

Here, the density of the liquid refrigerant in the refrigeration oil was estimated using the same method as that described in Section 6.2.3(1). On the other hand, the volume actually obtained by measurement (V_{meas}) is as shown in Figure 6.2-6(b), and as shown in Figure 6.2-6(c) in the supercritical state; therefore, it is smaller than V_{calc} calculated using Equation (6.2-8). Accordingly, the ratio of these volumes is expressed as α by the following equation.

$$\alpha = \frac{V_{meas}}{V_{calc}} \tag{6.2-9}$$

Based on these calculations, the volume ratio α was evaluated by comparing the calculated volume with the measured volume.

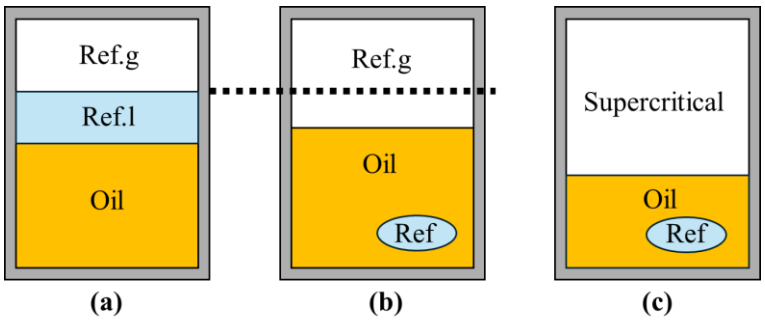

Figure 6.2-6 Conceptual model of volume change of the refrigeration oil/refrigerant mixture

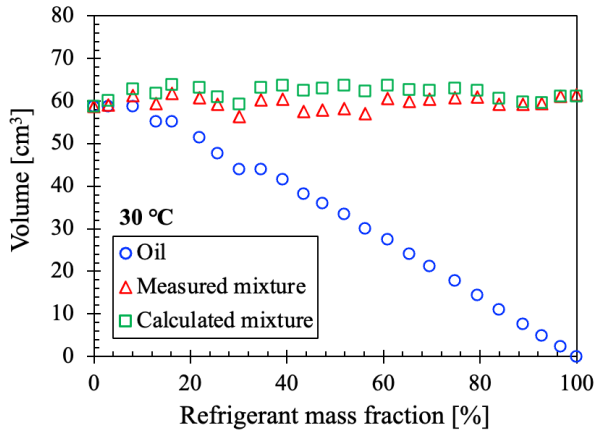

Figure 6.2-8

Comparison of mixture volume of POE / R454C mixture at 30 °C

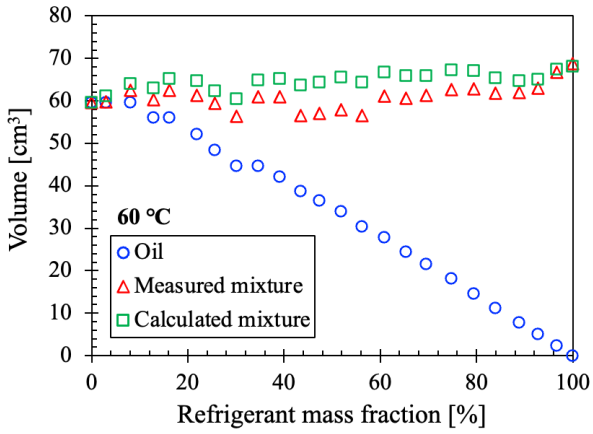

Figure 6.2-7

Comparison of mixture volume of POE / R454C mixture at 60 °C

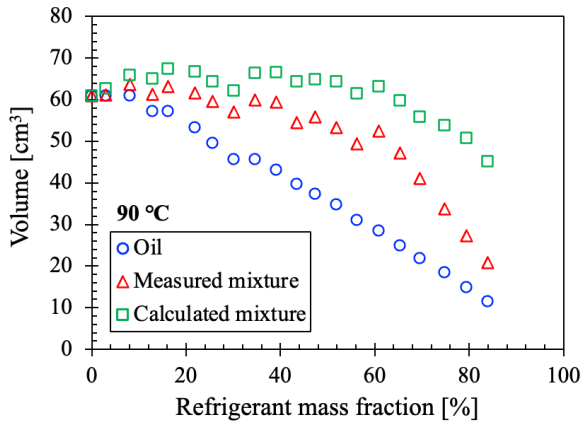

Figure 6.2-10

Comparison of mixture volume of POE / R454C mixture at 90 °C

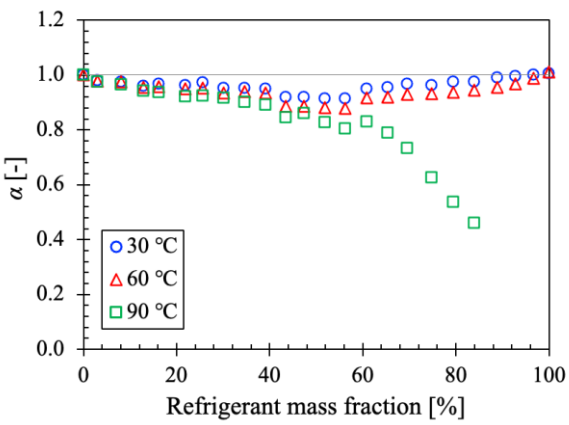

Figure 6.2-9

Volume difference rate α between measured volume and calculated one

(2) Measured volume and volume change

As an example of the volume measurement results for the refrigeration oil/refrigerant mixture, the volumes of the POE/R454C mixture at 30 °C, 60 °C, and 90 °C are shown in Figures 6.2-7, 6.2-8, and 6.2-9, respectively. The horizontal axis represents the refrigerant mass fraction [%], and the vertical axis represents the mixture volume [cm^3].

At 30 °C, as shown in Figure 6.2-7, when refrigerant dissolved in the refrigeration oil, the measured volume of the mixture became smaller than the calculated volume as the mass fraction increased. The difference was largest at a mass fraction of approximately 50%, where the masses of the refrigerant and refrigeration oil were nearly equal, and then decreased as the mass fraction further increased. This volume change is considered to occur because, when the refrigerant dissolves in the refrigeration oil, the smaller refrigerant molecules enter the spaces between the larger oil molecules. At 60 °C, as shown in Figure 6.2-8, almost the same tendency as that observed at 30 °C was obtained, and the difference between the measured mixture volume and the calculated volume was slightly larger than that at 30 °C. At 90 °C, as shown in Figure 6.2-9, the same tendency as that at 30 °C and 60 °C was observed up to a mass fraction of approximately 50%; however, at higher mass fractions, the volume decreased sharply. As 90 °C corresponds to a

supercritical state and liquid refrigerant is absent, the volume of the refrigeration oil is considered to have become dominant in the high-mass-fraction region where the amount of refrigerant was large.

Figure 6.2-10 shows the relationship between the volume ratio α and the refrigerant mass fraction. As shown in the figure, the value of α was smallest when the mass fraction was approximately 50% and decreased slightly with increasing temperature. These results indicate that, when the refrigerant and refrigeration oil had nearly equal masses and the temperature was higher, the volume decreased during mixing compared with the total liquid volume of the pure refrigerant and oil before mixing. Furthermore, in the supercritical state at 90 °C, it was found that the value of α also decreased sharply at mass fractions of 50% or higher (Rakpakdee *et al*., 2025).

6.3 Solubility Characteristics of Refrigeration Oil/Refrigerant Mixtures: Dissolved Components and Solubility Prediction

6.3.1 Background and objectives

In refrigerant compressors, refrigeration oils that are miscible with refrigerants are generally used. On the other hand, when zeotropic mixed refrigerants such as those targeted in this research project are used, each component may exhibit different dissolution characteristics in refrigeration oil as the zeotropic mixed refrigerants consist of multiple pure refrigerants with different boiling points. In fact, for zeotropic mixed refrigerants containing HFO refrigerants that are being examined as alternative candidates, Inoue *et al*. (2024) reported how the composition mass ratio of each dissolved component changes with temperature and pressure, as a dissolution characteristic of R474A in PVE oil. However, reports on such dissolved compositions are limited, and the dissolved composition has not yet been sufficiently evaluated for various zeotropic mixed refrigerants.

Accordingly, in this research item, the selective dissolution of each component of a mixed refrigerant into refrigeration oil was experimentally clarified as a dissolution characteristic of zeotropic mixed refrigerants containing HFO refrigerant. In addition, based on the obtained experimental results, a calculation method for predicting refrigerant solubility was examined (Ariga *et al*., 2024).

6.3.2 Experimental apparatus and method

In this test, refrigeration oil/refrigerant mixtures were prepared at various solubilities, and the liquid phase of each mixture was sampled. The refrigerant dissolved in the refrigeration oil was then separated from the sampled solution and recovered. The composition of this dissolved refrigerant was measured by gas chromatography using the absolute calibration method. At the same time, the refrigerant solubility of the sampled refrigeration oil/refrigerant mixture was calculated from the mass change of the sampling vessel before and after refrigerant separation.

Figure 6.3-1 shows a schematic of the cylindrical pressure vessel used to prepare and sample the refrigeration oil/refrigerant mixture, with an inner diameter of 40 mm and a height of 60 mm. To enable observation of the inside of the test vessel, two glass windows with a diameter of 18 mm were installed vertically at each of three locations on the side surface of the vessel. The mixture was stirred using a magnetic stirrer, and temperature control was performed using an electric heater wound directly around the test vessel. In this test, to minimize changes in the composition of the zeotropic mixed refrigerant during refrigerant charging, charging was performed through a double-ended cylinder in addition to the siphon tube installed in the zeotropic mixed refrigerant cylinder. Before each test, the refrigerant charged into the test vessel from the lower part of the double-ended cylinder was collected using a sampling bag, and the refrigerant composition during charging was measured in advance and treated as the reference composition.

Figure 6.3-2 shows a schematic of the apparatus used to separate and recover the dissolved refrigerant from the sampled mixture. The sampling vessel containing the mixture was connected to an oil-free vacuum pump through a filter, and a sampling bag was connected to the outlet of the oil-free vacuum pump. An electric heater was wound

directly around the sampling vessel, and the refrigerant dissolved in the refrigeration oil was separated and recovered using the electric heater and vacuum pump. After refrigerant separation, the refrigerant solubility of the sampled refrigeration oil/refrigerant mixture was calculated from the mass change of the sampling vessel. The mass change of the filter installed between the sampling vessel and the vacuum pump was also recorded, and the refrigerant solubility was calculated after correcting for any small amount of discharged refrigeration oil. The recovered refrigerant gas was injected into a gas chromatograph, and its composition was measured using the absolute calibration method.

In this test, R454C, a zeotropic mixed refrigerant composed of R32, an HFC refrigerant, and R1234yf, an HFO refrigerant, was used. POE oil and PVE oil supplied by a domestic oil manufacturer were used as refrigeration oils.

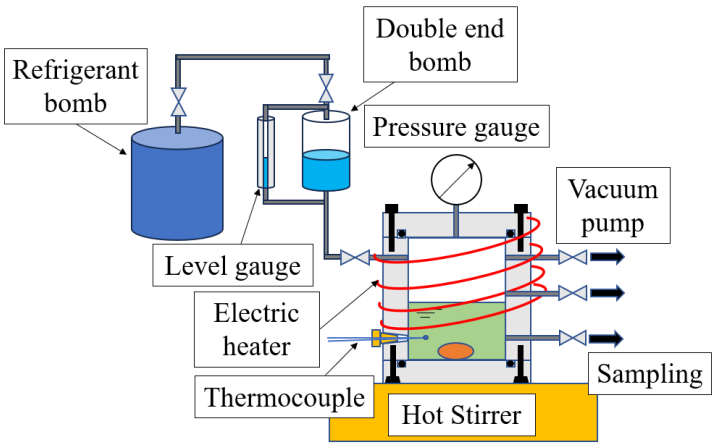

Figure 6.3-1 Pressure vessel for refrigerant and oil mixture

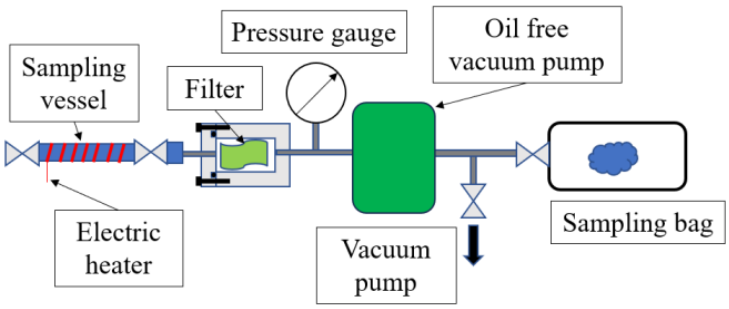

Figure 6.3-2 Refrigerant extraction system for separating refrigerant from the mixture in the sampling vessel

6.3.3 Dissolved composition of refrigeration oil/refrigerant mixtures under saturated dissolution conditions

As an example, the measurement results for the dissolved composition of the PVE/R454C mixture at liquid temperatures of 20 °C and 60 °C are shown in Figures 6.3-3 and 6.3-4, respectively. In these figures, the horizontal axis represents the refrigerant solubility [%], and the vertical axis represents the mass ratio [%] of each component in the liquid phase. The refrigerant composition during charging in each experiment and the range of refrigerant solubility above the dew-point pressure are also shown in the figures. As shown in Figure 6.3-3, at 20 °C, the dissolved composition nearly coincided with the charging composition, and selective dissolution did not occur. On the other hand, at 60 °C, as shown in Figure 6.3-4, the dissolved composition of R32 was slightly smaller than the charging composition at refrigerant mass fractions of 30–60%; thus, in this region, R1234yf exhibited greater selective solubility than R32. One possible reason for this is that a component with higher molecular polarity preferentially dissolves in the polar refrigeration oil. R32, an HFC refrigerant, consists only of saturated bonds, whereas R1234yf, an HFO refrigerant, has

unsaturated bonds and higher molecular polarity. As a result, R1234yf is considered to dissolve preferentially in the refrigeration oil compared with R32, thereby decreasing the relative mass ratio of R32 in the liquid phase. In addition, as R32 is a lower-boiling component than R1234yf and has higher volatility, it is more likely to transfer to the gas phase; therefore, a larger decrease in the mass ratio of R32 was observed at higher temperatures.

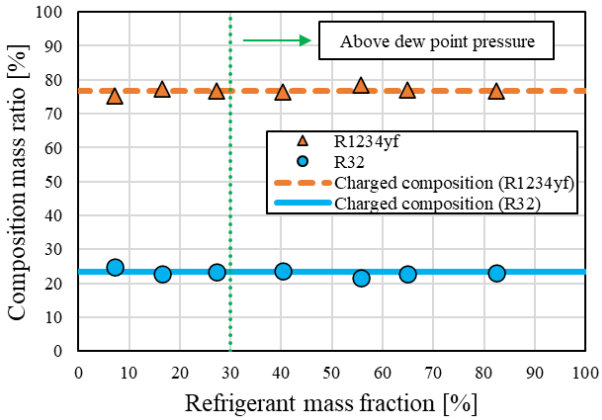

Figure 6.3-3
Dissolved composition at saturation (PVE/R454C, 20 °C, Charged composition R32: R1234yf = 23.3:76.7 [wt.%])

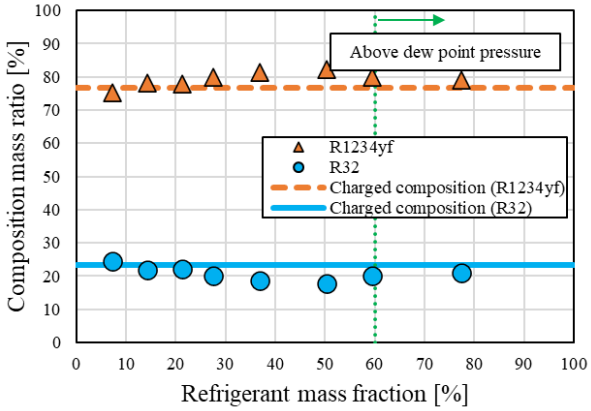

Figure 6.3-2
Dissolved composition at saturation (PVE/R454C, 60 °C, Charged composition R32: R1234yf = 23.2:76.8 [wt.%])

6.4 Formulation of Oil-Return Amount Based on Oil-Film Measurements in a Vertical Upward Pipe

6.4.1 Background and objectives

Developing and evaluating refrigeration oil for new refrigerants requires evaluating not only lubrication and sealing characteristics but also oil-return characteristics in piping. In compressor-inlet piping, an annular two-phase flow pattern forms, and it remains unclear how much of the highly viscous refrigeration oil is transported by refrigerant flow. In particular, refrigeration oil is expected to return with the greatest difficulty in vertical pipes, making its amount hard to predict. Accordingly, the flow pattern was observed by visualization, temporal changes in oil-film thickness were measured using a liquid-film sensor, and the measurement parameters required for prediction were examined.

6.4.2 Film-thickness measurement using a fiber-optic liquid-film sensor and prediction of the base liquid film

As one indicator for understanding refrigeration-oil transport in refrigeration-cycle piping, this study focused on liquid-film thickness. A fiber-optic liquid-film sensor was used, owing to its excellent environmental resistance, high temporal resolution, and ability to locally measure liquid-film thicknesses ranging from several hundred micrometers to several millimeters (Watanabe *et al*., 2024). This method exploits reflection caused by the difference in refractive index at the interface: light emitted from the fiber core toward the liquid film is reflected at the gas–liquid interface and returned to the core (return-light intensity). Liquid-film thickness was evaluated from this relationship, established in advance by calibration. This method offers higher accuracy for thinner films, since return-light intensity increases as the film thins.

In the experiment, liquid-film thickness was measured in a vertical upward pipe simulating a compressor suction pipe under room-temperature, atmospheric-pressure conditions, and a liquid-film-thickness model was evaluated as a first step toward predicting the transported flow rate. A schematic of the experimental apparatus and the fiber-optic

liquid-film sensor are shown in Figure 6.4-1. Gas was supplied as compressed air from a compressor and introduced vertically upward into the pipe through a flow meter. Liquid was supplied from a pressurized tank to the gas–liquid mixing section through a valve and a flow meter. In the gas–liquid mixing section, liquid permeated into the pipe through sintered metal, mixing with the upward-flowing gas to form annular flow. The total length of the apparatus was 900 mm, the section from the gas–liquid mixing section to the test-pipe outlet was 680 mm, and the inner diameter was 18 mm.

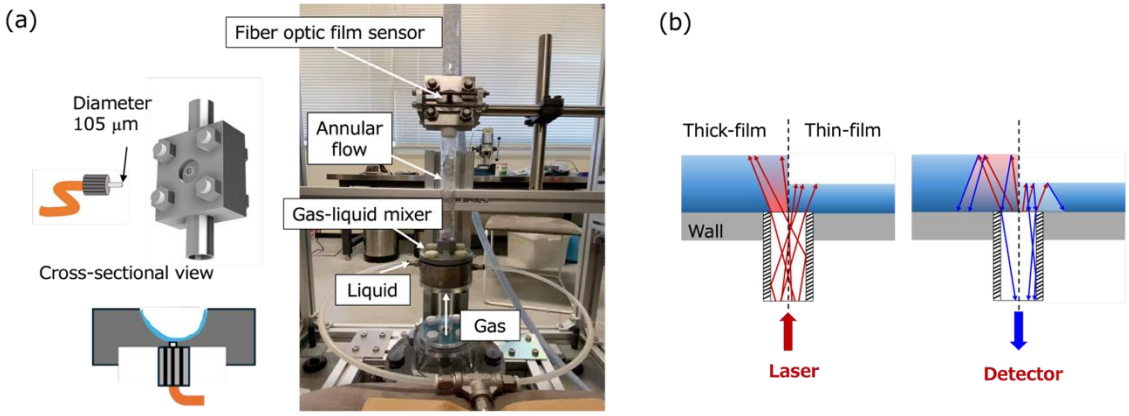

Figure 6.4-1 Schematic of the experimental setup: (a) observation system for annular flow forming a liquid film using a porous mixer; (b) measurement principle of the fiber-optic liquid film sensor, where the reflected light intensity varies with film thickness

In the experiments, liquid-film thickness was measured using water and two glycerol aqueous solutions with different viscosities, and the obtained results were examined. Inoue and Maeda (2021) derived Equation (6.4-1) as a theoretical expression for the liquid-film thickness formed by gas flow, assuming that the velocity distribution in the liquid phase is linear. Here, if the interfacial friction coefficient f can be determined, the liquid-film thickness can be predicted. They used the Blasius equation, which represents wall friction in turbulent flow ($f_b = 0.080Re_G^{1/2}$), as f.

$$h = \frac{2}{\sqrt{f}}\frac{\mu_L}{\mu_G}\sqrt{\frac{\rho_G}{\rho_L}}Re_L^{-\frac{1}{2}}Re_G^{-1}D \tag{6.4-1}$$

A comparison between the experimental and predicted results obtained using this equation is shown in Figure 6.4-2(a). The results indicate a large difference between the experimentally obtained average liquid-film thickness and the value predicted using the Blasius equation, which overestimated it. This result indicates that the gas–liquid interface has a larger friction coefficient than a turbulent wall surface. On the other hand, as shown in Figure 6.4-2(b), using the Wallis equation, Equation (6.4-2), enables accurate prediction of only the base liquid film obtained experimentally. In the low liquid-film Reynolds-number region, namely for highly viscous liquids, where the Blasius equation showed particularly large deviations, the base liquid-film thickness can be predicted from the present experimental results, and the amount of liquid transported by the base liquid film can also be estimated from the linear velocity distribution.

$$f = f_b\left(1 + 300\frac{t}{D}\right) \tag{6.4-2}$$

6.4.3 Transport mechanism of highly viscous liquids in annular flow

For air–water annular gas–liquid two-phase flow, a model has been proposed in which disturbance waves and droplets, in addition to the base liquid film, contribute to liquid transport (Le Corre, 2022). In this model, ripple waves generated on the base liquid film do not contribute to transport. On the other hand, disturbance waves are known not to occur in annular flow of highly viscous liquids, and droplet generation has been reported to become extremely limited (Wang *et al*., 2022). Under such conditions, the mechanism by which the liquid is transported remains unclear. Therefore, a device for separating liquid according to the momentum of the transported liquid was installed at the outlet of the annular-flow experimental apparatus, and the liquid-transport mechanism was examined.

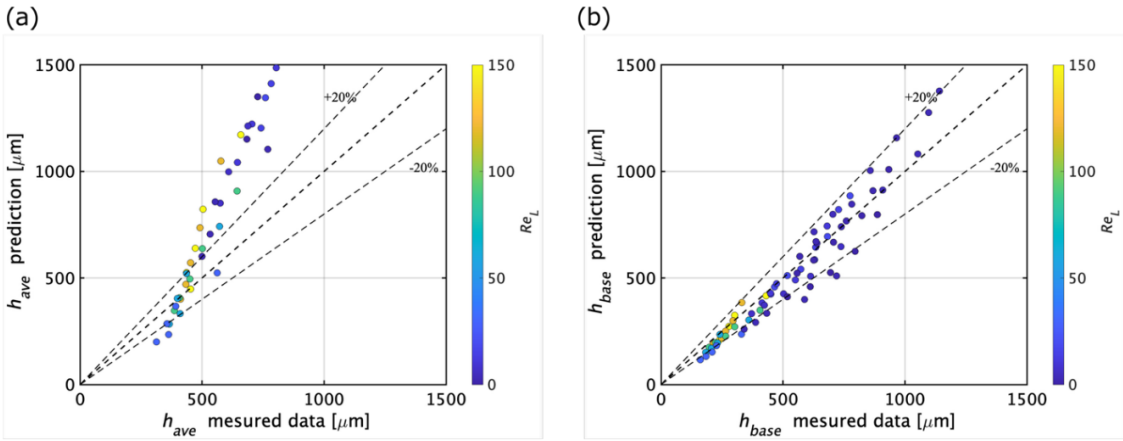

Figure 6.4-2 Comparison of measured liquid film thickness with model predictions: (a) average liquid film thickness calculated using the Blasius equation; (b) base liquid film thickness calculated using the Wallis equation

Figure 6.4-3 shows the liquid separation mechanism used to examine the transport mechanism of highly viscous liquid in annular two-phase flow. The figure shows a cross-sectional view of the separation mechanism and the state of liquid separation. In this separation mechanism, a plate with a central hole separated the liquid transported at the pipe outlet into three components, with the flow rate of each measured. At Outlet 1, liquid transported as droplets with the highest momentum was recovered. At Outlet 2, liquid transported by waves generated unsteadily was recovered. As shown in the visualization image in the figure, a large liquid film formed at the outlet and scattered outward; this scattered liquid was collected. By contrast, at Outlet 3, liquid flowing along the wall without large inertia was recovered. Therefore, it was assumed that the liquid transported by waves was measured at Outlet 2, whereas the liquid transported by the base liquid film was measured at Outlet 3.

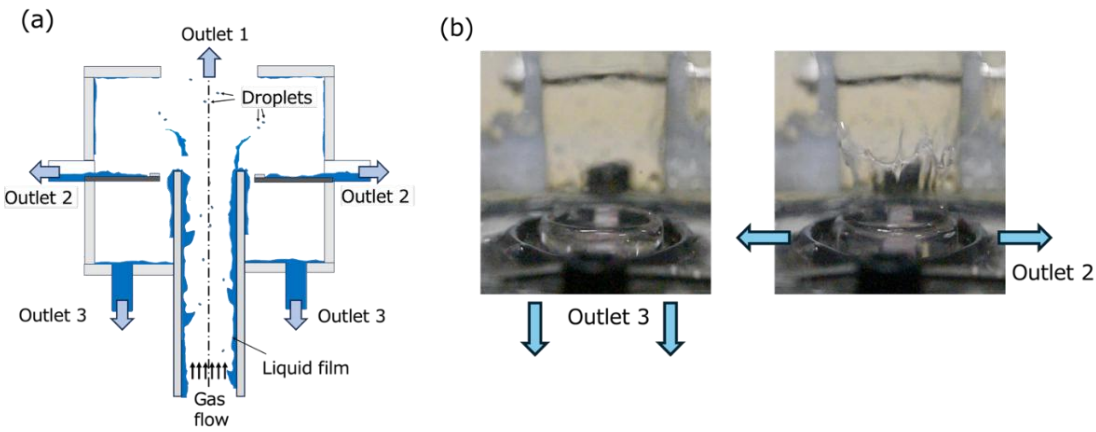

Figure 6.4-3 Liquid separation apparatus at the pipe outlet: (a) cross-sectional view of the separation system; (b) base liquid film discharged at Outlet 3 (left) and unsteady ejection of the liquid film at Outlet 2 (right)

Figure 6.4-4 shows the flow rates at each outlet measured using the separation mechanism. The vertical axis represents the amount of liquid recovered, the horizontal axis represents the supplied liquid flow rate, and the color map represents the gas Reynolds number. The circular plot symbols indicate the recovered flow rate at Outlet 1, assumed to be transported by waves, whereas the diamond symbols indicate the recovered liquid amount at Outlet 3, assumed to be transported by the base liquid film. The graph shows that, regardless of liquid viscosity, the recovered liquid at Outlet 1 tended to increase in proportion to the supplied flow rate. By contrast, the recovered liquid at Outlet 3 tended to asymptotically approach a certain constant value. These results suggest the existence of a limiting value, determined by the gas flow rate in the pipe, for liquid transport by the base liquid film; the surplus flow rate exceeding this limit was inferred to be transported by surface waves. As the base-liquid-film transport amount can be predicted from the liquid-film thickness, future work will aim to predict wave-transported liquid from data such as wave velocity, occurrence frequency, and wave height, and to formulate the oil-return amount according to refrigerant flow rate and piping dimensions.

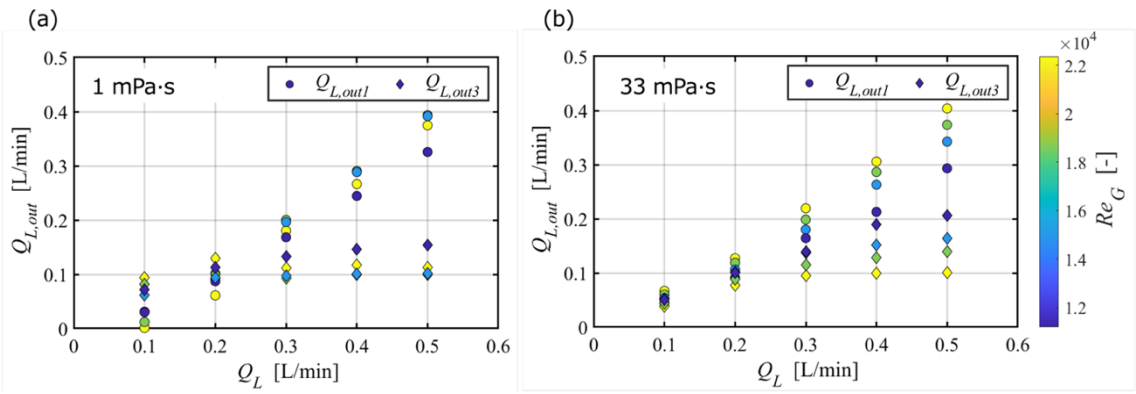

Figure 6.4-4 Liquid flow rates collected at outlets 2 (transported by the base liquid film) and 3 (by wave-induced liquid): (a) water (1 mPa·s); (b) viscous liquid (glycerin solution, 33 mPa·s)

6.5 Construction of a Compressor-Characteristics Prediction Model Considering Composition Changes in Mixed Refrigerants and Evaluation of Applicability of Alternative Refrigerants

6.5.1 Background and objectives

In recent years, from the perspective of mitigating global warming, the air-conditioning and refrigeration fields have been required to transition to low-GWP refrigerants. Mixed refrigerants composed of R32, R1234yf, and other components are being considered as promising alternative candidates to replace refrigerants that have been widely used conventionally. However, as the thermophysical properties of mixed refrigerants vary depending on their composition ratio, they may substantially affect compressor performance and loss characteristics. Against this background, the objective of this study is to construct a compressor-characteristics prediction model that can account for changes in the composition of mixed refrigerants. Specifically, a model is developed to predict discharge refrigerant temperature, compressor power, and refrigerant flow rate using suction refrigerant pressure, suction refrigerant temperature, and discharge refrigerant pressure as inputs. In addition, by considering various losses such as flow-rate losses and mechanical losses, the model aims to reproduce behavior closer to that of an actual machine. Furthermore, using this model, changes in compressor characteristics and losses associated with variations in the composition ratio of R32/R1234yf mixed refrigerant are evaluated, to obtain fundamental knowledge for compressor design suitable for alternative mixed refrigerants.

6.5.2 Construction of the compressor-characteristics prediction model

Figure 6.5-1 shows an overview of the compressor-characteristics prediction model. In this study, a quasi-steady model was constructed for a rotary compressor, taking into account energy transfer and various losses in the suction, compression, and discharge processes. The model inputs were the suction pressure P_s, suction temperature T_s, discharge pressure P_d, and ambient temperature T_{env}, and the outputs were the compressor power L, refrigerant mass flow rate G_r heat loss to the ambient air Q_{env}, and the amounts of various losses. The energy balance, including enthalpy transfer associated with refrigerant inflow and outflow, input power to the compressor, and heat dissipation to the ambient air, is expressed by the following equation.

$$G_r \cdot h_s + L = G_r \cdot h_d + Q_{env} \tag{6.5-1}$$

Here, h_s and h_d are the specific enthalpies at the suction and discharge states, respectively.

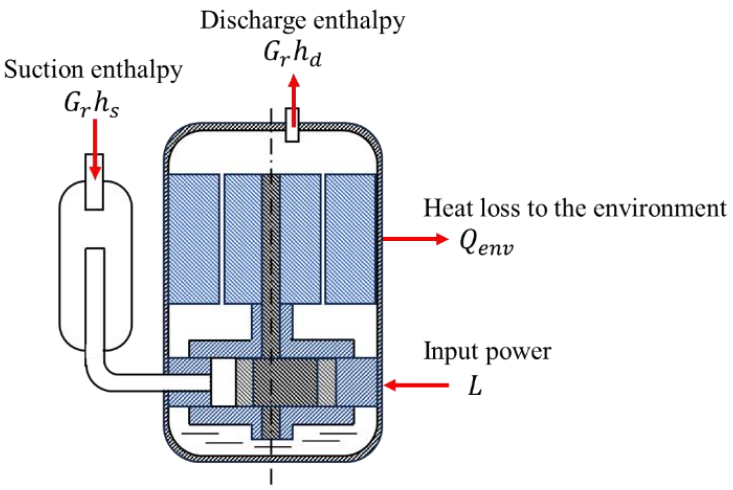

Figure 6.5-1 Energy balance model of the rotary compressor

(1) Refrigerant flow-rate model

The refrigerant flow rate G_r is obtained by subtracting various flow-rate losses from the theoretical flow rate G_0, which is based on the suction density ρ_s, displacement volume V_s, and rotational speed N.

$$G_0 = \rho_s \cdot V_s \cdot N \tag{6.5-2}$$

$$G_r = G_0 - \left(\Delta G_l + \Delta G_q\right) \tag{6.5-3}$$

Here, ΔG_l is the leakage flow-rate loss, and ΔG_q is the flow-rate loss associated with suction heating.
The leakage flow-rate loss is evaluated using the following equation by treating blow-through flow from the compression chamber as quasi-steady compressible flow.

$$\Delta G_l = \rho_l u_l A_l = A_l \sqrt{\frac{\kappa}{\kappa - 1} P_d \rho_d \left[\left(\frac{P_d}{P_s}\right)^{\frac{2}{\kappa}} - \left(\frac{P_d}{P_s}\right)^{\frac{\kappa-1}{\kappa}}\right]} \tag{6.5-4}$$

In addition, the superheating flow-rate loss is evaluated as a decrease in density caused by the temperature rise during the suction process and is expressed as follows.

$$\Delta G_q = \frac{\Delta T_s}{T_s} G_0 \tag{6.5-5}$$

Here, the suction temperature rise ΔT_s is estimated by the following equation based on heat transfer in the suction pipe.

$$\Delta T_s = \frac{Q_s}{G_0 c_{p,s}} = \frac{\alpha_s (T_w - T_s)}{G_0 c_{p,s}} \approx \frac{\alpha_s (T_d - T_s)}{G_0 c_{p,s}} \tag{6.5-6}$$

(2) Compression power model

The compressor power is evaluated by adding various power losses to the ideal power L_{ad} assuming isentropic compression.

$$L_{ad} = G_r (h_{d0} - h_s) \tag{6.5-7}$$

Here, h_{d0} is the discharge specific enthalpy after isentropic compression.
The actual shaft power L_{sh} is obtained by adding the indicated loss ΔL_{in}, leakage loss ΔL_l, and mechanical loss ΔL_{me}.

$$L_{sh} = L_{ad} + (\Delta L_{in} + \Delta L_l + \Delta L_{me}) \tag{6.5-8}$$

Furthermore, the input power L is obtained by considering the motor efficiency η_{mt}as follows.

$$L = L_{sh} / \eta_{mt} \tag{6.5-9}$$

The indicated loss ΔL_{in} is evaluated by geometrically approximating the difference between the $P - V$ diagrams of the ideal cycle and the actual cycle. In addition, the leakage loss and mechanical loss are estimated as follows.

$$\Delta L_l = \Delta G_l (h_{d0} - h_s)/2 \tag{6.5-10}$$

$$\Delta L_{me} = c_f F U = c_f \cdot A_f (P_d - P_s) \cdot 2\pi R_{sh} N \tag{6.5-11}$$

(3) Performance indices

Using the present model, the volumetric efficiency η_v and the total efficiency η_t are defined as follows.

$$\eta_v = G_r / G_0 \tag{6.5-12}$$

$$\eta_t = L_{ad}/L \tag{6.5-13}$$

6.5.3 Validation of the prediction accuracy of the compressor model

To confirm the validity of the present model, a comparison was made with measured data obtained using R22 as the refrigerant (Yanagisawa *et al.*, 1990). The comparison covered the refrigerant mass flow rate, compressor power, volumetric efficiency, and total efficiency, and the corresponding results are shown in Figure 6.5-2(a)–(d). Test conditions were as follows: suction pressure $P_s = 0.498 - 0.681$ [MPa], suction temperature $T_s = 0 - 10$ [°C], discharge pressure $P_d = 1.53 - 2.42$ [MPa], ambient temperature $T_{env} = 35$ [°C], and rotational speed $N = 3450$ [rpm]. The figures confirm that, for all evaluation quantities, the calculated values and measured values generally agreed within ±10%. In particular, the refrigerant flow rate and volumetric efficiency showed good agreement over a wide range of operating conditions, indicating that the present model can appropriately reproduce the basic characteristics of the compressor. On the other hand, slightly larger errors were observed for compressor power and total efficiency, which may be attributable to simplifications in the power-loss model. Accordingly, further improvement of the accuracy of these loss models should be examined in future work.

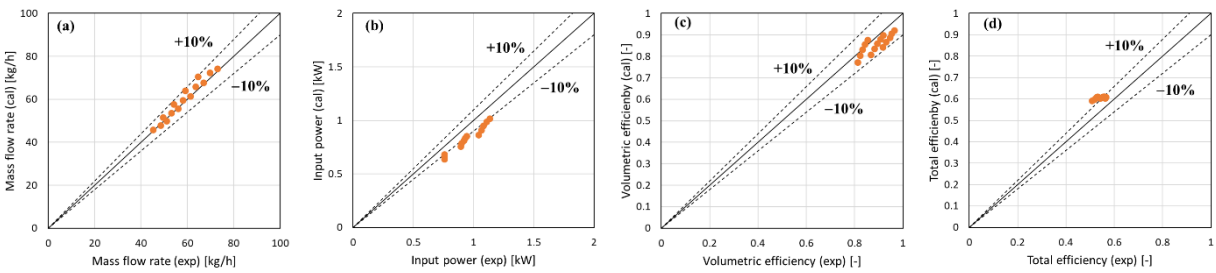

Figure 6.5-2 Validation of the proposed model by comparison with experimental data:
(a) refrigerant mass flow rate, (b) input power, (c) volumetric efficiency, and (d) total efficiency

6.5.4 Prediction of compressor characteristics associated with composition changes in R32/R1234yf mixed refrigerant

Figures 6.5-3 to 6.5-6 show the refrigerant mass flow rate, compressor power, volumetric efficiency, and total efficiency when the composition ratio of the R32/R1234yf mixed refrigerant was varied. The values of each loss are also shown in the graphs of refrigerant flow rate and compressor power. The analysis conditions were $P_s = 0.454$ [MPa], $T_s = 10$ [°C], $P_d = 2.37$ [MPa], $T_{env} = 35$ [°C], and $N = 3450$ [rpm]. The thermodynamic properties of the refrigerant were calculated using REFPROP ver.10.

As shown in Figure 6.5-3, the refrigerant flow rate decreased monotonically with increasing mass fraction of R32 (hereinafter referred to as the R32 fraction), and the volumetric efficiency shown in Figure 6.5-5 decreased in the same manner. This decrease is considered to be dominated by the reduction in suction density associated with the increase in the R32 fraction. Focusing on flow-rate losses, the suction-heating loss increased with increasing R32 fraction, whereas the change in leakage loss was extremely small. On the other hand, the compressor power shown in Figure 6.5-4 and the total efficiency shown in Figure 6.5-6 tended to decrease gradually with increasing R32 fraction. This is considered to result from the interaction between the increase in the enthalpy difference $h_{d0} - h_s$ in Equation (6.5-7) and the decrease in refrigerant flow rate G_r. The effect of composition change on indicated loss, leakage loss, and mechanical loss was almost negligible.

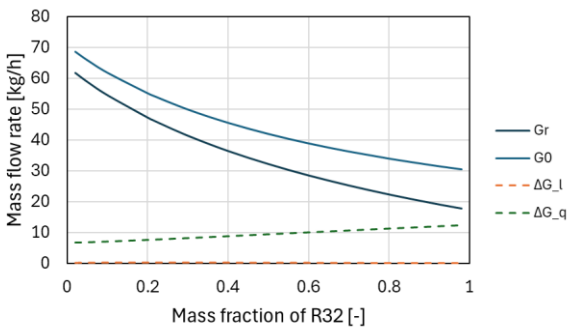

Figure 6.5-3 Mass flow rate vs. R32 mass fraction

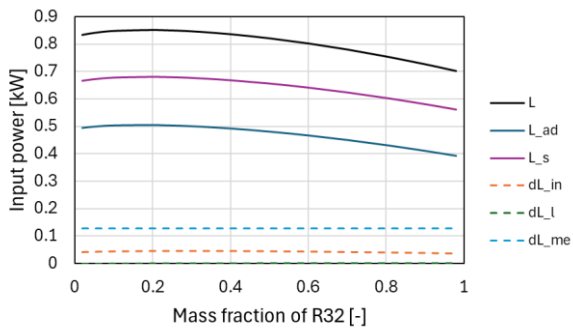

Figure 6.5-4 Input power vs. R32 mass fraction

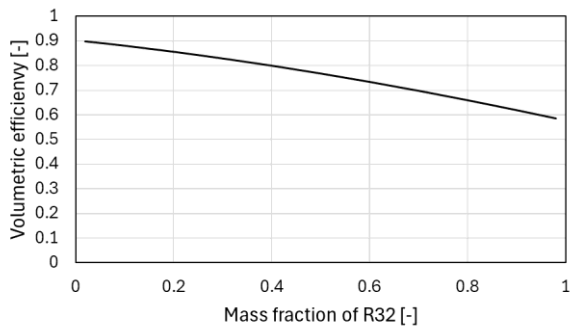

Figure 6.5-5 Volumetric efficiency vs. R32 mass fraction

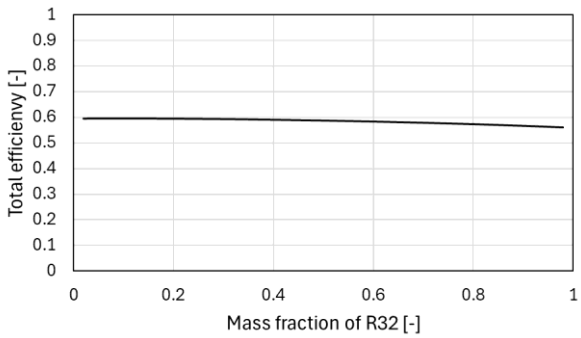

Figure 6.5-6 Total efficiency vs. R32 mass fraction

6.6 Development of Design Guidelines for High-Speed Compressors Using Low-GWP Refrigerants and Testing of Prototype Compressors

6.6.1 Background and objectives

Many low-GWP mixed refrigerants currently under consideration tend to have lower volumetric refrigeration capacity than conventional refrigerants (Domanski *et al*., 2017). Therefore, securing the required refrigeration capacity requires an increase in the refrigerant circulation rate processed by the compressor per unit time. Possible solutions include increasing the compressor size or increasing its operating speed; however, from a practical standpoint, increasing the compressor size conflicts with market demand. Accordingly, increasing compressor speed without enlarging the compressor is an effective approach for achieving refrigeration capacity equivalent to that of current refrigerants. However, high-speed compressor operation may increase friction losses at sliding parts in the compression elements and increase compression-power loss owing to the increased discharge volume per unit time. To address these issues, compressor improvements and weight reduction of compressor components may be required. This study therefore aims to realize high-speed compressor operation by applying lightweight composite materials currently being developed by Advance Composite Co., Ltd., a subcontractor in this project.

Accordingly, this research item targets rotary compressors and theoretically examines the loss factors that become pronounced with increased operating speed. Based on these results, points for compressor improvement are identified, and prototype compressors are fabricated. The prototype compressors are incorporated into a test refrigeration cycle and evaluated experimentally. The objective is to feed these results back into the next prototype compressor and establish compressor design guidelines.

6.6.2 Issues associated with increasing compressor speed and examination of countermeasures

The following three issues are identified as challenges associated with increasing the operating speed of rotary compressors. (1) Vane jumping, (2) Deflection of the rotating shaft, and (3) Increase in discharge loss. Details of each issue and possible countermeasures are described below.

(1) Prevention of vane jumping

In a rotary compressor, as the operating speed increases, the inertial force of the reciprocating vane becomes larger than the force pressing the vane against the rolling piston (hereinafter referred to as the piston) owing to the pressure difference, causing jumping in which the vane tip separates from the outer circumference of the piston. The following measures are effective for preventing vane jumping.

Measure 1: Reduction of vane mass

- Change the material from steel to an aluminum/ceramic composite material.
  → This can be achieved by applying the lightweight composite material developed by the subcontractor.
- Provide hollow sections, such as grooves or holes, within a range that does not impair the function of the vane.

Measure 2: Enhancement of vane pressing force

- Increase the spring constant of the vane spring.
  → This involves difficulties in the design of the pressing spring.
- Adopt a structure in which the pressure in the space behind the vane increases near top dead center.
  → This makes the mechanism complex and creates difficulties for practical application.

(2) Reduction of rotating-shaft deflection

In a rotary compressor, balance weights are required at the upper and lower parts of the motor rotor to dynamically balance the eccentric portion of the rotating shaft. During high-speed operation, these balance weights cause shaft deflection (bending), which leads to whirling at the upper end of the shaft and deterioration of motor performance. The following measures are effective for reducing rotating-shaft deflection.

Measure 1: Reduction of the eccentric mass of the rotating-shaft eccentric portion

- Reduce the mass of the piston that rotates together with the eccentric portion and the mass of the reciprocating vane.
  → This can be achieved by changing the piston and vane materials from steel to aluminum/ceramic composite materials developed by subcontractor.
- Reduce the weight of the shaft eccentric portion by partially hollowing the eccentric portion or replacing it with another lightweight component.

Measure 2: Adoption of a two-cylinder configuration at the rear of the compressor

- Compared with a single-cylinder configuration, the mass of the balance weights at the upper and lower ends of the rotor can be reduced, thereby suppressing deflection.

Measure 3: Review of balance-weight design

- Establish an optimal design method for the balance weights of rotary compressors.

(3) Reduction of discharge loss

As the rotational speed of a rotary compressor increases, the discharge volume per unit time, i.e., the discharge flow rate, increases. This results in increased pressure losses at the discharge port and discharge valve, thereby increasing compression-loss power. The following measures are effective for reducing discharge loss.

Measure 1: Enlargement of the discharge-port diameter

- An upper limit exists from the viewpoint of reed-valve strength (Hirayama *et al*., 2017).
- An optimal design that minimizes delayed closing and valve vibration is required.

Measure 2: Installation of discharge ports at two locations per cylinder

- By providing two discharge ports, the discharge flow rate per discharge valve is halved, reducing discharge-loss power.
- Install the second discharge valve on the partition plate between the two cylinders.
  → Although examples of implementation exist, the thickness of the partition plate increases, thereby increasing the distance between the shaft eccentric portions and requiring heavier balance weights.
- Install the second discharge valve at a location other than the partition plate.
  → As it is no longer necessary to increase the thickness of the partition plate, the distance between the two shaft eccentric portions does not increase, which is advantageous for balance-weight design.

6.6.3 Theoretical examination

The effects of various losses on overall efficiency were evaluated, including mechanical friction losses associated with increased compressor speed, such as vane-tip friction loss, vane-side friction loss, rolling-piston bearing friction loss, and main-bearing friction loss, as well as pressure loss at the discharge-valve section. The following describes the examination method and, as one representative result, the vane behavior during high-speed operation.

(1) Examination method

As the theoretical examination, performance calculations were conducted for a rotary compressor. The calculations consisted of piston-motion analysis, friction-loss calculations for each sliding part, and fluid-loss calculations coupled with motion analysis of the discharge valve (Yanagisawa, 1982). The calculations were performed considering the following points.

- Piston rotational motion: determined by an equation of motion based on the balance between the moment about the piston center and the moment of inertia of the piston.
- Piston bearing load: calculated from the resultant force of the gas compression load, rotational centrifugal force of the piston, and the normal and tangential forces at the contact point with the vane.
- Forces acting on the vane: the normal and friction forces at the contact point between the piston outer circumference and the vane tip; the normal and tangential forces at the contact point between the vane side surface and the cylinder vane slot wall; the force due to the pressure difference between the suction and compression chambers in the cylinder; the force due to the pressure difference between the inside and outside of the cylinder; the vane spring force; and the reciprocating inertial force of the vane.

Considering these factors, the rotational equation of motion of the piston (6.6-1) and the differential equations for the eccentricity and attitude angle of the shaft center at the piston bearing were solved simultaneously using the Euler method.

$$I_p \dot{\omega}_p = M_c - rF_t - M_b \tag{6.6-1}$$

Here, I_p is the moment of inertia of the piston, ω_p is the angular velocity about the piston center, M_c is the friction moment at the piston bearing, r is the piston radius, F_t is the tangential force at the contact point between the cylinder and the vane, and M_b is the friction moment at the piston end face. Based on the above, the vane-tip friction loss, vane-side friction loss, and piston-bearing friction loss were obtained. Meanwhile, to evaluate the fluid loss at the discharge-valve section, the discharge valve was modeled as a single-degree-of-freedom vibration system. By solving the equation of motion of the valve, considering the valve mass, elasticity, and damping coefficient, simultaneously with the pressure-change equation based on energy conservation in the cylinder, the valve lift and pressure variation in the compression chamber were calculated for each crank angle. The principal dimensions and operating conditions of the rotary compressor were set based on the literature (Yanagisawa, 1982), and R454C was used as the refrigerant.

(2) Vane behavior during high-speed operation

During high-speed compressor operation, the reciprocating inertial force of the vane increases, and vane jumping may occur, in which the vane tip separates from the outer circumferential surface of the piston. In such a case, a rapid decrease in volumetric efficiency owing to internal refrigerant leakage may occur, and reliability degradation caused by noise and impact loads when the vane recontacts the piston is also a concern. Figure 6.6-1 shows the normal force at the vane tip over a rotational-speed range of 50–250 rps. When this force becomes negative, the vane tip is judged to have separated from the outer circumferential surface of the piston. As shown in the figure, as the rotational speed increased, the amplitude of the normal force at the vane tip increased owing to the increase in the reciprocating inertial force of the vane. At 250 rps, the normal force at the vane tip became negative, indicating the occurrence of vane jumping, and it was found that approximately 200 rps is the limiting rotational speed at which vane jumping does not occur.

Furthermore, as a countermeasure against vane jumping in the high-speed region, a comparison was conducted assuming that the vane material was changed to lightweight, high-rigidity, and wear-resistant silicon nitride ceramics, thereby reducing the vane density from 7500 kg m^{-3} to 3200 kg m^{-3}. It was confirmed that changing the vane material increased the limiting rotational speed at which jumping begins. Even at 250 rps, the normal force at the vane tip did not become negative, indicating that a stable contact state could be maintained. This result demonstrates that reducing the material weight is an effective approach for preventing vane jumping in realizing high-speed compressor operation.

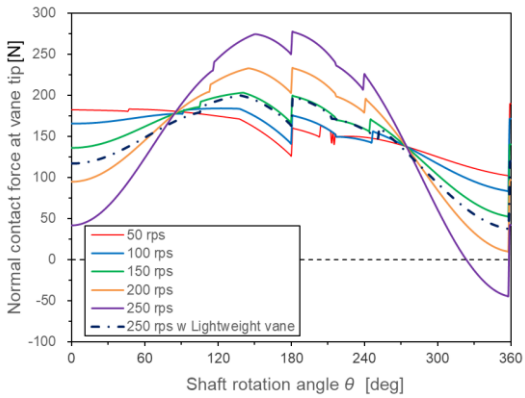

Figure 6.6-1 Normal contact force at vane tip

6.6.4 Prototype compressor fabrication and integration into the test refrigeration cycle

Based on the above examination results, fabrication of the prototype compressor ver.2025-1, satisfying the following requirements, was commissioned to a domestic compressor manufacturer using a 2.8 kW-class two-cylinder rotary compressor manufactured by the same company as the base model. In addition, fabrication of the vane and piston using lightweight components was commissioned to the subcontractor, Advance Composite Co., Ltd.

- Change to a motor capable of high-speed operation
- Application of lightweight components developed by the subcontractor to the vane and piston

Figure 6.6-2 shows the test refrigeration cycle to which the prototype compressor ver.2025-1 was connected, and Figure 6.6-3 shows the vane and piston fabricated from lightweight components. The following points are identified as major concerns, and they will be examined in detail through testing of the prototype compressor.

- Adjustment of bearing clearances and related parameters in accordance with high-speed operation is required.
- Optimal design of the motor and controller is required.

In future work, the performance of the prototype compressor ver.2025-1 during high-speed operation and the associated issues will be evaluated using the test refrigeration cycle, in addition to the points described above. The

effects of using lightweight components will also be verified. Based on the evaluation results, points for improvement will be examined and fed back to the next prototype unit.

Figure 6.6-3

Test refrigeration cycle with prototype compressor

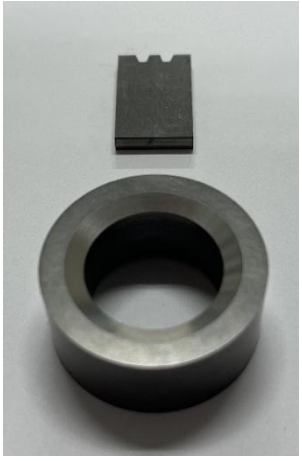

Figure 6.6-2

Vane and piston made from new material

References (Section 6)

Aruga, K., Rakpakdee, W., Fukuta, M., Motozawa, M., 2024, Measurement of Dissolved Components of Zeotropic Refrigerant Mixture in POE Oil, *Trans. of the JSRAE*, vol. 41, no. 4: p. 335-342. (in Japanese)

Domanski, P.A., Brignoli, R., Brown, J.S., Kazakov, A.F., McLinden, M.O., 2017, Low-GWP Refrigerants for Medium and High-Pressure Applications, *Int. J. Refrig.*, vol. 84: p. 198-209.

Hirayama, T., Aoki, T., Shida, S., Hatayama, M., Ferdhy Monasry, J., Okada, M., 2017, Study on Large Capacity and High Efficiency Rotary Compressor, *Trans. of the JSRAE*, vol. 34, no. 3: p. 261-271. (in Japanese)

Inoue, C., Maeda, I., 2021, On the Droplet Entrainment from Gas-Sheared Liquid Film, *Phys. Fluids*, vol. 33: 011705.

Inoue, T., Goto, T., Yamada, Y., 2024, Compositional Change Behavior of R1132(E) Refrigerant Mixture in the Presence of Refrigeration Oil—Compositional Change of R474A in the Presence of Refrigeration Oil PVE—, *Trans. of the JSRAE*, vol. 41, no. 4: p. 343-349. (in Japanese)

Le Corre, J.M., 2022, Phenomenological Model of Disturbance Waves in Annular Two-Phase Flow, *Int. J. Multiphase Flow*, vol. 151: 104057.

Lemmon, E.W., Huber, M.L., McLinden, M.O., NIST Standard Reference Database, REFPROP Ver. 10.0.

Rakpakdee, W., Fukuta, M., Motozawa, M., 2024, Mixing Behaviors of Refrigeration Oil and Zeotropic Refrigerant, *Proc. of 34th International Symposium on Transport Phenomena (ISTP34)*, Taoyuan.

Rakpakdee, W., Koarashi, T., Fukuta, M., Motozawa, M., 2025, Examination on Solubility and Volume Change of POE/R454C Mixture, *Proc. of JRAIA Symposium, International Symposium on New Refrigerants and Environmental Technology 2025*, Kobe.

Wang, Z., Liu, H., Zhang, Z., Sun, B., Zhang, J., Lou, W., 2022, Research on the Effects of Liquid Viscosity on Droplet Size in Vertical Gas–Liquid Annular Flows, *Chem. Eng. Sci.*, vol. 220: 115621.

Watanabe, S., Mizushima, Y., Sanada, T., 2024, Thin Liquid Film Thickness Measurement Using Stepped-Index-Type Optical Fiber Sensors, *J. Fluid Sci. Tech.*, vol. 19: JFST0007.

Yanagisawa, T., 1982, Piston Behavior and Mechanical Losses of the Rolling Piston Type Rotary Compressor: 1st Report, Experimental and Theoretical Analyses of Piston Behavior, *Trans. of the JSME. C.*, vol. 48, no. 429: p. 732-740. (in Japanese)

Yanagisawa, T., Fukuta, M., Suzuki, H., 1990, Mathematical Modeling of Transient Behavior of a Refrigerating Rotary Compressor, *Trans. of the JSME. B.*, vol. 56, no. 526: p. 1696-1701. (in Japanese)

7. Elucidation of Friction, Wear, and Lubrication Characteristics in Low-GWP Mixed-Refrigerant Atmospheres for Improving the Mechanical Efficiency of Compressors (Osaka Electro-Communication University)

7.1 Overview of Research and Development and Outcomes

When low-GWP mixed refrigerants are used, a reduction in overall system performance is unavoidable owing to their thermophysical characteristics. Therefore, maintaining and improving compressor performance requires an increase in compression capacity. This can be achieved either by enlarging the compressor or by increasing its operating speed to raise the compression amount per unit time. As there is also strong demand to avoid increasing compressor size, high-speed operation is required. Under such conditions, friction losses at the sliding parts of the mechanism must be minimized to maintain mechanical efficiency.

In this research and development item, friction characteristics in a low-GWP mixed-refrigerant atmosphere are clarified using the composite material developed in Machine C-3, to enable high-speed compressor operation. In particular, the friction, wear, and lubrication characteristics of the compressor mechanism, which are closely related to mechanical losses, are investigated in detail, and the results are used to develop design guidelines for high-performance compressors using the low-GWP mixed refrigerants examined in Machine C-1. This task targets rotary compressors, which are widely used in residential air conditioners. In collaboration with Machine C-1 and Machine C-3, the objective is to achieve an approximately 10% weight reduction relative to the current design while maintaining the same compressor capacity as current models.

In a rotary compressor, mechanical efficiency is affected by how smoothly the vane and cylinder groove, the vane and rolling piston, and the rolling piston and cylinder can slide against each other and how effectively they can roll. The friction forces and oil-film forces at each of these locations are measured experimentally to clarify the friction characteristics. Once the losses at the friction-generation sites are clarified, the mechanical efficiency can be calculated. These results will be incorporated into a compressor-efficiency calculation program and used to develop design guidelines for high-performance compressors.

7.2 Friction Characteristics of Rolling-Piston Rotary Compressors

7.2.1 Friction characteristics of rotary compressors

In a rolling-piston rotary compressor, as shown schematically in Figure 7.2-1, the rolling piston rotates along the inner wall of the cylinder. The mechanism is equivalent to a slider-crank mechanism in which the crank pin is enlarged and the connecting rod is eliminated. The tip of the slider is formed into an arc shape and is externally tangent to the rolling piston.

The rolling piston is not fixed to the crank pin and rotates independently of the crankshaft. A large discharge pressure acts on the back surface of the vane, pressing the vane tip against the rolling piston. At the vane tip indicated by (b) in Figure 7.2-1, both rolling and sliding occur. Furthermore, as the vane reciprocates in accordance with the motion of the rolling piston while suction and compression pressures act on its left and right sides, respectively, it tilts inside the cylinder groove, causing large friction at the contact point between the vane side surface and the groove, indicated by (a) in Figure 7.2-1.

In the theoretical treatment of compressor performance, it is important to accurately understand friction at sliding parts to clarify the motion of moving components. Rolling-piston friction and the resulting rotational behavior have been investigated both theoretically and experimentally by Okada and Hisayama (1975), Shimizu (1976), Slayton and

Hall (1982), Yanagisawa (1982a, b; 1983), Imaichi *et al*. (1983), Ishii *et al*. (1988, 1989), and others. In this study, the coefficient of friction when composite materials are used is experimentally clarified to help develop compressors operating at higher speeds than conventional models.

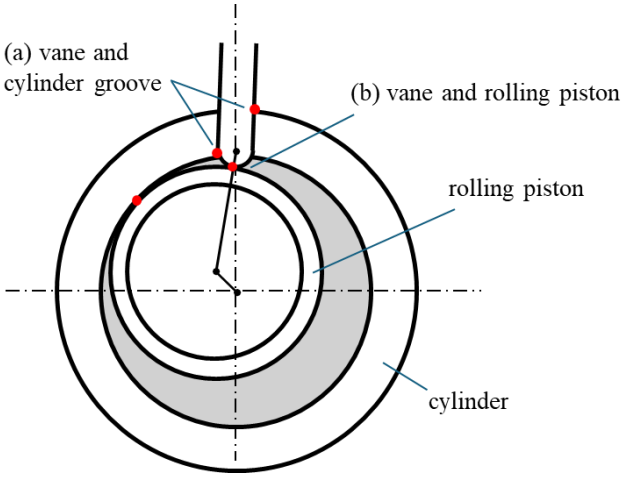

Figure 7.2-1 Schematic view of a rotary compressor and the contact points of its components

7.2.2 Friction characteristics between the vane and fixed groove

Suction pressure and compression pressure act on the two sides of the vane, respectively, and the back surface of the vane is constantly pressed against the rolling piston by a large discharge pressure. As the vane reciprocates under these conditions, it tilts inside the fixed groove, and large friction occurs between the vane side surface and the cylinder groove. To evaluate these friction characteristics when using the composite material developed in Machine C-3, a friction tester reproducing this sliding condition was fabricated, and measurements were taken in a refrigerant atmosphere.

Before starting the measurements, the friction, wear, and lubrication tester installed at Osaka Electro-Communication University was modified. As oil could not be circulated in the original pressure vessel during the experiment, an oil-circulation hole was added to its bottom flange. In addition, a pump for circulating refrigeration oil was newly installed.

The friction tester that reproduces the sliding condition between the vane and the cylinder groove is shown in Figure 7.2-2(a). To measure the friction force generated when the vane reciprocates while tilted and in contact with the edge of the fixed groove, the model shown in Figure 7.2-2(b) was fabricated. In this model, a flat-plate vane is supported while torque is applied to it, and a U-shaped groove sandwiching the vane is reciprocated.

The overall experimental apparatus is shown in Figure 7.2-3. As shown in Figure 7.2-2(b), the vane was suspended, and the U-shaped cylinder groove was installed on a slide guide. The slide guide was driven by converting the rotational motion of a motor into reciprocating motion through a Scotch-yoke mechanism. The stroke of the U-shaped groove was ±3 mm. The vane measured 55 mm wide, 36 mm high, and 5 mm thick; U-shaped grooves 5 mm wide and 18 mm long sandwiched it on either side. The contact height between the groove and the vane was 29 mm. A torque meter was installed above the vane. When the U-shaped groove reciprocates while torque is applied to the vane, friction is also supported at the vane suspension section. To avoid this, a linear-slide ball bearing was installed at the vane support section. Load cells installed on both sides of the vane measured the restraining forces at each end during reciprocation of the U-shaped groove, thereby detecting the generated friction force. The entire experimental apparatus was enclosed in a pressure vessel, and the experiments were conducted in a refrigerant atmosphere.

Experiments were conducted under environments of refrigerant R32 with POE oil (equivalent to VG68) and refrigerant R454C with PVE oil (equivalent to VG68). Under each environment, tests used vane/U-shaped-groove

combinations of cast iron/cast iron, composite/composite, and cast iron/composite. The motor was driven at 5–25 Hz. The reciprocating velocity v of the U-shaped groove was 0–0.47 m s^{-1}. A torque of approximately 6 Nm was applied to the vane, and oil was sprayed onto the sliding part at approximately 0.1 L min^{-1} during the experiment. The oil temperature inside the pressure vessel was approximately 20–40 °C. Owing to the characteristics of the experimental apparatus, the rotational speed was lower than that of an actual machine. Therefore, the oil temperature was set lower than that in an actual machine so that the viscosity was higher.

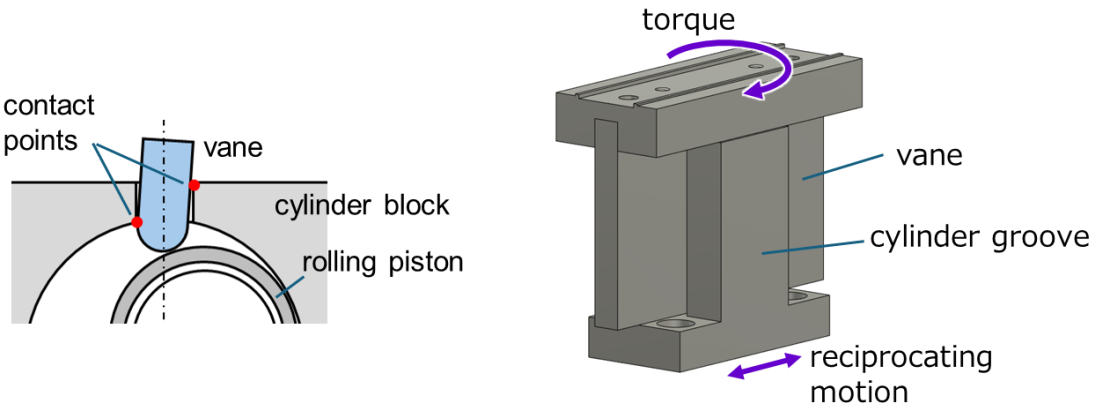

(a) Vane and cylinder groove (b) Experimental model

Figure 7.2-2 Experimental model of the vane and cylinder groove in a rotary compressor

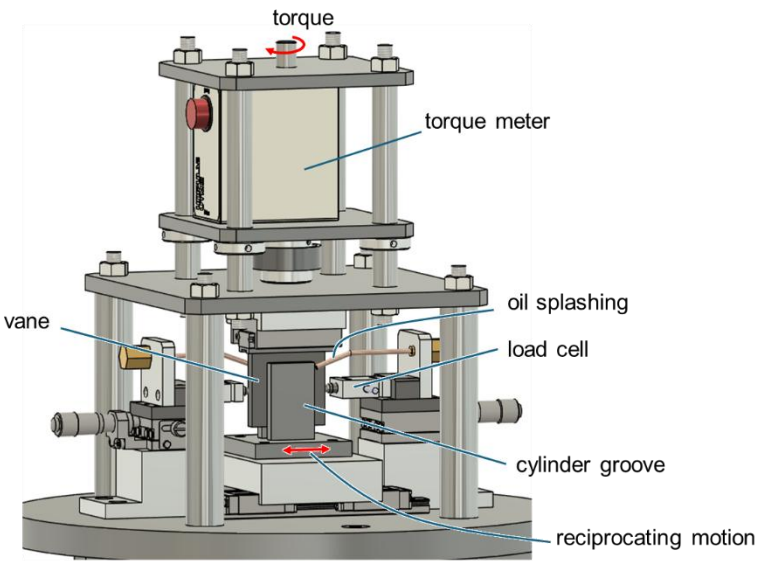

Figure 7.2-3 Experimental setup for friction measurements between the vane and cylinder groove of a rotary compressor

Figure 7.2-4 shows the coefficient of friction obtained by dividing the restraining forces measured by the left and right load cells by the pressing force between the vane and the U-shaped groove. Figure 7.2-4(a) shows the experimental results under the R32 environment, and Figure 7.2-4(b) shows those under the R454C environment. The horizontal axis represents the dimensionless bearing characteristic number expressed as $\eta v/P$. Here, η is the oil viscosity, and P is the average load per unit length. In both figures, the triangular symbols indicate the results for the cast iron/cast iron combination, the diamond symbols indicate those for the composite/composite combination, and the circular symbols

indicate those for the composite/cast iron combination. In either refrigerant environment, the coefficient of friction was almost constant when the horizontal-axis value was smaller than approximately 5×10^{-7}, and thereafter it tended to decrease gradually. The coefficient of friction was smallest for the cast iron/cast iron combination and was confirmed to increase slightly when composite materials were used. For composite combinations, the coefficient of friction tended to be slightly smaller for the composite/composite combination than for the composite/cast iron combination. Comparing the results under the R32 and R454C environments, no major difference owing to the refrigerant or oil was observed; however, the coefficient of friction tended to be slightly larger overall under the R454C environment.

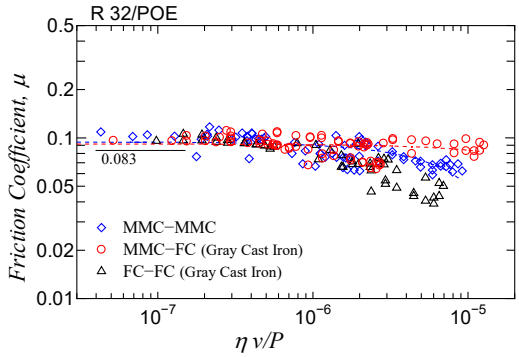

(a) For R32 and POE

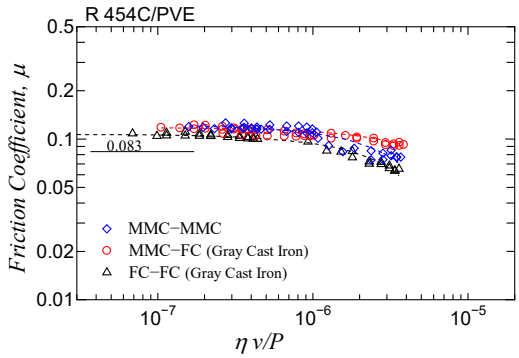

(b) For R454C and PVE

Figure 7.2-1 Experimental results for friction coefficient at vane and cylinder groove of rotary compressor

For the combination of a composite vane and a composite fixed groove, abnormal wear of the vane was observed during testing under the R454C environment. Analysis conducted in Machine C-3 (Advance Composite Co., Ltd.) confirmed the presence of ceramic agglomerates that served as the origin of the abnormal wear. It was also confirmed that the aluminum serving as the matrix of the composite material had slightly decreased. The present test results indicate that, when composite materials are used, particular attention must be paid during material fabrication to prevent such agglomeration.

7.2.3 Friction characteristics between the vane and rolling piston

The vane separating the suction chamber and compression chamber reciprocates vertically in accordance with the rotational motion of the rolling piston. The rolling piston is not fixed to the crank pin and rotates independently of the crankshaft. Accordingly, both rolling and sliding occur at the contact region between the vane tip and the freely rotating rolling piston.

To examine the friction characteristics between the vane and rolling piston when using the composite material

developed in Machine C-3, a friction tester reproducing this sliding condition was fabricated, and measurements were taken in a refrigerant atmosphere.

The vane tip has an arc-shaped profile and contacts the outer circumference of the cylindrical rolling piston. As shown in Figure 7.2-5(a), the vane tip and rolling piston come into contact somewhere along the two arcs. In this test apparatus, as shown in Figure 7.2-5(b), the rolling piston was reciprocated horizontally while a vane with a flat tip was pressed against it. The vane was fixed while a pressing force was applied to its back surface, and load cells were installed on both sides. A helical gear was used so that the crank pin made one revolution while the rolling piston completed one reciprocating cycle. A sliding bearing was provided between the crank pin and the rolling piston, allowing it to rotate freely. As the sliding state of the rolling piston changes depending on the pressing force applied by the vane, a target whose radius changes by 1 mm per revolution was attached to its upper end, and its motion was also measured. The overall test apparatus is shown in Figure 7.2-6. The rolling piston had an outer diameter of 44 mm, an inner diameter of 30 mm, and a height of 30 mm. The vane had a width of 12 mm, a length of 23 mm, and a height of 26 mm. The entire test apparatus was enclosed in a pressure vessel, and experiments were conducted in a refrigerant atmosphere.

The experiments were conducted under an environment of refrigerant R454C and PVE oil (equivalent to VG68). Tests used vane/rolling-piston combinations of cast iron/cast iron, composite/composite, and cast iron/composite. The pressing force on the back surface of the vane was varied from approximately 20 to 50 N, and the motor was driven at 5–20 Hz. The experiments were conducted while oil was supplied at approximately 0.1 L min^{-1} to the sliding parts between the crank pin and rolling piston and between the vane and rolling piston. The oil temperature inside the pressure vessel was approximately 20–40 °C.

When a cast-iron vane and rolling piston were combined, the contact point was confirmed to alternate irregularly between sliding and non-sliding states. Under conditions with substantial sliding, the rolling piston was found to move at almost the same speed as the crankshaft. Changes in the sliding state during an experiment under fixed conditions may have been affected by fluctuations in the oil supply rate and other factors. It is considered that a similar state also occurs during compressor operation and that the coefficient of friction constantly changes.

For both the composite vane/composite rolling piston and composite vane/cast-iron rolling piston combinations, the range of nearly rolling contact was confirmed to be wide. Even when the same amount of oil as that used for the cast iron/cast iron combination was supplied, the sliding velocity was relatively low.

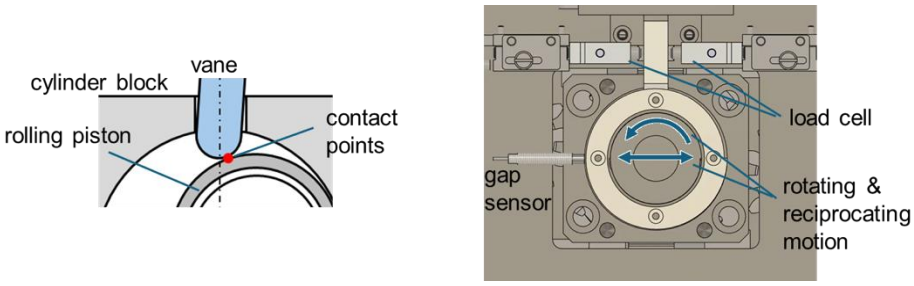

(a) Vane and rolling piston (b) Experimental model

Figure 7.2-2 Experimental setup for friction coefficient between vane and rolling piston of rotary compressor

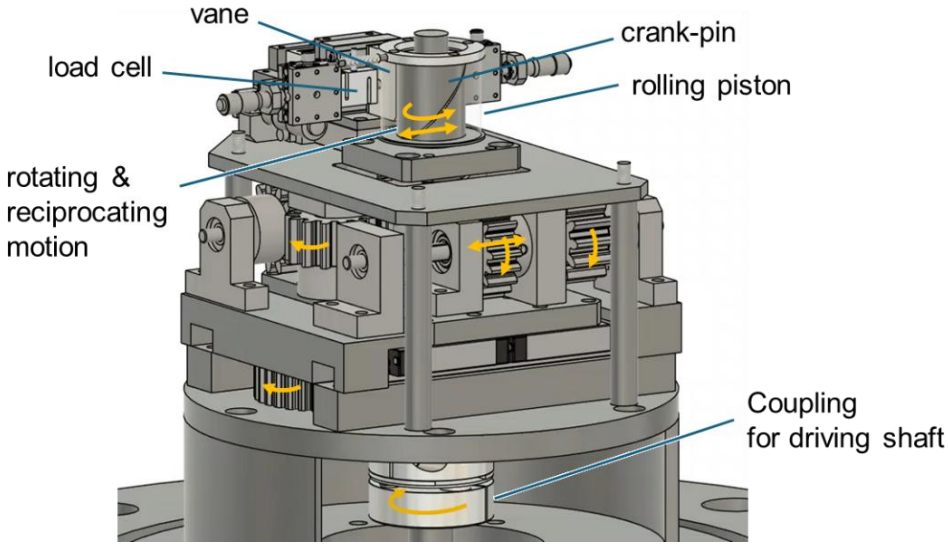

Figure 7.2-6 Experimental setup for friction measurements at vane and rolling piston of rotary compressor

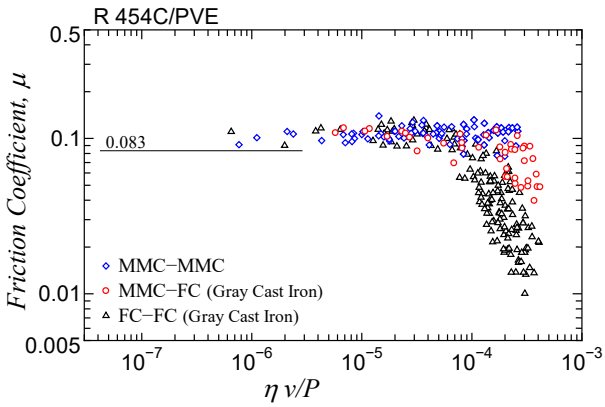

Figure 7.2-7 Coefficient of friction as a function of the dimensionless bearing characteristic number

The actual sliding velocity v was obtained by subtracting the reciprocating velocity from the angular velocity of the rolling piston. The coefficient of friction was then organized using this actual sliding velocity. Figure 7.2-7 shows the coefficient of friction calculated by dividing the measured friction force by the pressing force applied to the back surface of the vane. The horizontal axis represents the dimensionless bearing characteristic number expressed as $\eta v/P$. The triangular symbols indicate the results for the cast iron/cast iron combination, the diamond symbols indicate those for the composite/composite combination, and the circular symbols indicate those for the composite/cast iron combination.

For the cast iron/cast iron combination, the coefficient of friction tended to decrease gradually when the horizontal-axis value was approximately 5×10^{-5} or higher. For the composite/cast iron combination, the coefficient of friction tended to decrease gradually when the horizontal-axis value was approximately 1×10^{-4} or higher; however, for the composite/composite combination, no decrease in the coefficient of friction was confirmed within the range of the present test. This indicates that, under the same load conditions, the velocity at which the mixed-lubrication state is reached is higher for the composite/composite combination than for the cast iron/cast iron combination. Accordingly, in the design of high-speed compressors, using a composite/composite combination is considered to be somewhat disadvantageous in terms of friction. However, by using a composite material for the rolling piston and cast iron for

the vane, it is considered possible to achieve both weight reduction of the main body and a low coefficient of friction. In the range where the horizontal-axis value was smaller than approximately 5×10^{-5}, the coefficient of friction was almost constant. No difference attributable to material type was observed. As the data scatter was somewhat large, further investigation is planned.

7.2.4 Wear characteristics of cast iron and composite materials

The wear characteristics when using composite materials are currently being investigated. A ball-on-plate test was conducted in which a steel ball was pressed against flat cast iron and composite-material plates while the plates were reciprocated, and the wear scars after the sliding tests were observed using a confocal microscope. Although this test differs from the actual sliding conditions in a compressor, it was performed as a reference for examining wear characteristics. Tests were conducted under two conditions: a dry sliding surface and a sliding surface coated with refrigeration oil (VG68). The volume loss owing to wear was measured using a confocal microscope and organized in terms of the specific wear amount. The effects of surface roughness and contact surface pressure are currently being analyzed, and detailed results will be reported in due course.

7.3 Examination of Compressor Mechanical Efficiency Based on Experimental Results for the Coefficient of Friction

Ishii *et al*. (1988, 1989) conducted experiments on a 600 W-class rolling-piston rotary compressor operating steadily at 3405 rpm under the JIS standard conditions: evaporation temperature of 7 °C, condensation temperature of 55 °C, degree of superheat of 11 °C, suction pressure of 0.54 MPa, discharge pressure of 2.06 MPa, and refrigerant R22. They clarified the following points: (1) the mechanical efficiency was 90.3%; (2) the average rotational speed of the rolling piston was 32 rpm; (3) hydrodynamic lubrication was formed between the rolling piston and crank pin; and (4) boundary lubrication was formed between the crankshaft and bearings. Furthermore, they estimated that the viscosity coefficient of the lubricating oil (SUNISO 4GS) was 2.076 mPa·s under standard conditions, namely an ambient pressure of 2.06 MPa, saturated solubility of R22 of 15%, average temperature of 100 °C, kinematic viscosity of 2.4 cSt, and specific mass of $0.865 \times 10^{-3}\ \mathrm{kg/m^3}$. They then performed detailed mechanical-dynamics simulations and, based on the experimentally clarified results, found that the Coulomb friction coefficient between the vane and rolling piston and between the vane and cylinder groove was 0.083.

In the results obtained from the present friction and wear tests, shown in Figures 7.2-4 and 7.2-7, the coefficient of friction at relatively small bearing characteristic numbers was close to the value of 0.083 identified in the previous study. However, the values measured in the present research diverged considerably from the coefficient of friction identified in that study. This difference is considered to be attributable to factors such as the refrigerant, lubricating oil, and materials. In particular, a characteristic rapid decrease in the coefficient of friction was observed in the region where the bearing characteristic number was high. As the bearing characteristic number increases during high-speed compressor operation, this result is considered extremely important for simulating compressor performance under such conditions.

Using the coefficient-of-friction values from the friction and wear tests, losses at each kinematic pair and the resulting mechanical efficiency can be determined via mechanical-dynamics simulations of the compressor's moving components. For a rotary compressor, the equations of motion of the crankshaft system need only be solved simultaneously with the equation of motion for the rolling piston's rotation. The analyses of Yanagisawa (1983), Imaichi *et al*. (1983), and Ishii *et al*. (1989) can be applied for this purpose.

Calculations are also being conducted to examine how losses at each sliding part change when composite materials are used for the moving components, and what dimensional specifications maximize mechanical efficiency under composite materials and high-speed operation. As the use of composite materials, which are lighter than cast iron, changes the reciprocating inertial force of the vane, it is important to clarify the effect of this change on efficiency.

Furthermore, compressor-body vibration during high-speed operation is also being analyzed, and balance design to minimize it is under investigation. The results of these analyses will be reported in due course.

References (Section 7)

Ishii, N., Yamamura, M., *et al.*, 1988, The High Mechanical Efficiency of Rolling-Piston Rotary Compressors (1st Report, Experimental Study), *Trans. of the JSME. C.*, vol. 54, no. 507: p. 2578-2582. (in Japanese)

Ishii, N., Fukushima, M., *et al.*, 1989, The High Mechanical Efficiency of Rolling-Piston Rotary Compressors (2nd Report, Theoretical Study), *Trans. of the JSME. C.*, vol. 55, no. 511: p. 687-695. (in Japanese)

Imaichi, K., Fukushima, M., *et al.*, 1983, Vibration Analysis of Rotary Compressors, *Trans. of the JSME. C.*, vol. 49, no. 447: p. 1959-1970. (in Japanese)

Okada, K., Hisayama, K., 1975, Piston Behavior of a Rotary Compressor, *Refrigeration*, vol. 50, no. 571: p. 331-338. (in Japanese)

Shimizu, T., 1976, Friction Loss of Rotating Piston in Rotary Compressor for Air Conditioning, *Refrigeration*, vol. 51, no. 589: p. 959-965. (in Japanese)

Slayton, C.R., Hall, E.M., 1982, Compressor Roller Bearing Dynamics Analysis, *Proc. Purdue Compressor Tech. Conf.*: p. 417-425.

Yanagisawa, T., 1982a, Piston Behavior and Mechanical Losses of the Rolling Piston Type Rotary Compressor (1st Report, Experimental and Theoretical Analyses of Piston Behavior), *Trans. of the JSME. C.*, vol. 48, no. 429: p. 732-740. (in Japanese)

Yanagisawa, T., 1982b, Piston Behavior and Mechanical Losses of the Rolling Piston Type Rotary Compressor (2nd Report, Analysis of Mechanical Friction Loss), *Trans. of the JSME. C.*, vol. 48, no. 435: p. 1854-1861. (in Japanese)

Yanagisawa, T., 1983, A Study on the Fundamental Operating Characteristics of Rolling Piston Type Rotary Compressors, *Doctoral dissertation*, Osaka University. (in Japanese)

8. Development of Metal-Matrix Composite Materials Suitable for Compressor Components and Evaluation of Their Fundamental Properties (Advance Composite Co., Ltd.)

This research and development has been conducted to design the material properties of compressor components compatible with low-GWP mixed refrigerants, develop lightweight and high-rigidity new materials with clarified characteristics, and elucidate the fundamental properties of metal-matrix composite materials suitable for such components, thereby contributing to the miniaturization and weight reduction of compressors. These metal-matrix composite materials were supplied to Shizuoka University and Osaka Electro-Communication University. Furthermore, in collaboration with Shizuoka University, compatibility with refrigeration oil and evaluation as compressor materials were conducted. In collaboration with Osaka Electro-Communication University, lubrication characteristics were evaluated, and compressor design guidelines for the use of lightweight and high-rigidity materials were examined. The fundamental property items of the metal-matrix composite materials to be developed include density, tensile strength, hardness, fatigue strength, and Young's modulus.

8.1 Design of Metal-Matrix Composite Materials

8.1.1 Material survey for compressor components (FY2023)

Compressors consist of a wide variety of components; this study focused on rotating components and developed lightweight materials for them. In general, cast iron (FC200 or FC250) is often used; therefore, the company developed a lightweight and high-rigidity aluminum-based composite material as an alternative to cast iron. The existing material and the target mechanical-property values for the material to be developed are shown below (Table 8.1-1).

Table 8.1-1 Mechanical properties of existing and developmental materials

Item	Unit	FC250	Development product
Density	g/㎤	7.2	≦3.0
Tensile strength	MPa	250	≧200
Young's modulus	GPa	100	≧110
Coefficient of Thermal Expansion	ppm/K	12.0	≦14.0
Fatigue strength	MPa	112	≧100
Brinell hardness	HBW	≦241	≧120

8.1.2 Design of metal-matrix composite materials

The rule of mixtures was used to design the metal-matrix composite materials.

When a metal with a density of ρm is combined at a volume fraction of 50% with ceramic particles with a density of ρf at a volume fraction of 50%, the density ρc of the resulting composite material can be regarded as the average of ρm and ρf and is expressed by the following equation.

$$\rho c = \frac{\rho f + \rho m}{2} \tag{8.1-1}$$

Thus, the density can be obtained from the above equation. If the volume fraction of ceramic particles is denoted by Vf, the volume fraction of the metal is (1−Vf), and the equation can be rewritten as follows.

$$\rho c = Vf\rho f + (1 - Vf)\rho m \quad (8.1\text{-}2)$$

This relationship can be further generalized and expressed as follows.

$$Uc = VfUf + (1 - Vf)Um \quad (8.1\text{-}3)$$

Here, *U*c denotes the property of the composite material, *U*f denotes the property of the reinforcement, *V*f denotes the volume fraction of the reinforcement, and Um denotes the property of the metal. In this case, various properties such as the coefficient of thermal expansion and elastic modulus can be substituted for the property represented by *U*. This is referred to as the rule of mixtures. This relationship assumes no reaction between the reinforcement and the matrix, and no volume change. In practice, the rule of mixtures is often applicable to density; however, for properties that are strongly affected by the distribution and shape of the reinforcement, such as the coefficient of thermal expansion and thermal conductivity, the accuracy of prediction using the rule of mixtures is not very high. Tensile strength and elastic modulus are affected by the strength of the interface between the reinforcement and the metal, as well as by the distribution state. Accordingly, the rule of mixtures is often used as a guideline for design during examination, and it was also utilized in the development of the metal-matrix composite materials.

8.2 Development of Metal-Matrix Composite Materials

8.2.1 Verification of the effects of changing the matrix in metal-matrix composite materials (FY2023)

Based on the material survey, development was conducted using mechanical properties equivalent to those of cast iron FC250 as the benchmark. First, the matrix alloy used in AC-Albolon®, the company's standard product, was changed to improve strength. The mechanical properties of the composite material subsequently designed and obtained are shown below.

Table 8.2-1 Mechanical properties of existing and developmental materials

Item	Unit	FC250	AC-Albolon®	Development product
Density	g cm^{-3}	7.2	2.8	2.79
Tensile strength	MPa	250	250	240–260
Young's modulus	GPa	100	120	110–115
Coefficient of Thermal Expansion	ppm K^{-1}	12.0	12	11–12
Fatigue strength	MPa	112	105	105
Brinell hardness	HBW	≦241	Not stated	129

The obtained results showed that the expected mechanical strength was generally achieved; however, the fatigue strength was slightly low at 105 MPa. Accordingly, the fracture surfaces of the fatigue-strength specimens were observed. Photographs of the fracture surfaces are shown below.

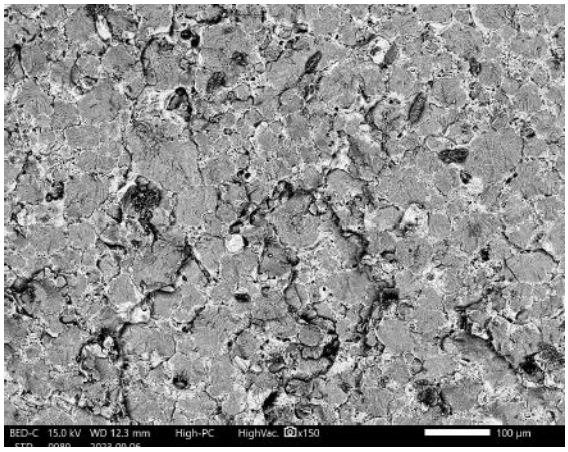

AC-Albolon®

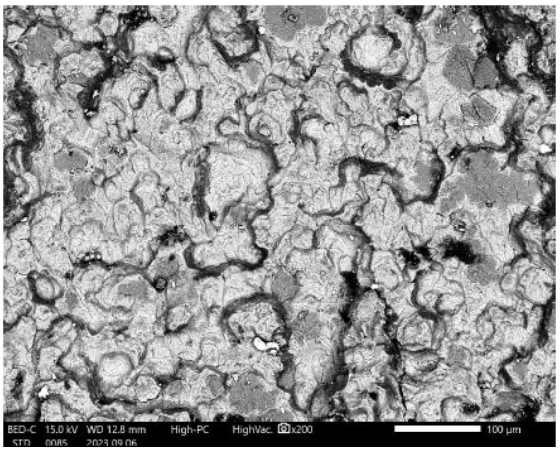

Development product

Figure 8.2-1 Micrographs of existing materials and development samples

The fracture surfaces after fatigue-strength testing were compared between AC-Albolon® and the developed product in which the matrix was changed. In AC-Albolon®, reinforcement particles were observed over the entire fracture surface, and crack propagation appeared to occur along grain boundaries in both materials. By contrast, although a small number of reinforcement particles were observed in the composite material of the developed product, its fracture morphology differed substantially. In addition, linear groove-like patterns were observed in the matrix around the reinforcement on the fracture surface of the developed product, suggesting that cracks propagated along these lines. However, as large variations were observed in the shape and particle size of the reinforcement materials used in both composite materials, these are considered to have contributed to both scatter in, and an overall reduction of, material strength.

8.2.2 Design and development of reinforcement structure in metal-matrix composite materials (FY2024)

To meet the mechanical-property targets from the FY2023 composite, its reinforcement particles were reviewed, and the material was redesigned, fabricated, and re-evaluated. Their shape and particle size were adjusted to improve mechanical strength. The evaluation results are shown below.

Table 8.2-2 Mechanical properties of existing and developmental materials

Item	Unit	‘23_MMC02N	‘24_MMC02N
Density	g cm^{-3}	2.79	2.73
Tensile strength	MPa	240～260	360
Young's modulus	GPa	110～115	120
Coefficient of Thermal Expansion	ppm K^{-1}	11-12	12.5
Fatigue strength	MPa	105	133
Brinell hardness	HBW	129	174

* The values of the developed material shown in the table are average values for N5.

By redesigning the reinforcement's particle shape and size, the mechanical strength was successfully improved. Next, comparisons of fracture-surface observations for tensile test specimens and fatigue-strength specimens are shown.

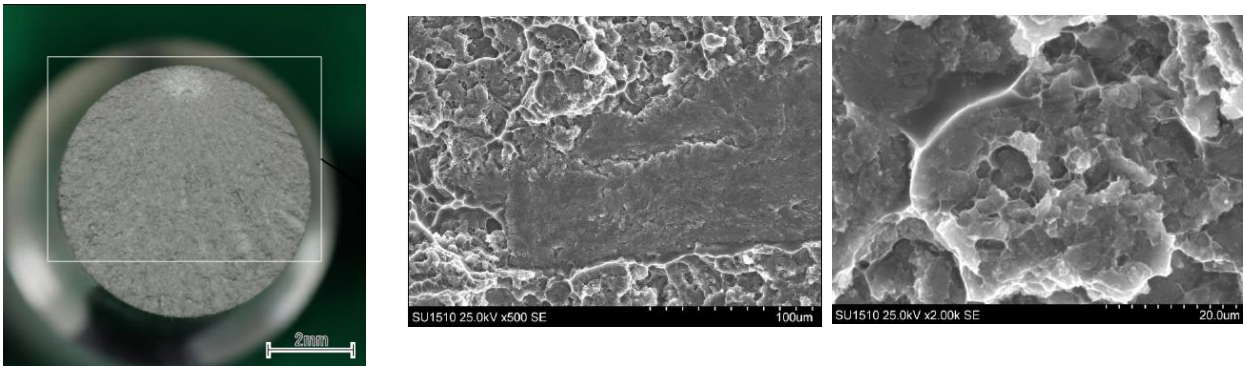

Fracture Surface Appearance　　Surface origin　　Crack propagation region

Figure 8.2-2 Tensile fracture surface

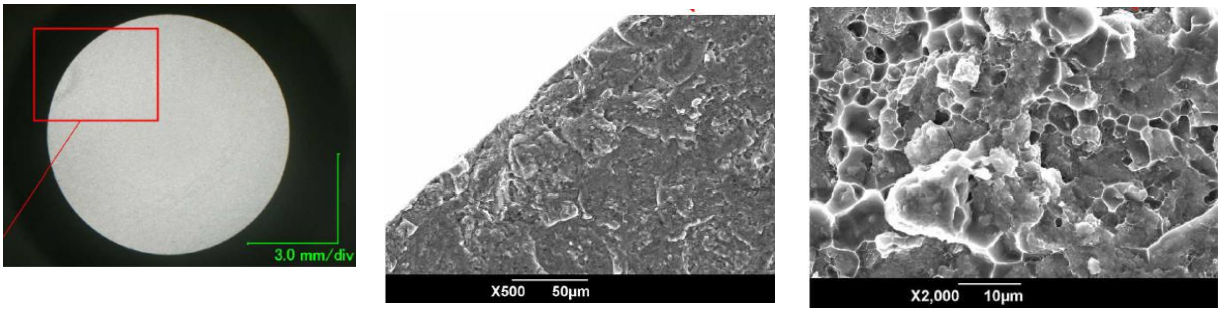

Fracture Surface Appearance　　Surface origin　　Crack propagation region

Figure 8.2-3 Fatigue fracture surface

Fracture-surface observations in the tensile tests (Figure 8.2-2) showed clear radial patterns on all specimens, and the fracture origins could be readily identified. Although the fracture appearance suggested brittle fracture without deformation, microscopic SEM observations revealed many dimples, which are traces of ductile fracture. Observations of the origin regions suggested brittle fracture in all specimens, though region size varied. Flat regions were also observed, varying in size among specimens; larger flat regions tended to correspond with a greater impact on fracture strength.

In the fracture-surface observations after fatigue-strength testing (Figure 8.2-3), the fracture morphology was smooth, and pores resembling dimples were scattered across the surface. As these features closely resembled the particle shape of the reinforcement, its shape is considered to have persisted in the composite material. The fatigue fracture surface's microscopic morphology was characteristic of metal-matrix composite materials, making the crack-propagation direction difficult to determine from it alone. By contrast, macroscopic observations allowed relatively easy estimation of the fracture origin, final fracture location, and crack-propagation path. Meanwhile, many inclusions were observed on the fracture surfaces. These inclusions are presumed to have entered during the reinforcement-processing step when binder was added.

Based on these results, mechanical-property values equivalent to or higher than those of FC250 were obtained. Moreover, by reviewing the powder morphology of the reinforcement rather than changing the matrix, mechanical-property values exceeding those of conventional AC-Albolon® were successfully achieved.

8.2.3 Machinability evaluation of metal-matrix composite materials (FY2025)

The machinability of the FY2024 metal-matrix composite material was evaluated, and its processing characteristics were clarified.

In addition, rolling pistons and vanes were provided to Osaka Electro-Communication University (Machine C-2) for the evaluation of friction and wear. The results of the machinability evaluation are presented below.

Table 8.2-3 Test conditions

Item	Machinability evaluation conditions for milling
Test machine	NV5000α (DMG Mori Seik)
Lubrication	Dry (Air blow)
Work material	Albolon® / MMC02N (Developed material)
Work material size [mm]	85 × 85 × 45
Tool	φ10 AE-TS-N10 × 3 / tooth (OSG)
Tool overhang [mm]	30
Spindle speed [rpm]	6,000
Table feed rate [mm min^{-1}]	7,000
Depth of cut [Rough]	ap = 1.0 mm / ae = 5.0 mm
Depth of cut [finish]	ap = 5.0 mm / ae = 0.05 mm
Measurement timing [pass]	24 (2 m) / 59 (5 m) / 118 (10 m)
Tool wear measurement device	Zoller pomBasicMicro
Cutting force measurement device	Kistler 9255B (Fx,Fy,Fz,Fc)
Cutting temperature measurement device (Thermocouple)	MULTI INTELLIGENCE® ASM (Yamamotokinzokuseisakusyo)

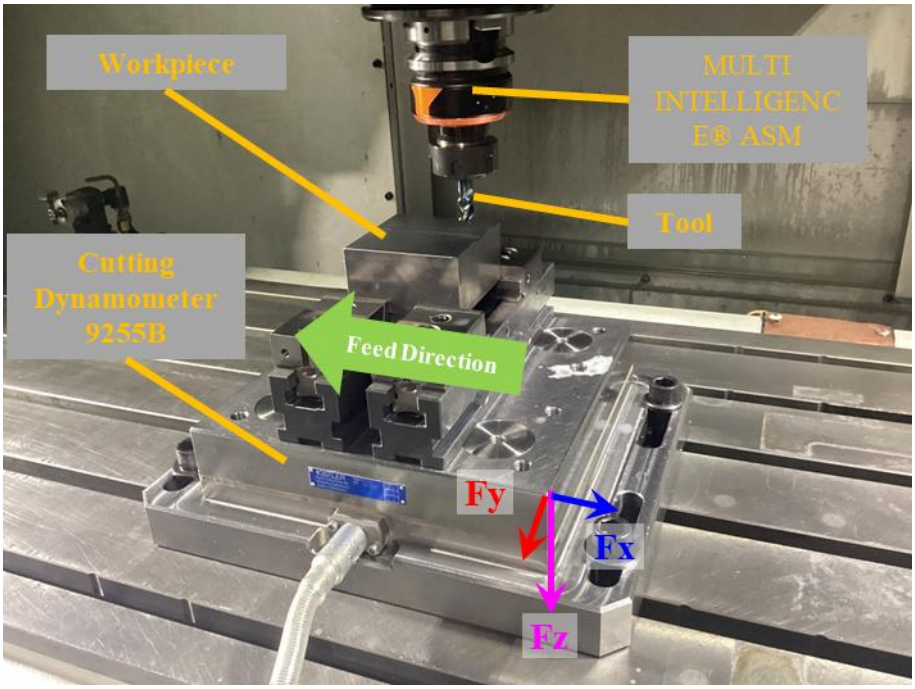

Figure 8.2-4 Machinability evaluation setup

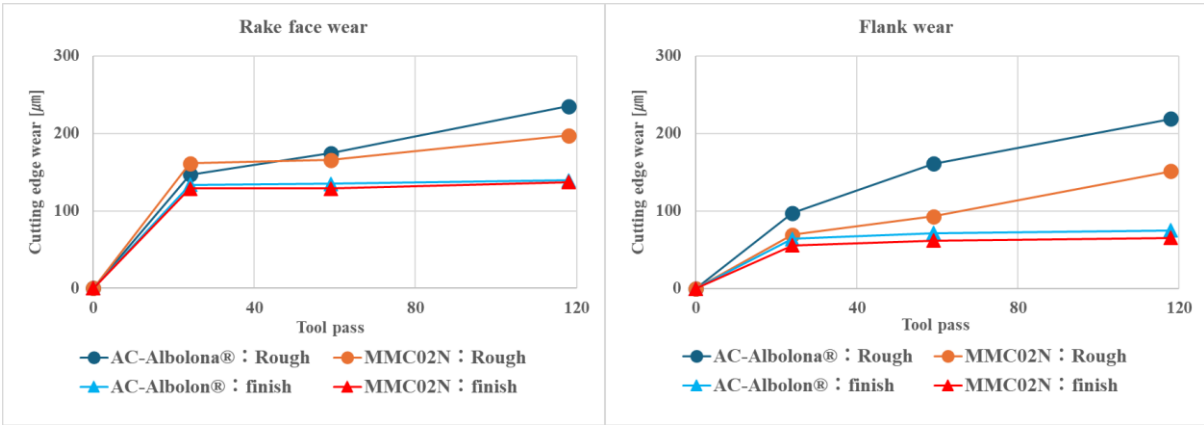

Figure 8.2-5 Tool wear

In the tool-wear evaluation test (Figure 8.2-5), under rough-machining conditions, both materials exhibited flank wear of slightly less than 0.1 mm at a machining distance of 2 m (24th pass), and the amount of wear subsequently increased with machining distance. However, wear progressed more rapidly for AC-Albolon®. Under finishing conditions, the change in wear width for each pass was smaller for both materials than under rough-machining conditions. Although MMC02N has higher mechanical strength, its wear progression rate was lower than that of AC-Albolon®.

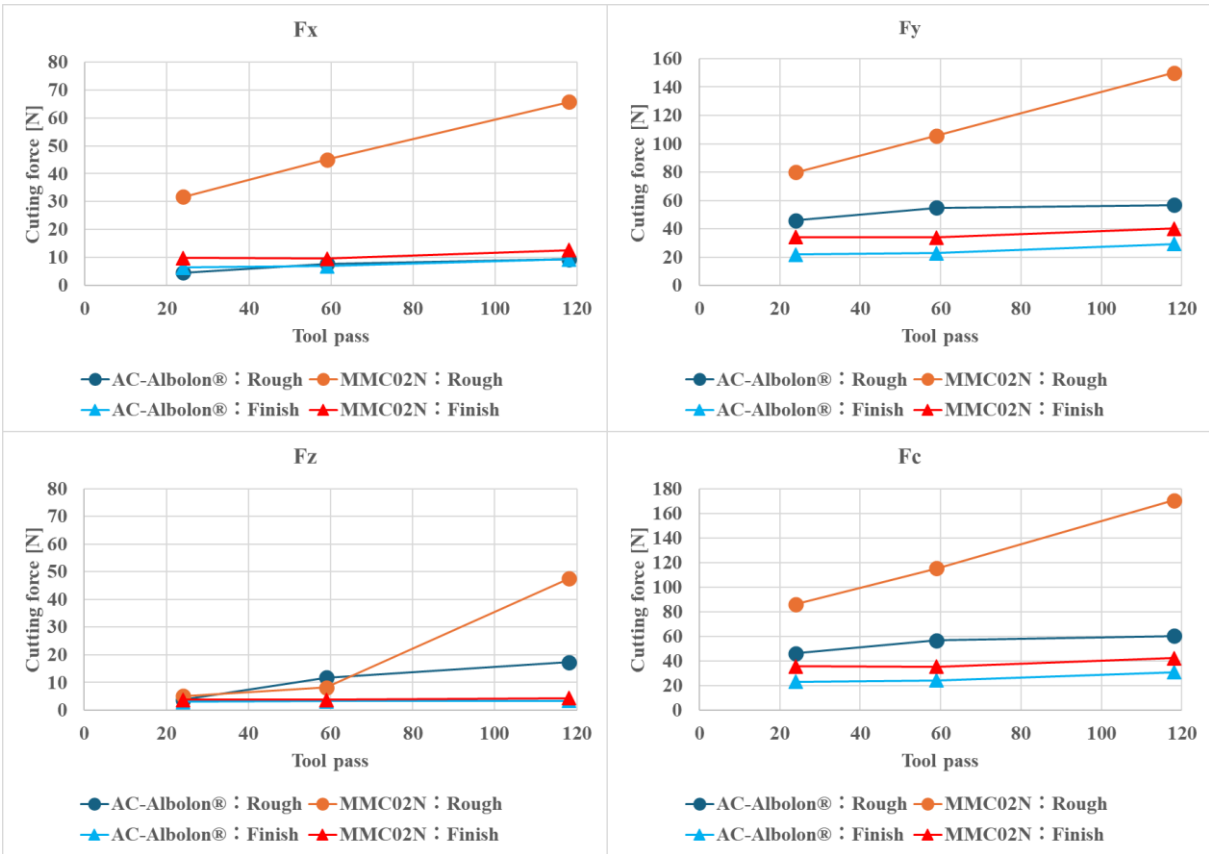

Figure 8.2-6 Cutting force

In the cutting-force evaluation (Figure 8.2-6), although MMC02N exhibited slower wear progression, its cutting force was 35% higher than that of AC-Albolon®, presumably reflecting its higher material strength. Focusing on the Fc value of MMC02N, the cutting force increased nearly twofold after machining from 2 m to 100 m. By contrast, although

severe tool wear occurred for AC-Albolon®, the increase in cutting force was only slight compared with MMC02N. Under finishing conditions, the variation in cutting force was moderate, and the Fc value of MMC02N was generally approximately 10 N higher than that of AC-Albolon®.

In the cutting-edge temperature evaluation (Figure 8.2-7), temperature increased with each pass under all conditions. Under finishing conditions, the temperature increase per pass was small, as the radial depth of cut was also small. Comparing the two materials, MMC02N tended to exhibit a higher cutting temperature.

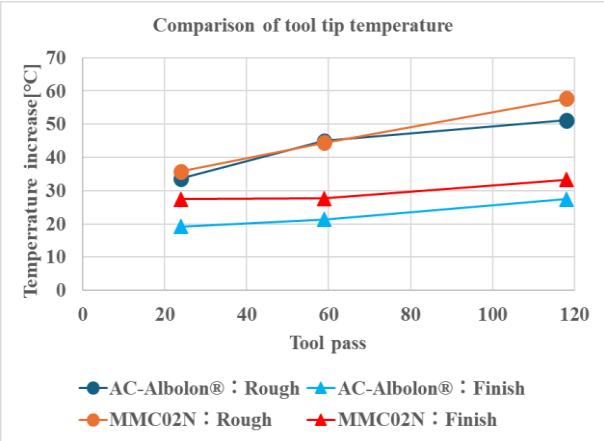

Figure 8.2-7 Cutting temperature measurement

In summary, MMC02N showed higher values than AC-Albolon® in terms of cutting force and cutting-edge temperature increase. In the wear evaluation, however, progression was comparable up to the 24th pass; thereafter, it slowed for MMC02N, which showed less wear by the 118th pass. Photographs of the cutting edges of the tools used in this test are shown in Figure 8.2-8.

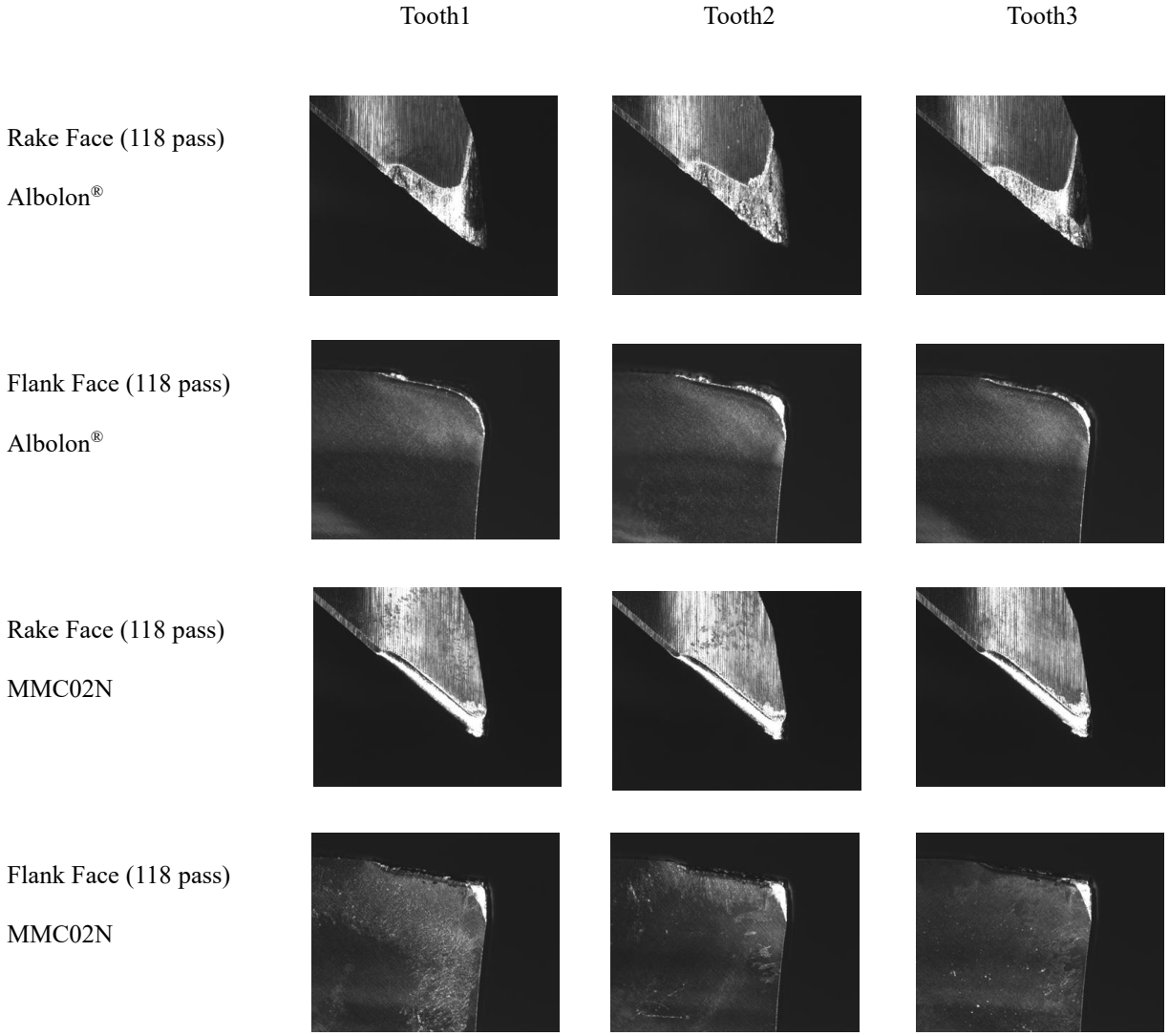

Figure 8.2-8 Photographs of tool wear

Next, in lathe machining, wear, cutting force, and post-machining surface roughness were compared between carbide tools and diamond tools. The evaluation conditions are shown below (Table 8.2-4).

Table 8.2-4 Test conditions

Test machine	NL2500Y/750 (DMG MoriSeik)
Lubrication	emulsion-type water-soluble cutting fluid
Work material	MMC02N (Developed material)
Work material size [mm]	85×85×45
Tool （Roughing）	CNMG120408 AH-KW10 (Kyocera)
Tool （Finish）	CNMM120408M SE-KPD001 (Kyocera)
Workpiece chucking force [MPa]	1.6
Roughing Cutting speed (V) [m min^{-1}]	80
Finishing Cutting speed (V) [m min^{-1}]	100
Roughing Depth of cut (f) [mm rev^{-1}]	0.2 / ap = 1 mm
Finishing Depth of cut (f) [mm rev^{-1}]	0.1 / ap = 0.5 mm
Tool wear measurement device	HRX-01(HiROX)

Cutting force measurement device	9129AA (KISTLER)
Surface roughness measurement	SURFTEST SJ-210 (Mitutoyo)

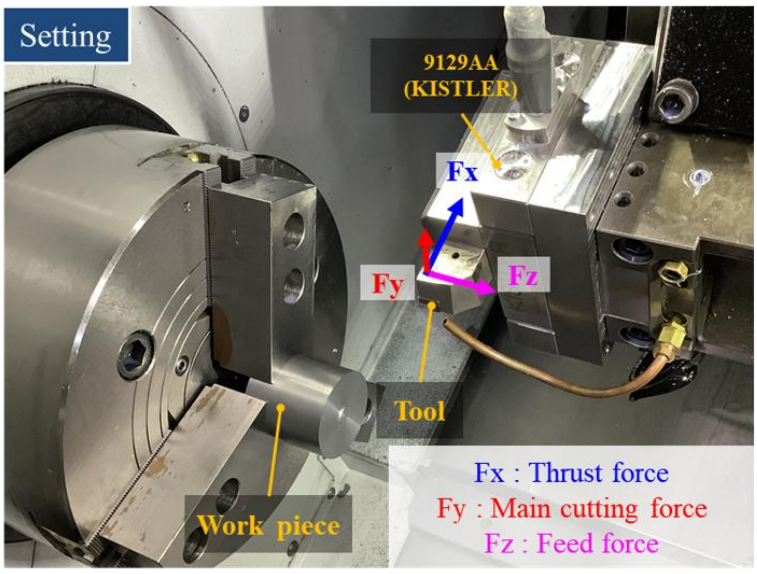

Figure 8.2-9 Machinability evaluation setup

Results under the conditions in Table 8.2-4 are presented as tool wear on the outer diameter (Figure 8.2-10) and end face (Figure 8.2-11).

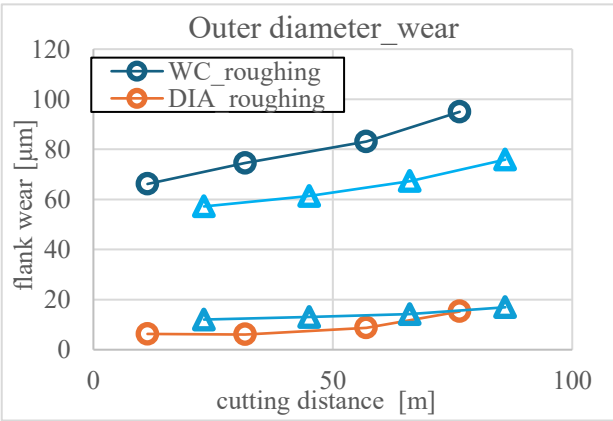

Figure 8.2-10 Outer diameter tool wear

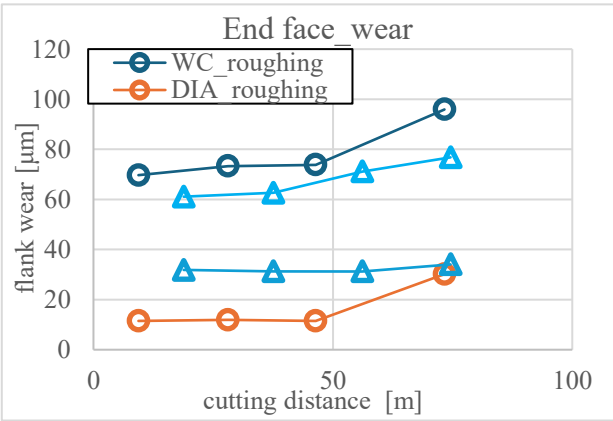

Figure 8.2-11 End face wear

Tool wear tended to increase from a cutting distance of approximately 40 m for both the carbide and diamond tools. By contrast, wear of the diamond tool under finishing conditions remained almost constant. Next, the stress applied to the tool during cutting is reported below as the resultant cutting force (Figures 8.2-12 and 8.2-13).

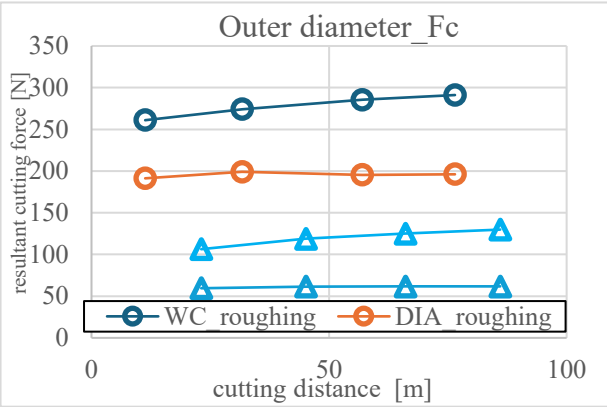

Figure 8.2-12 Resultant cutting force (OD)

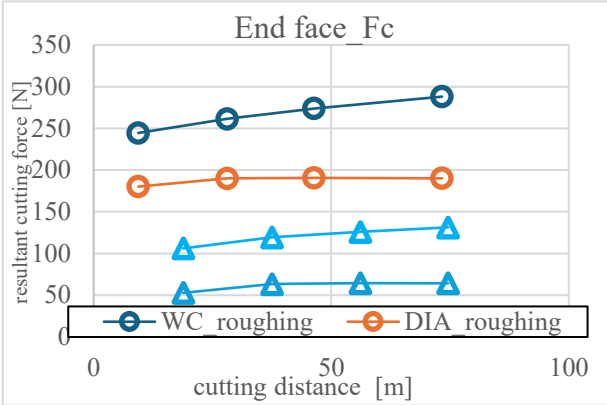

Figure 8.2-13 Resultant cutting force (End face)

The carbide tool tended to show a higher cutting force under both roughing and finishing conditions. Next, the surface roughness compared by tool type is reported (Figures 8.2-14 and 8.2-15).

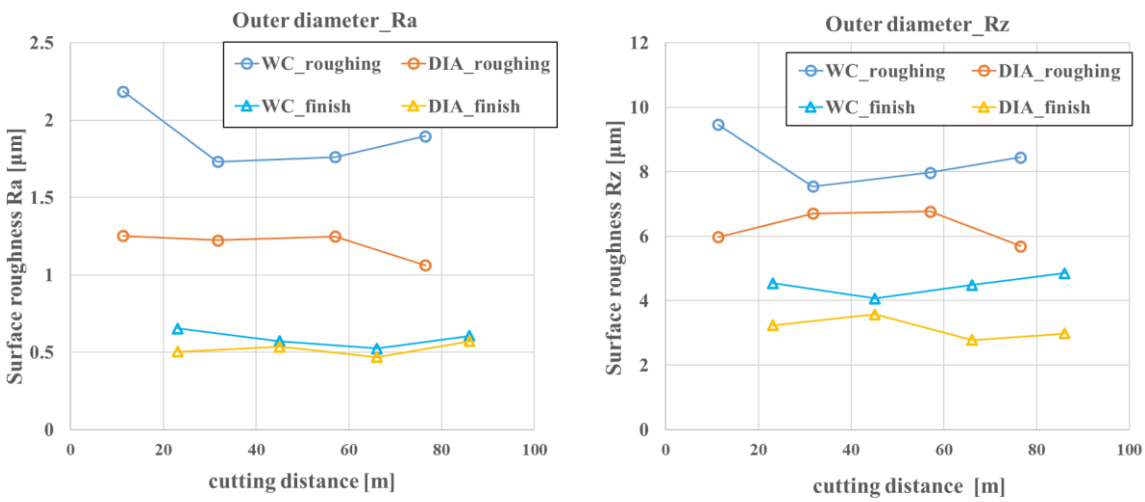

Figure 8.2-14 Surface roughness (Outer diameter)

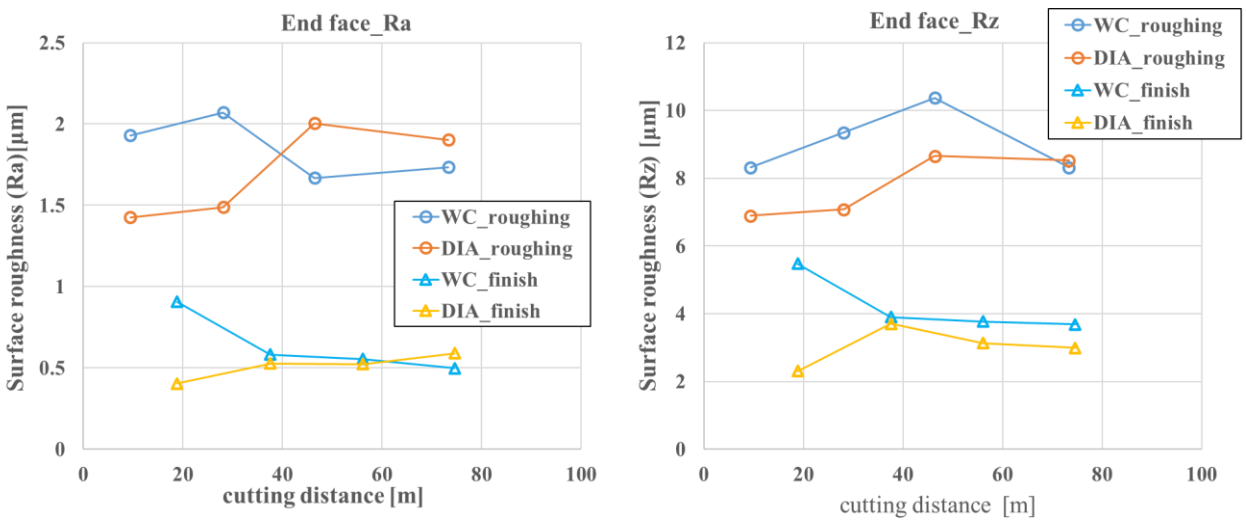

Figure 8.2-15 Surface roughness (End face)

In carbide finishing, both Ra and Rz showed high values at the first pass. In diamond roughing, both values increased substantially at the third pass. Examining the cutting edge where these large changes occurred suggested that, in carbide finishing, initial wear had a pronounced influence. At the third pass in diamond roughing, aluminum appeared to adhere to the cutting edge; however, adhesion was no longer observed as the cutting distance increased (Figure 8.2-16).

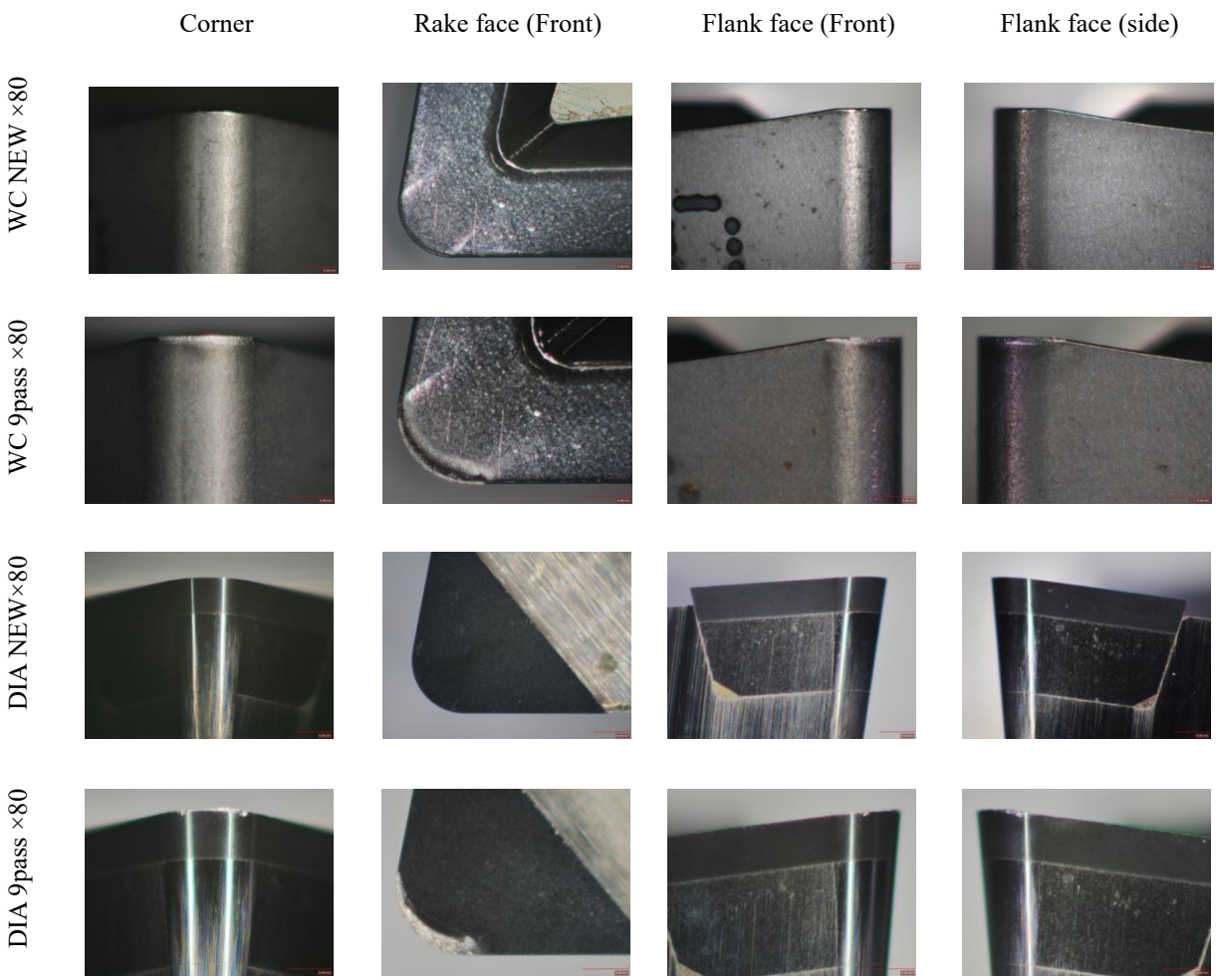

Figure 8.2-16 Photographs of tool wear

To measure the sliding characteristics of the metal-matrix composite material at Osaka Electro-Communication University (Machine C-2), the following rolling piston and vane were provided as test pieces (Figure 8.2-17).

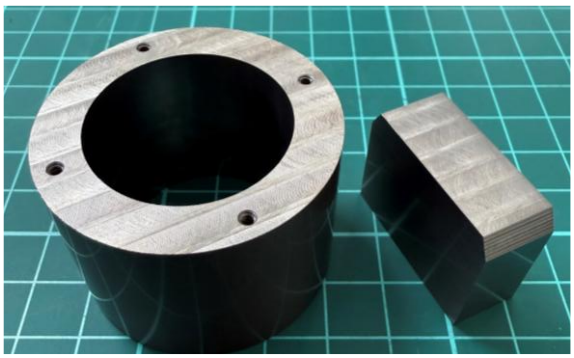

Figure 8.2-17 Rolling piston and vane

8.2.4 Summary

The target mechanical-property values were successfully achieved. A comparison of the mechanical properties of the existing material and the metal-matrix composite material developed in this study is shown below (Table 8.2-5). In terms of density, the developed material achieved an approximately 60% weight reduction compared with the existing material, indicating that it can contribute to the target of a 10% reduction in compressor weight in this study. At the same time, tensile strength, Young's modulus, and fatigue strength were also improved.

In the machinability evaluation, the developed metal-matrix composite material ('24_MMC02N) exhibited higher cutting resistance; however, tool wear progression was approximately 30% lower than for the conventional material.

Table 8.2-5 Mechanical properties of existing and developmental materials

Item	Unit	FC250	'24_MMC02N	Change (%)
Density	g cm^{-3}	7.2	2.73	−62.1%
Tensile strength	MPa	250	360	44.0%
Young's modulus	GPa	100	120	20.0%
Coefficient of Thermal Expansion	ppm K^{-1}	12.0	12.5	4.2%
Fatigue strength	MPa	112	133	18.8%
Brinell hardness	HBW	≦241	174	−27.8%

8.2.5 Future plans

From 2023 to 2025, the developed materials are considered to have met their targeted objectives for mechanical properties and machinability. In future work, development will be advanced with a focus on productivity, cost, and related factors (Figure 8.2-18).

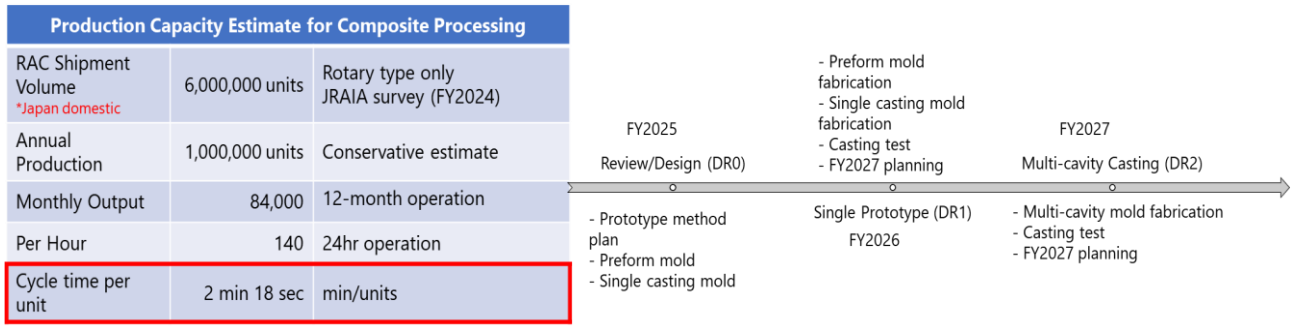

Figure 8.2-18 Cost survey and activities in the latter half of the project period

References (Section 8)

Nishida, Y., Introduction to Metal Matrix Composites, Corona Publishing Co., Ltd., Section 1.2, "Rule of Mixtures," pp. 9–10 (in Japanese).

Advance Composite Co., Ltd., "AC-Albolon®," product brochure, company website.